

---

# Effect of excitons in quantum spin Hall effect

---

*Author:*  
Tania Paul

*Supervisors:*  
Dr. Timo Hyart  
Dr. hab. Wojciech Brzezicki

*Submitted in partial fulfillment of the requirements for the degree of*

**DOCTOR OF PHILOSOPHY**

August 21, 2023



INTERNATIONAL RESEARCH CENTER MAGTOP,  
INSTITUTE OF PHYSICS, POLISH ACADEMY OF SCIENCES, WARSAW,  
POLAND

*To my parents*

*"We spent our day looking under rocks in the creek..."*

- Bill Watterson, *Calvin and Hobbes*, 30 June 1992

---

## Acknowledgement

I would like to begin by conveying my gratitude to Timo, without whom the completion of the two research projects that comprise this thesis would not have been possible. Apart from being an excellent physicist, he has also been a wonderful PhD guide right from the beginning. He created a positive and collaborative work environment, where I was given the time to learn from my failures and improve my research capabilities. His dedication and approach to research is inspiring and made working with him rewarding.

I would like to give my sincere thanks to Victor, who has consistently made time to help me when I was stuck with computational or analytical problems. I have also learnt a lot from his exceptional coding skills and his approach to work. During his time at the institute, he always gave me space to discuss and cleared my conceptual doubts with respect to our research.

I would like to thank Dr. hab. Wojciech Brzezicki for his support and help with the thesis. I am thankful to Prof. Tomasz Dietl and Prof. Tomasz Wojtowicz for their numerous help during this period. I would also like to extend my thanks to Dr. hab. Carmine Autieri, for letting me use his computational grant in my first year and providing me with important information regarding the doctoral procedures at the institute.

Even though we were not research collaborators, Archana has listened to my silly physics questions every time. The discussions and laughter we shared in the office translated to a genuine friendship which I will always cherish. I would like to thank Nguyen, who was my first friend in the institute and with whom I have also shared many laughs and discussions. Ashutosh, who has inspired me with his contagious enthusiasm for physics and design ideas. To Arathi, Saranya, Sarath, Giuseppe and Peixin for joys of friendship. To Anna, Agnieszka, Sylwia and Bozena for their assistance during this period.

To Lekha ma'am for believing in me and pushing me to do better. To Tabish sir for introducing me to theoretical research. Lastly, I am grateful and indebted to my parents for always encouraging my dreams and life decisions, my husband Umair for

---

his love and support, and my folks from back home.

---

## Abstract

A quantum spin Hall insulator is a two-dimensional insulator with an insulating bulk and conducting edges. They belong to an entirely new class of materials which cannot be adiabatically connected to usual (topologically trivial) insulators and semiconductors. Much like the quantum Hall and quantum anomalous Hall effects, the quantum spin Hall effect also finds connection to topology to explain its many interesting features. After establishing key concepts related to topological materials in general and quantum spin Hall effect in particular, this thesis begins an investigation into electron-hole correlations in the quantum spin Hall effect of band-inverted electron-hole bilayers. The Coulomb interactions favors the formation of excitons, a pair of electron and hole from the conduction and valence bands, respectively, that condense to form a highly coherent phase. Excitonic correlations enrich the topological phase diagram of quantum spin Hall insulators by inducing an insulating phase with spontaneously broken time-reversal symmetry between the trivial and quantum spin Hall phases. One of the paradigmatic features of topological phase transitions in correlation-free topological insulators is the bulk-gap closing. However, the presence of excitons lead to a transition where the bulk-gap does not close. This could be interpreted as an effort by the system to minimise energy during the topological transition. There are multiple, recent experimental observations pointing out the existence of excitons in these systems but so far the spontaneous time-reversal symmetry breaking has not been directly observed. In the original work carried out for this thesis, we propose an experimental set-up to observe this time-reversal symmetry broken phase. Numerical experiments of transport in a Corbino disc measure bulk and edge conductances and confirm that the topological phase transition manifests without bulk-gap closing. Moreover, we also propose to utilize the system in its broken time-reversal symmetry state, together with an s-wave superconductor, to create, probe and manipulate the appearance of Majorana zero modes. We find, both numerically and analytically, the existence of Majorana zero modes at the interface of an s-wave superconductor and a time-reversal symmetry broken insulator. We provide an experimental configuration of a superconductor/TRS broken insula-

---

tor/superconductor Josephson junction to observe  $4\pi$  Josephson current, which is indicative of the Majorana zero modes residing at the interface. Finally, we also propose how to manipulate the quantum information stored in the Majorana zero modes and read out the state of the topological qubit.

---

## Streszczenie

Kwantowe spinowe izolatory Halla to układy dwuwymiarowe z izolującą objętością i przewodzącymi krawędziami. Należą one do zupełnie nowej klasy materiałów, których nie da się połączyć adiabaticznie ze zwykłymi (topologicznie trywialnymi) izolatorami i półprzewodnikami. Podobnie jak kwantowy i kwantowy anomalny efekt Halla, kwantowy spinowy efekt Halla również wiąże się z topologią, co pozwala wyjaśnić jego wiele interesujących cech. Po ustaleniu kluczowych pojęć związanych ogólnie z materiałami topologicznymi, a w szczególności z kwantowym spinowym efektem Halla, niniejsza praca skupia się na badaniu korelacji elektron-dziura w układach dwuwarstwowych z odwróconymi pasmami. Oddziaływania kulombowskie sprzyjają tworzeniu ekscytonów, par elektronów i dziur odpowiednio z pasm przewodnictwa i walencyjnego, które kondensują, tworząc wysoce koherentną fazę. Korelacje ekscytonowe wzbogacają topologiczny diagram fazowy kwantowych spinowych izolatorów Halla, indukując fazę izolującą ze spontanicznie złamaną symetrią odwrócenia czasu, pomiędzy trywialną i nietrywialną fazą spinowego izolatora Halla. Jedną z charakterystycznych cech topologicznych przejść fazowych w bezkorelacyjnych izolatorach topologicznych jest zamykanie przerwy energetycznej. Obecność ekscytonów prowadzi jednakże do przejścia, w którym przerwa nie zamyka się. Można to interpretować jako wysiłek systemu w celu zminimalizowania energii podczas przejścia topologicznego. Istnieje wiele niedawnych obserwacji doświadczalnych wskazujących na istnienie ekscytonów w układach dwuwarstwowych, ale jak dotąd nie zaobserwowano bezpośrednio spontanicznego łamania symetrii odwrócenia czasu. W oryginalnych badaniach przeprowadzonych na potrzeby tej rozprawy proponujemy układ doświadczalny do obserwacji tej właśnie fazy uporządkowanej. Numeryczne obliczenia transportu w dysku Corbino, badające przewodnictwo w objętości i na krawędziach, potwierdzają, że topologiczne przejście fazowe odbywa się bez zamykania przerwy energetycznej. Co więcej, proponujemy również wykorzystanie układu w jego stanie ze złamaną symetrią, wraz z nadprzewodnikiem typu s, do tworzenia, badania i manipulowania stanami zerowymi Majorany. Potwierdzamy, zarówno numerycznie jak i analitycznie, istnienie stanów zerowych Majorany na gra-

---

nicy tych dwóch układów. Przedstawiamy eksperymentalną konfigurację złącza Josepha o budowie: nadprzewodnik/izolator ze złamaną symetrią/nadprzewodnik, pozwalającą zaobserwować prąd Josepha o okresie  $4\pi$ , wskazujący na stanami zerowymi Majorany zlokalizowane na interfejsach. Na koniec pokazujemy również, jak manipulować informacją kwantową przechowywaną w stanach zerowych Majorany i odczytywać stan kubit topologicznego.

---

## List of publications

1. **T. Paul**, V. Fernández Becerra, T. Hyart, Interplay of quantum spin Hall effect and spontaneous time-reversal symmetry breaking in electron-hole bilayers. I. Transport properties, Phys. Rev. B 106, 235420 (2022).
2. **T. Paul**, V. Fernández Becerra, T. Hyart, Interplay of quantum spin Hall effect and spontaneous time-reversal symmetry breaking in electron-hole bilayers. II. Zero-field topological superconductivity, Phys. Rev. B 106, 235421 (2022).

## List of oral presentations

1. **T. Paul**, V. Fernández Becerra, T. Hyart, Effect of excitons in type-II quantum wells, International meeting on superconducting quantum materials and nanodevices, April 2023, Budva, Montenegro (**Invited talk**).
2. **T. Paul**, V. Fernández Becerra, T. Hyart, Interplay of excitonic correlations, quantum spin Hall effect and superconductivity in electron-hole bilayers, Joint European Magnetic Symposia, July 2022, Warsaw, Poland (**Contributed talk**).
3. **T. Paul**, V. Fernández Becerra, T. Hyart, Interplay of excitonic correlations with quantum spin Hall effect and superconductivity, 3rd annual conference Q-MAT 2020, Kolkata, India (**Online talk**)

# Contents

<b>1</b>	<b>Introduction</b>	<b>4</b>
1.1	Quantum Hall effect . . . . .	6
1.1.1	Edge states . . . . .	8
1.1.2	Topological explanation of the perfect quantization of Hall resistance . . . . .	8
1.1.3	Other remarks . . . . .	10
1.2	Quantum anomalous Hall effect . . . . .	11
1.2.1	Haldane model in honeycomb lattices . . . . .	11
1.2.2	Qi-Wu-Zhang model . . . . .	13
1.3	The quantum spin Hall effect . . . . .	16
1.3.1	Inverted band structure . . . . .	18
1.3.2	Time reversal symmetry . . . . .	19
1.3.3	$\mathbb{Z}_2$ Topological invariant . . . . .	19
1.3.4	Quantized conductance . . . . .	20
1.3.5	Experimental signatures . . . . .	21
1.4	Role of interactions . . . . .	22
1.5	Majorana zero modes . . . . .	23
1.6	Quantum transport theory . . . . .	27
1.7	Motivation and outline . . . . .	29
1.7.1	Motivation . . . . .	29
1.7.2	Outline . . . . .	31
<b>2</b>	<b>Bernevig-Hughes-Zhang model for the quantum spin Hall effect</b>	<b>33</b>

2.1	Quantum well structure . . . . .	34
2.1.1	Type-I quantum well . . . . .	34
2.1.2	Type-II quantum well . . . . .	35
2.2	Non-interacting BHZ model . . . . .	36
2.3	Symmetries of the system . . . . .	37
2.3.1	Inversion symmetry . . . . .	37
2.3.2	Rotation symmetry . . . . .	38
2.3.3	Time-reversal symmetry . . . . .	38
2.4	Model parameters . . . . .	38
2.5	Effect of bulk inversion asymmetry $\Delta_z$ term . . . . .	39
2.5.1	Type-I quantum well . . . . .	39
2.5.2	Type-II quantum well . . . . .	41
2.6	Effect of mass asymmetry . . . . .	41
2.7	Topological Invariant . . . . .	42
2.7.1	Spin Chern topological invariant when $\Delta_z = 0$ . . . . .	43
2.7.2	$Z_2$ topological invariant when $\Delta_z \neq 0$ . . . . .	45
2.8	Effect of magnetic field . . . . .	49
2.8.1	Perpendicular magnetic field . . . . .	49
2.8.2	In-plane magnetic field . . . . .	50
<b>3</b>	<b>Interplay of excitons and the quantum spin Hall effect</b>	<b>52</b>
3.1	Excitons in Type-II quantum well . . . . .	52
3.1.1	Obtaining the exciton pairings . . . . .	54
3.2	Topological Phase transition . . . . .	56
3.3	Bulk inversion asymmetry term $\Delta_z$ . . . . .	60
3.4	Mass asymmetry . . . . .	61
<b>4</b>	<b>Paper I: Interplay of quantum spin Hall effect and spontaneous time-reversal symmetry breaking in electron-hole bilayers I. Transport properties</b>	<b>63</b>

<b>5 Paper II: Interplay of quantum spin Hall effect and spontaneous time-reversal symmetry breaking in electron-hole bilayers II. Zero-field Topological Superconductivity</b>	<b>75</b>
<b>6 Conclusion and Outlook</b>	<b>94</b>
<b>Bibliography</b>	<b>95</b>

# List of Figures

1.1	Hall resistance as a function of magnetic field . . . . .	5
1.2	Quantum Hall effect . . . . .	7
1.3	Quantum Hall effect without Landau levels . . . . .	13
1.4	Qi-Wu-Zhang model . . . . .	15
1.5	Quantum spin Hall effect in graphene . . . . .	17
1.6	Quantized conductance for Bernevig, Hughes and Zhang model . . .	20
1.7	Two-terminal setup to measure edge conductance . . . . .	21
1.8	Kitaev's chain . . . . .	25
1.9	Experimental setups to observe Majorana zero modes . . . . .	26
1.10	Quantum transport setup . . . . .	27
2.1	Type-I quantum well structure and bulk band structure . . . . .	35
2.2	Type-II quantum well structure and bulk band structure . . . . .	36
2.3	Edge spectrum of a type-I quantum well when $\Delta_z = 0$ . . . . .	40
2.4	Edge spectrum of a type-I quantum well when $\Delta_z \neq 0$ . . . . .	40
2.5	Edge spectrum of a type-II quantum well when $\Delta_z \neq 0$ . . . . .	41
2.6	Edge spectrum with mass asymmetry between electrons and holes . .	42
2.7	Spin Chern number as a function of $E_G$ . . . . .	45
2.8	The zeros of $P(k)$ lying on a curve enclosing the $\Gamma$ point, when the system is in quantum spin Hall phase. . . . .	48
3.1	Phase diagrams of $\Delta_{1,2}$ for different $g_s$ and $g_p$ . . . . .	55
3.2	Phase diagram of $\mathcal{T}_{br}$ . . . . .	57
3.3	Phase diagram of $\mathcal{P}$ . . . . .	58

3.4	Energy band dispersion . . . . .	59
3.5	Phase diagram of order parameters for different $\Delta_z$ . . . . .	60
3.6	Phase diagram for mass asymmetry . . . . .	61
3.7	Energy phase diagram in the presence of mass asymmetry . . . . .	62

# List of Tables

- 2.1 Table of parameter values used for the calculations present in this thesis for HgTe/CdTe and InAs/GaSb. Table adapted from [133]. . . 39

# Chapter 1

## Introduction

In 1879, Edwin Hall showed that, a perpendicular magnetic field applied to a thin metallic sheet, can induce an electric voltage perpendicular to the charge current [1]. Hall effect is now an important technique used to characterize semiconducting films to obtain the carrier density  $n_s$  and mobility  $\mu$  through the measurement of Hall resistance  $\rho_{xy}$  and longitudinal resistance  $\rho_{xx}$ ,

$$\rho_{xy} = \frac{B}{en_s}, \quad \text{and} \quad \rho_{xx} = 1/en_s\mu, \quad (1.1)$$

where  $e$  is the magnitude of the electronic charge and  $B$  is the magnetic field applied perpendicularly [2]. In 1980, it was experimentally shown that, a two-dimensional electron gas in the inversion layer of a silicon based MOSFET (metal-oxide semiconductor field-effect transistor) exposed to a strong magnetic field ( $> 18$  T) at low temperatures gives rise to quantized steps of Hall resistance [3]. It was also accompanied by an oscillating longitudinal resistance. The longitudinal resistance were finite-valued peaks at the transition between two Hall resistance plateaus and zero otherwise (see Fig. 1.1). This behaviour is in contrast to (1.1), where the Hall resistance is linearly proportional to  $B$  and the longitudinal resistance is a constant. Implementing the theory of Landau quantization, gave some understanding of the new observations [2]. The quantization of Hall resistance was explained as the num-

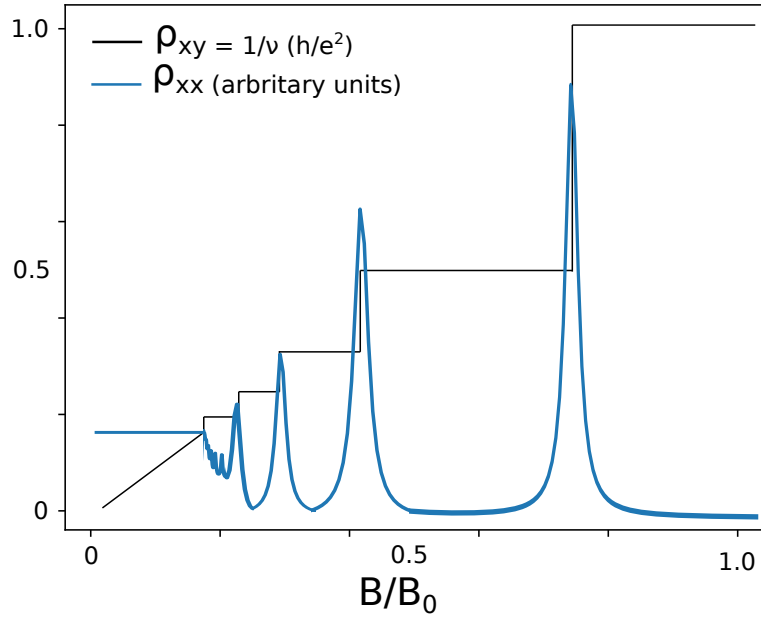


**Figure 1.1:** Schematic illustration of Hall resistance  $\rho_{xy}$  and longitudinal resistance  $\rho_{xx}$  as a function of  $B/B_0$ , where  $B_0 = n_s h/e$ , applied perpendicularly to a two-dimensional electron gas. The Hall resistance forms quantized plateaus of values  $1/\nu$  (is linear) as a function of strong (weak) applied magnetic field  $B/B_0$ . The longitudinal resistance shows oscillatory (constant) behaviour for strong (weak) magnetic field.

ber of filled Landau levels and was given by

$$\rho_{xy} = \frac{1}{\nu} \frac{h}{e^2} \implies \sigma_{xy} = \frac{e^2 \nu}{h}, \quad (1.2)$$

where the integer  $\nu = 1, 2, 3, \dots$ . The longitudinal resistance is zero when the Hall resistance is quantized and when the integer value of  $\nu$  changes, the longitudinal resistance shows finite height peaks (see Fig. 1.1). When the Fermi energy lies in between two Landau levels, the Hall resistance takes a quantized value and longitudinal resistance becomes zero. When the Fermi energy lies on a Landau level, the quantization breaks and the longitudinal resistance ceases to be zero and takes a finite value. Presence of disorder with strength smaller than the energy gap between the Landau levels, were considered essential to explain the plateau formation in Hall resistance [4, 5].

This experiment was repeated for different materials [6, 7], and the observation of a perfectly quantized Hall resistance was found to be consistent in all these experiments. The observation of the quantum Hall effect is often considered to be one of

the most significant discoveries in twentieth century physics, and von Klitzing was awarded the Nobel prize in physics in 1985 [8]. The quantum Hall effect laid a foundation for the observation of even more intricate physics like fractional quantum Hall effect [9–11], exciton condensation [12], the quantum spin Hall effect [13, 14] and quantum anomalous effect [15–17]. It has also opened up research to find non-Abelian quasiparticles that could be used in topological quantum computation [18]. The quantum Hall effect has analogies even in the study of black holes and string theory [19, 20].

Below, we will discuss the physics behind quantum Hall effect and quantum anomalous Hall effect to better understand the quantum spin Hall effect. The former two theories are crucial in understanding the topological nature of quantum spin Hall effect. We will then look into the important properties of quantum spin Hall effect, role of interactions in quantum spin Hall insulators, and its application in realizing Majorana zero modes which are useful in topological quantum processing. A short section on quantum transport theory is also included, as the method is used to calculate the bulk and edge conductance in the paper attached in Chapter 4. This will be followed by presenting the main research problems addressed in the thesis and the thesis outline.

## 1.1 Quantum Hall effect

The theory of Landau quantization of energy states [2, 21, 22] was used initially to get the expression for the quantized Hall conductance given in (1.2). However, what surprised the scientific community the most was the order of accuracy ( $\sim 10^{-9}$ ) of the Hall conductance [6, 23]. Why is a disordered sample in a quantum Hall setup producing a quantized current of such high accuracy? Moreover, Laughlin in 1981 introduced gauge invariance to explain the quantized Hall resistance [4]. He considers a flux  $\Phi$  that introduces a gauge potential going through the center of a Corbino ring in addition to the magnetic field. To see this roughly, consider that flux  $\Phi$  is slowly changing from zero to  $\Phi_0 = 2\pi\hbar/e$  over the time 0 to  $T$ . An electro-

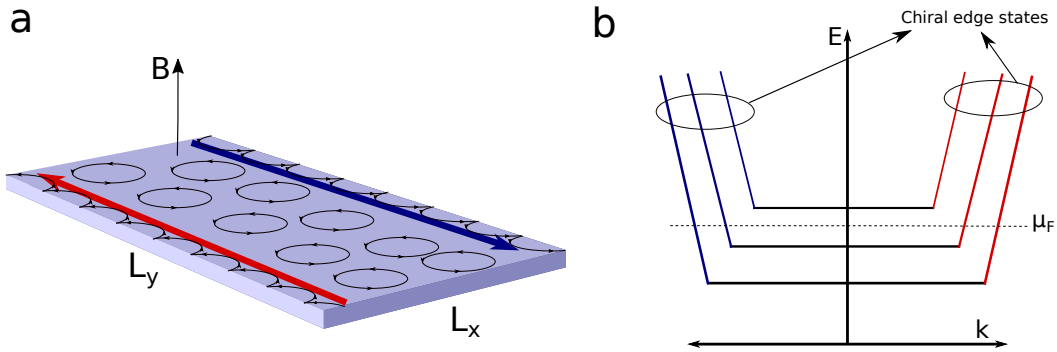


**Figure 1.2:** (a) Schematic figure depicting quantum Hall effect. The chiral edge states are shown by red and blue arrows. The classical picture of cyclotron orbits and skipping orbits at the edge is also depicted. Since the spin of the electron does not enter the equation of motion, both spin-up and spin down electrons will show the same behaviour in motion as shown in the figure. Figure adapted from [25]. (b) Schematic illustration of the energy states giving rise to the chiral edge states. Figure adapted from [2].

motive force  $\mathcal{E} = -\partial\Phi/\partial t = -\dot{\Phi}_0/T$  appears around the ring. If a fixed  $n$  number of electrons are transported from the inner edge of the ring to the outer edge of the ring, then the radial current  $I = -en/T$ , and the Hall resistance comes out to be

$$\rho_{xy} = \frac{\mathcal{E}}{I} = \frac{\Phi_0}{ne} = \frac{h}{e^2} \frac{1}{n}. \quad (1.3)$$

The above thought experiment is called *Laughlin's charge pumping* and it was experimentally proven recently using an ultracold atomic gas [24]. When  $n$  number of electrons are transferred from the inner edge to the outer edge of the ring, the bulk is considered to be gapped and longitudinal resistance is zero. Of course, this explanation is true only in the case of integer quantum Hall effect as the quasiparticles that are transferred carries electron charge. In the case of fractional quantum Hall effect, the transferred quasiparticles carry fractional charge. While Laughlin's charge pumping argument does not directly apply to the experimental setup of quantum Hall effect, it alluded to the presence of something deeper and more fundamental to the theory of quantum Hall effect [22]. Below, we will see how a combination of different approaches is required to attain clarity regarding quantum Hall effect.

### 1.1.1 Edge states

One of the interesting observations from the study of quantum Hall systems is the presence of robust, unidirectional states that move along the boundary of the material. Consider a rectangular sample which is finite in, say,  $x$  direction and is infinite in the  $y$  direction. A magnetic field  $B$  is applied perpendicular to the plane of this sample. Classically, one can see electrons make incomplete cyclotron orbits or skipping orbits at the boundary of the sample as shown in Fig. 1.2a. These skipping orbits move in opposite directions on boundaries opposite to each other. From quantum mechanics, the edge modes are explained by the presence of a confining potential. For a wide sample, along the  $x$  direction, the confining potential can look very flat in the bulk, with steep rise (fall) on the right (left) edge. This leads the electrons to move in opposite directions on the right and left edges. For a wide enough sample along the  $x$  direction, the two edge states are spatially separated and will have little overlap. Therefore, any impurity on one edge cannot scatter the electron to the opposite edge, making these edge states very robust. These unidirectional edge states are called *chiral edge states*. In the bulk, the electrons have zero drift velocity because of the very flat confining potential in the interior of the sample.

Within the edge state picture, the quantization of Hall resistance and zero longitudinal resistance is explained using the Landauer-Buttiker formalism (see Chapter 2 and 4 in Ref. [2]). The quantized Hall resistance is shown to be dependent on the number of edge states at the Fermi energy which in turn, is equal to the number of filled Landau levels. The bulk states that contribute to longitudinal resistance remain in equilibrium and hence do not contribute to transport [2].

### 1.1.2 Topological explanation of the perfect quantization of Hall resistance

Laughlin's charge pumping thought experiment and the edge state explanation of the quantized Hall conductance were followed by a work by Thouless-Kohomoto-Nightingale-den Nijs in 1982 where the quantized Hall conductance is related to a

topological invariant in two-dimensional systems [26]. In this case the quantized Hall conductance is obtained from the bulk-current density when an electric field is applied.

Consider a particle moving in a rectangular lattice, where the lattice momentum is restricted to the Brillouin zone of the reciprocal lattice [27, 28]. This Brillouin zone can also be described by a torus  $\mathbf{T}^2$  that is parameterised by  $k_x$  and  $k_y$ . Moreover, there is no electron-electron interaction present and the Fermi energy lies between the filled and unfilled bands. With these assumptions, using the Kubo formula, when an electric field  $E_x$  is applied in the  $x$  direction, the bulk current density  $j_y$  obtained will yield the Hall conductivity, given by,

$$\sigma_{xy} = \frac{ie^2}{\hbar} \sum_{\alpha} \int_{\mathbf{T}^2} \frac{d^2k}{(2\pi)^2} \langle \partial_y u_{\mathbf{k}}^{\alpha} | \partial_x u_{\mathbf{k}}^{\alpha} \rangle - \langle \partial_x u_{\mathbf{k}}^{\alpha} | \partial_y u_{\mathbf{k}}^{\alpha} \rangle. \quad (1.4)$$

Here, the sum is over occupied energy bands  $\alpha$ ,  $\partial_i$  is a shorthand-notation for  $\partial/\partial k_i$ , and  $|u_{\mathbf{k}}^{\alpha}\rangle$  is an eigenstate of the Hamiltonian corresponding to band  $\alpha$  that picks up a phase as it completes a round in the Brillouin zone [22, 29]. The integrand can be obtained using the expressions for the Berry connection and Berry curvature [30–32]. The Berry connection measures the change in gauge and is given by

$$\mathcal{A}_i(\mathbf{k}) = -i \langle u_{\mathbf{k}} | \frac{\partial}{\partial k^i} | u_{\mathbf{k}} \rangle, \quad (1.5)$$

where  $i = x, y$ . The Berry curvature is defined as the curl of the Berry connection,

$$\Omega_{xy} = \frac{\partial \mathcal{A}_x}{\partial k^y} - \frac{\partial \mathcal{A}_y}{\partial k^x} = -i \langle \partial_y u | \partial_x u \rangle + i \langle \partial_x u | \partial_y u \rangle. \quad (1.6)$$

Integration of the Berry curvature over the Brillouin zone gives us the Chern number,

$$C = -\frac{1}{2\pi} \int_{\mathbf{T}^2} \Omega_{xy}. \quad (1.7)$$

When the Chern number for each filled band  $\alpha$  is calculated and summed over, the Hall conductance which is observed in the experiments is obtained,

$$\sigma_{xy} = \frac{e^2}{2\pi\hbar} \sum_{\alpha} C_{\alpha}. \quad (1.8)$$

The summation of Chern number over all the filled bands is an integer which is termed as TKNN number and gives the value for Hall conductance. It is a topological invariant which does not change as long as the energy gap does not close [26]. Interestingly, this theory tells us that measuring Hall resistance indicates the topological state of a system. In the quantum Hall effect, the Chern number is a nonzero integer that comes from the structure of the wave functions of the Landau levels that are formed in the presence of a strong magnetic field. These equations show why the Hall resistance is an integer number that is not dependent on any details of material properties, but on a topological invariant called the Chern number. This connection between Hall conductivity and a topological invariant naturally provides an explanation why robust quantization is observed for Hall resistance. Moreover, between each Hall resistance plateau, the bulk-gap closes and leads to a peak in the longitudinal resistance as well as a change in Chern number.

### 1.1.3 Other remarks

We have presented two pictures to understand the quantized Hall conductance. The edge state picture suggests that the current is carried only by the chiral edge states at the Fermi energy, whereas the TKNN picture shows that the bulk states also participate in the quantized Hall conductance. There are also other works which give different descriptions of the spatial distribution of the current that flows in the bulk [6, 33] and along the edge [34]. By keeping the microscopic details aside, the edge state and TKNN pictures are nicely connected via *bulk-boundary correspondence*. The bulk-boundary correspondence ensures that the Chern number is equal to the number of *chiral edge states*. As long as the bulk-gap does not close, the Chern number will not change. Therefore, the edge states remain topologically protected through

the bulk [35–38], and the spatial distribution of the current does not affect the quantization of the Hall conductance.

The quantization of Hall conductance occurs at precise integers in units of  $e^2/h$ . Hence it is also called the *integer quantum Hall effect*. There also exists a *fractional quantum Hall effect*, where the quantization of Hall conductance occurs at extremely accurate fractional values due to the presence of strongly-interacting electrons [9, 11]. Robert B. Laughlin, Horst L. Störmer and Daniel C. Tsui shared a Nobel prize in 1998 for the discovery of fractional quantum Hall effect [39]. There continues to be new developments and revisions to the theory of quantum Hall effect [40, 41]. The quantum Hall effect can also be realized in three-dimensional systems, but the physics behind this effect differs from that for the two-dimensional systems [42–44]. It has also been demonstrated that the quantum Hall effect in graphene and other Dirac fermion systems can be realized at significantly higher temperatures because the energy gaps between the Landau levels are larger at a given magnetic field [45].

## 1.2 Quantum anomalous Hall effect

The observation of quantized Hall conductance in two dimensional electron gas without an external magnetic field is referred to as quantum anomalous Hall effect [46–48]. The materials exhibiting quantum anomalous Hall effect are also called Chern insulators because the topological invariant in these systems, is the Chern number which was discussed above.

### 1.2.1 Haldane model in honeycomb lattices

In 1988, F.D.M Haldane put forward a theoretical proposal to observe the quantized Hall conductance in systems with a honeycomb lattice structure, like graphene, when no net magnetic field is applied perpendicularly [15]. Honeycomb lattices have both inversion and time-reversal symmetry which leads to the valence and conduction band to meet at two corners  $K$  and  $K'$  of the Brillouin zone. Breaking one of the two symmetries will produce a gap at  $K(K')$ . In Haldane's proposal, it is argued

that there exist a suitable symmetry-breaking perturbation so that when the Fermi energy lies in the center of this gap, a quantized Hall conductance is obtained just as discussed above.

In the model, a next-nearest neighbor (NNN) hopping  $t_2$  is introduced in addition to the nearest neighbor (NN)  $t_1$  term. Moreover, the model includes a local magnetic flux density perpendicular to the unit cell such that the total flux through the unit cell remains zero. Due to this local field, the electron picks up a phase  $\phi$  when it goes to its next-nearest neighbor (see Fig.1.3a). The tight-binding Hamiltonian for this model becomes,

$$\begin{aligned}
 H(\mathbf{k}) = & 2t_2 \cos \phi \left( \sum_i \cos(\mathbf{k} \cdot \mathbf{b}_i) \right) \sigma_0 + t_1 \left( \sum_i [\cos(\mathbf{k} \cdot \mathbf{a}_i) \sigma_x + \sin(\mathbf{k} \cdot \mathbf{a}_i) \sigma_y] \right) \\
 & + \left[ M - 2t_2 \sin \phi \left( \sum_i \sin(\mathbf{k} \cdot \mathbf{b}_i) \right) \right] \sigma_z,
 \end{aligned} \tag{1.9}$$

where  $\sigma$ 's are the Pauli matrices,  $M$  is the difference in onsite energies of the two different sublattices A and B, and  $\mathbf{a}_i$  and  $\mathbf{b}_i$  are the lattice vectors between NN and NNN points. If  $t_2, M \ll t_1$ , then the above tight-binding Hamiltonian can be expanded around  $K$  and  $K'$  as

$$H_{\mathbf{K}(\mathbf{K}')} = \mp \frac{3t_1}{2} (k_x \sigma_x \pm k_y \sigma_y) + m_{\pm} \sigma_z, \tag{1.10}$$

which describes the (2+1)D Dirac Hamiltonian where,  $m_{\pm} = M \pm 3\sqrt{3}t_2 \sin \phi$  behaves like the Dirac mass term. If  $m_{\pm} \neq 0$  it induces an energy gap around  $K$  and  $K'$ .  $M \neq 0$  breaks the inversion symmetry while  $t_2 \sin \phi \neq 0$  breaks time-reversal symmetry. If  $t_2$  is positive valued, then varying  $M$  term from negative to positive values can change the sign of the Dirac mass term. A particular value of  $M$  will cancel the  $t_2 \sin \phi$  term, and the Dirac mass term will become zero. The sign of this mass term determines the value of the Hall conductivity through the relation  $\sigma_{xy} = C e^2/h$ , where

$$C = \frac{1}{2} [\text{sgn}(m_-) - \text{sgn}(m_+)]. \tag{1.11}$$

When  $t_2 \sin \phi = 0$ , then  $\text{sgn}(m_-) = \text{sgn}(m_+)$  and the time-reversal symmetry is preserved. This gapped system is adiabatically connected to a normal semiconductor which does not exhibit quantized Hall conductance. When both  $M \neq 0$  and  $t_2 \sin \phi \neq 0$ , their signs and relative strengths determine the value of  $C = \pm 1, 0$ . When  $C = 0$ , then  $m_-$  and  $m_+$  have the same sign or time-reversal symmetry is not broken.  $C$  is the Chern number determining the quantized Hall conductance. The three phases with zero Chern number and non-zero Chern number are all separated by bulk-gap closings. The bulk-gap closing forms the phase boundaries in the topological phase diagram shown in Fig.1.3b. The experimental confirmation of this model has so far been unsuccessful in stand alone two-dimensional materials with honeycomb lattice but have been shown using ultracold atoms in an optical honeycomb lattice [49].

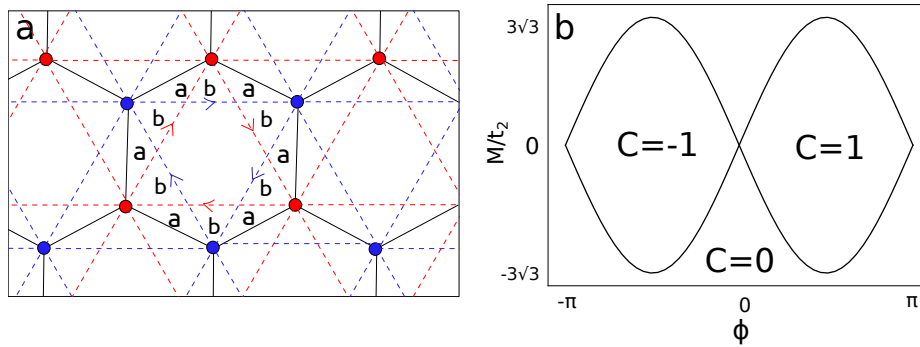


**Figure 1.3:** Schematic illustration of (a) graphene honeycomb lattice, where the solid (dashed) lines are for the nearest (next-nearest) neighbour hoppings. (b) Topological phase diagram with non-zero and zero Chern numbers separated by bulk-gap closing (in solid line). Figure adapted from [15].

### 1.2.2 Qi-Wu-Zhang model

In 2005, Qi-Wu-Zhang proposed a model to realize quantum anomalous Hall effect in semiconductors [16]. They considered a minimal, two-band model on a square lattice in the low energy range around  $\mathbf{k} = 0$ . The model they considered is a massive Dirac Hamiltonian given by,

$$h(\mathbf{k}) = \sum_{a=1,2,3} d_a(\mathbf{k})\sigma^a, \quad (1.12)$$

where  $\sigma$ 's are the Pauli matrices and  $\mathbf{k} = (k_x, k_y)$  is the Bloch wave vector of the electron. The two bands depends on the system considered, for example, it could be from spin or orbital degrees of freedom. By defining the unit vector  $\hat{\mathbf{d}}(\mathbf{k}) = \mathbf{d}(\mathbf{k})/|\mathbf{d}(\mathbf{k})|$ , the TKNN formula introduced previously becomes [16],

$$\sigma_H = \frac{e^2}{h} \frac{1}{4\pi} \int dk_x \int dk_y \hat{\mathbf{d}} \cdot \left( \frac{\partial \hat{\mathbf{d}}}{\partial k_x} \times \frac{\partial \hat{\mathbf{d}}}{\partial k_y} \right). \quad (1.13)$$

The unit vector  $\hat{\mathbf{d}}(\mathbf{k})$  is a mapping from the momentum space to the unit vector in a sphere. The integrand in (1.13) is therefore, the Jacobian of the mapping  $\mathbf{T}^2 \rightarrow \mathbf{S}^2$  [22, 36]. The full integration in (1.13) yields an integer multiple of the covered surface area [46]. This gives the expression  $\sigma_H = Ce^2/h$  for the minimal model, where the integer  $C$  is the Chern number. It is possible to obtain non-zero values of  $C$ , by choosing the appropriate expressions for  $d_a(\mathbf{k})$  around the  $\Gamma$  point in the Brillouin zone,

$$d_x = Ak_x, \quad d_y = -Ak_y, \quad d_z = M + B(k_x^2 + k_y^2), \quad (1.14)$$

where  $A$ ,  $B$  and  $M$  are material-dependent parameters. When the above expressions are expanded around  $\mathbf{k} = 0$ , for  $B = 0$ ,  $M$  is the Dirac mass. In the general case when  $B \neq 0$ ,  $\hat{\mathbf{d}} = \text{sign}(M)\hat{z}$  for  $k = 0$  and  $\hat{\mathbf{d}} = \text{sign}(B)\hat{z}$  for  $\mathbf{k} \rightarrow \infty$ . Therefore, the sign of the ratio  $M/B$  determines the topological phase. For  $M/B < 0$ ,  $\hat{\mathbf{d}}$  points in opposite direction at  $k = 0$  and  $k \rightarrow \infty$ , whereas for intermediate values of  $k$ ,  $\hat{\mathbf{d}}$  tilts and winds around  $k = 0$ . Therefore,  $\hat{\mathbf{d}}$  covers the whole surface area of the unit sphere, giving  $C = 1$ . For  $M/B > 0$ ,  $\hat{\mathbf{d}}$  points in the same direction at  $k = 0$  and  $k \rightarrow \infty$ . Therefore, for other values of  $k$ ,  $\hat{\mathbf{d}}$  does not have a winding number, as it first covers and then uncovers the same surface area and hence results in  $C = 0$  [16].  $M/B < 0$  ( $M/B > 0$ ) has inverted (normal) band structure, where the valence (conduction) band lies above the conduction (valence) band (see section 1.3.1), and are topologically distinct [46]. The inverted band structure supports chiral edge states (see Fig. 1.4). The topological transition between the two phases occurs at  $M = 0$  when the bulk-gap closes. From the bulk-boundary correspondence, the number of edge states is equal to the Chern number.

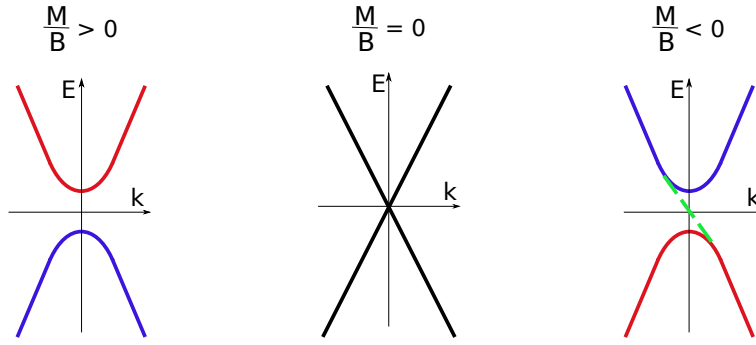


**Figure 1.4:** Schematic illustration when the energy band structure (a) is normal, (b) has zero bulk-gap, (c) is inverted. The inverted band structure is topologically non-trivial and supports chiral edge states (in green) on the boundary of the two-dimensional material. Figure adapted from [48].

In Haldane and Qi-Wu-Zhang models, there are no Landau levels to explain the quantization of Hall conductivity. The non-zero quantized Hall conductivity appears when time-reversal symmetry is broken and there is an associated change in the sign of mass term or band inversion is present. The model proposed by Qi-Wu-Zhang is experimentally more realistic, as it can be based on quantum spin Hall insulators (see section 1.3) with broken time-reversal symmetry (see section 1.3.2). In particular, it is known that some materials with strong spin-orbit coupling can exhibit inversion of bands. Moreover, the breaking of time-reversal symmetry could be done by using ferromagnetic insulators or magnetic doping. The change in the sign of the mass term could be achieved by varying some tunable parameter. The first successful realization of quantum anomalous effect was in Chromium doped  $(\text{Bi,Sb})_2\text{Te}_3$  [17]. Various Moiré materials like twisted bilayer graphene,  $ABC$  trilayer graphene on  $h$ -BN and transition metal dichalcogenide bilayer moiré superlattices have shown quantum anomalous Hall effect [50–52]. Magnetically doped topological insulator films have also been used to realize this effect [53]. So far, the best accuracy of the observed anomalous Hall conductance in experiments is on the order of  $10^{-6}$  [47, 54, 55]. It has been shown experimentally that as longitudinal resistance obtains a peak value, the Chern number and the associated Hall conductance changes [56].

### 1.3 The quantum spin Hall effect

In the above discussion, the role of spin was not considered via spin-orbit coupling. When each copy of the spin is introduced into Hamiltonian, like in (1.15), the time-reversal symmetry of the total Hamiltonian is preserved and there appears another topological state called the quantum spin Hall state [13, 57–62]. The first toy model was proposed by Kane and Mele for graphene [63]:

$$H = \begin{pmatrix} H_{\uparrow}(\mathbf{k}) & \lambda(\mathbf{k}) \\ \lambda^{\dagger}(\mathbf{k}) & H_{\downarrow}(\mathbf{k}) \end{pmatrix}. \quad (1.15)$$

Here  $H_{\uparrow(\downarrow)}$  is the Hamiltonian introduced by Haldane but with a fixed spin [15] denoted in the subscript and  $\lambda$  is a matrix that couples the two spin-sectors. From time-reversal symmetry,  $\lambda(\mathbf{k}) = \lambda^T(-\mathbf{k})$ . Moreover,  $H_{\uparrow}$  and  $H_{\downarrow}$  are time-reversed copies of each other and  $H_{\downarrow} = H_{\uparrow}^*(-\mathbf{k})$ . It is found that, inside the energy gap opened by the spin-orbit interaction around the Fermi level, there appears a state that connects the  $K$  and  $K'$  point in the positive direction in the energy  $E$  vs  $k$  spectrum. Due to time-reversal symmetry, there also appears a state of the second spin that connects  $K'$  to  $K$  in the negative direction of  $k$  in the energy spectrum. The two edge states cross at special points in the Brillouin zone (see Fig. 1.5).

These edge states are called as *helical edge states* and appear on the edge of a two-dimensional sample while the bulk remains insulating [63]. The crossing of the edge states is facilitated by translation and time-reversal symmetry present in graphene. The crossing points are called TRIM (time-reversal invariant momenta) points in the Brillouin zone [37]. For a zigzag edged graphene nanoribbon, the crossing occurs at  $k = \pi$  whereas for an armchair edge, the crossing is at  $k = 0$  [63].

When  $\lambda = 0$ , the spin-sectors are not coupled and  $S_z$  is a conserved quantity. Each spin sector is a sub Hamiltonian that is a quantum anomalous Hall insulator (see section 1.2), and therefore a non-zero Chern number can be calculated for them. Because the spin-sectors are related by time-reversal symmetry, the Chern numbers are equal in magnitude and opposite in sign. The sum of the two Chern numbers give zero charge Hall conductance whereas the difference gives a finite and quantized

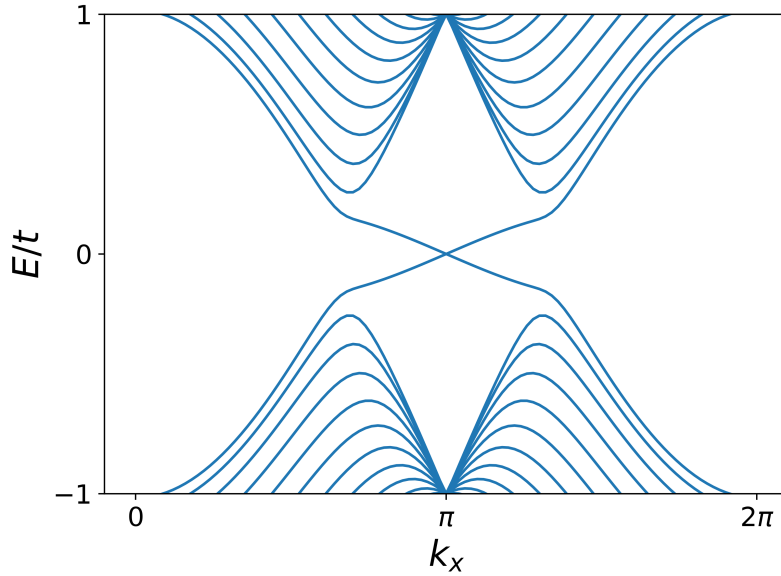


**Figure 1.5:** Schematic illustration of crossing of the helical edge states at  $k_x = \pi$  for a graphene nanoribbon with zigzag edges in quantum spin Hall phase. Figure adapted from [63].

value for spin Hall conductance. An example of this calculation is presented in the next chapter for HgTe/CdTe quantum well.

When  $\lambda \neq 0$ , there is coupling between the two spin-sectors. In graphene this could be due to the Rashba coupling [63], and  $S_z$  is no longer a conserved quantity. One cannot calculate the Chern number separately as in the previous case. In order to identify the topological state, a  $Z_2$  topological invariant is calculated by Kane and Mele in a separate paper [64]. In the quantum spin Hall state, it is found that up to a certain strength, the crossing of the helical edge states was not lifted and the system remained in quantum spin Hall state [63]. This topological invariant counts the number of pairs of gapless modes on each edge. This will be discussed in more detail later.

In both cases, the importance of time-reversal symmetry is established. As long as the time-reversal symmetry is not broken, the helical edge states will cross at a TRIM point in the Brillouin zone. However, experimentally observing this topological phase in graphene is difficult because of the small energy gap ( $\sim 10^{-3}$  meV) opened by the very weak spin-orbit coupling in graphene [65, 66]. A small bulk-gap may allow even a weak perturbation to close the bulk-gap and destroy the edge states, so

a large bulk-gap is favourable.

In an independent work, Bernevig, Hughes and Zhang (BHZ) proposed an alternative model to realize quantum spin Hall state [13]. The BHZ model, also can be thought of as two copies of the Qi-Wu-Zhang model for each spin. The helical edge states appear, when the bands are inverted, as was briefly discussed in section 1.2.2. Moreover, the model was proposed for a HgTe/CdTe quantum well, where the strong spin-orbit coupling opens a large gap in the energy band spectrum. This allows for an experimental observation of these edge states as they are protected by a large gap from the bulk states. The change in the sign of the mass term in the massive Dirac Hamiltonian for this heterostructure, is brought upon by varying the width of the quantum well. This theoretical proposal was followed by an experimental confirmation [14]. In this thesis, only BHZ like models, that can be described by a massive Dirac Hamiltonian will be considered. The BHZ model will be discussed in more detail in the next chapter for two types of quantum wells, for the cases where spin-sector coupling is absent [13] and present [60]. Below, we discuss some important properties of quantum spin Hall insulators.

### 1.3.1 Inverted band structure

In the BHZ model, one of the most important conditions to host the quantum spin Hall phase is to drive the system to have an inverted band structure. In the Qi-Wu-Zhang model [16], when the mass term  $M > 0$ , the system has a normal progression of bands, meaning that the electron-like band lies above the hole-like band, with a positive energy gap. This is adiabatically connected to a trivial band insulator where the conduction band lies above the valence around the Fermi energy. When  $M < 0$ , the electron like band lies below the hole like band, and this results in an energy gap with a negative sign. This is the inverted band structure and is found in materials with very strong spin-orbit coupling. The two regimes are separated by a bulk-gap closing at  $M = 0$  and hence are topologically different. In the inverted band regime, the system behaves like a quantum spin Hall insulator. This will be discussed in detail in Chapter 2.

### 1.3.2 Time reversal symmetry

The time-reversal symmetry  $\mathcal{T}$  operator for spin 1/2 particles is anti-unitary. The operator  $\mathcal{T} = \tau\mathcal{K}$  is a product of a unitary operator  $\tau$  and a complex conjugate operator  $\mathcal{K}$ . Let's say there is a state  $|\psi\rangle$  with say, spin-up and it's time-reversed partner with same energy, is  $|\mathcal{T}\psi\rangle$  with spin-down. When  $\mathcal{T}^2 = -1$ , we get  $\tau\tau^* = -1$  which implies that  $\tau = -\tau^T$ . We have,

$$\langle\psi|\mathcal{T}\psi\rangle = \sum_{i,j} \psi_i^* \tau_{ij} \mathcal{K}\psi_j = \sum_{i,j} \psi_i^* \tau_{ij} \psi_j^* = - \sum_{i,j} \psi_i^* \tau_{ji} \psi_j^* = - \sum_{j,i} \psi_j^* \tau_{ji} \mathcal{K}\psi_i = -\langle\psi|\mathcal{T}\psi\rangle. \quad (1.16)$$

The above condition is possible only if  $|\psi\rangle$  and  $|\mathcal{T}\psi\rangle$  with the same energy are orthogonal to each other. This is called *Kramer's degeneracy* and the two states are called *Kramer's pair*. The counter propagating edge states that realise at the edge of the quantum spin Hall insulator is a Kramer's pair. As long as the time-reversal symmetry is protected, backscattering from disorder or interaction from one spin-up channel to the spin-down channel along the same edge is not possible as doing so would need the backscattered electron to flip its spin. Even when a TRS obeying impurity can flip the spin, it still cannot cause backscattering. Let's assume that there is an arbitrary disorder potential  $U_{\text{dis}}$  obeying time-reversal symmetry  $\tau U_{\text{dis}}^T \tau^\dagger = U_{\text{dis}}$ . Then the perturbation does not couple the Kramer's partners because  $\langle\psi|U_{\text{dis}}\tau\mathcal{K}|\psi\rangle = 0$  i.e. the matrix element of  $U_{\text{dis}}$  between the Kramer's partners vanishes. The proof is similar as the calculation above. In other words, time-reversal symmetry is a crucial ingredient to protect helical edge states in these topological materials [64, 67, 68].

### 1.3.3 $\mathbb{Z}_2$ Topological invariant

As briefly mentioned before, there is a need for another topological invariant that identifies the quantum spin Hall phase when there exists a coupling between the two spin-sectors of the Hamiltonian. The closing of the bulk-gap in such materials comes with a difference in the number of Kramer's pairs of 1. This means one can use topological invariant  $\nu$  which has a  $\mathbb{Z}_2$  classification, meaning it can take two values which counts odd or even number of Kramer's pairs [13, 64, 69]. By relating

$\nu$  to the parity of the number of edge states nesting in the bulk-gap, we get

$$\nu = \frac{N(E)}{2} \pmod{2}. \quad (1.17)$$

Here  $N(E)$  are the total number of energy states that crosses the Fermi energy. A more detailed discussion on the  $Z_2$  topological invariant is presented in Chapter 2 for the Bernevig, Hughes and Zhang model.

### 1.3.4 Quantized conductance

A signature of odd (even) number of helical pairs along the edge for the quantum spin Hall (normal) phase is also reflected in conductance measurements. For the BHZ model, the two-terminal quantized conductance goes from 0 (no helical pair) to  $2G_0$  (one helical pair) where  $G_0 = e^2/h$  as the system transitions from trivial to quantum spin Hall insulator. As has been discussed, the quantum spin Hall state is characterized by odd number of helical edge states, which carry opposite spins in opposite directions. In Ref. [13], a multi-terminal setup is also proposed for additional confirmation of helical edge states.

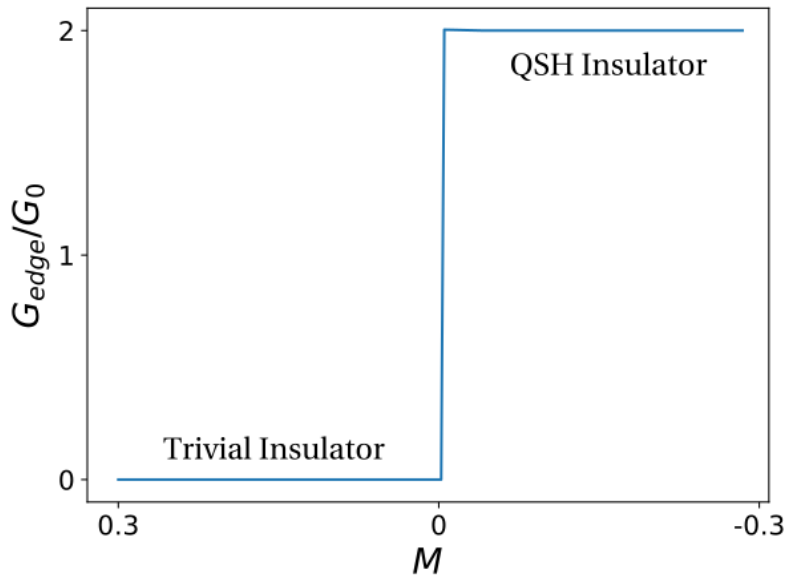


**Figure 1.6:** Behaviour of edge conductance in trivial and quantum spin Hall phase as a function of the Dirac mass term.

### 1.3.5 Experimental signatures

The proposed candidate material HgTe/CdTe by Bernevig-Hughes-Zhang to observe quantum spin Hall effect has been studied extensively [13]. Below we list experimental measurements that were carried out to confirm the properties characteristic of a quantum spin Hall insulator [14, 70–72].

When a magnetic field is applied perpendicularly to the two-dimensional sample, the features of the Landau level spectrum indicate whether the system has trivial or inverted band structure. In the normal regime, like most materials, the Landau levels shift to higher energies with increasing magnetic field. In the quantum spin Hall phase, due to the presence of an inverted band structure, the electron (hole)-like subband shifts to higher (lower) energies with increasing magnetic field. This leads to the two Landau levels to cross at some critical value of the magnetic field. The crossing of the Landau levels is characteristic of inverted band structures [14]. In order to test the presence of time-reversal symmetry that is essential for quantum spin Hall insulators, a perpendicular and in-plane magnetic field are applied. Even for weak strengths of perpendicular field, the edge conductance decreases quickly with increasing magnetic field. On the other hand, for an in-plane magnetic field, the edge conductance decreases more slowly with increasing magnetic field. The decrease of conductance demonstrates that the protection of edge states is lost due to breaking of time-reversal symmetry [14, 58, 59]. As will be discussed in the next chapter, when the spin sectors are coupled, the response of an in-plane magnetic field differs greatly from the case when the two spin-sectors are not coupled.

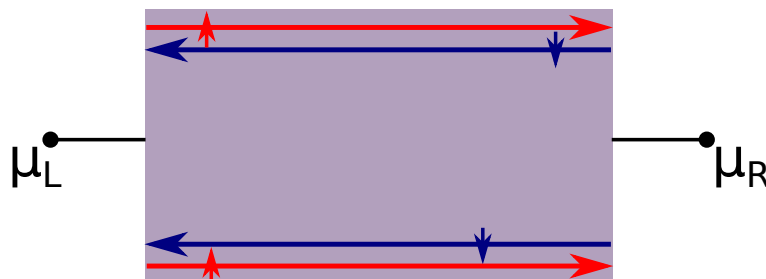


**Figure 1.7:** Sketch of a pair of helical edge states in a quantum spin Hall insulator. Bulk states are absent in the the figure given that in a quantum spin Hall insulator the bulk remains insulating. A two-terminal conductance measurement between  $\mu_L$  and  $\mu_R$  yields  $G_{LR} = 2e^2/h$ . Figure adapted from [13].

In the absence of magnetic fields, the presence of helical edge states is probed by measuring the edge conductance in a two terminal setup (see Fig. 1.7), the conductance measured is quantized with value  $2e^2/h$  in the quantum spin Hall phase and zero conductance in the trivial phase. The argument that the contribution to the measured conductance is only from the edge states and not from the bulk is checked by measuring the longitudinal conductance by changing the width of the sample. Since, the width of the sample does not affect the measured quantized conductance, it is concluded that the bulk does not participate in the transport and only edge states do [14]. The quantized edge conductance in quantum spin Hall phase is confirmed in the presence of a disordered sample [71] or when both interactions and disorder are present [68]. The transport measurements have been performed in two and four terminal setups [73]. The current is also known to flow through the bulk of the sample while the edge conductance remains quantized [70, 72]. The edge currents have also been observed in imaging experiments [72, 74]. The dissipationless, helical edge states have only been seen in short samples [14, 70, 73, 75]. In long samples, the edge conductance takes values lower than the quantized value [14, 70, 71, 76, 77]. To understand why the edge conductance is not perfectly quantized when time-reversal symmetry is present, effect of magnetic impurities [78, 79], disorders and interactions [68, 80–85] have been considered.

## 1.4 Role of interactions

As mentioned before, one of the reasons for the lack of topological protection of the edge states in these materials, which is important to be studied is the effect of Coulomb interactions.

The non-interacting theory predicts that in quantum spin Hall insulators, a large magnetic field closes the bulk-gap leading to an indirect semimetal phase [86]. In contradiction to this, it was found that in the type-II quantum wells such as InAs/GaSb, the quantization was found up to a large magnetic field of 10T [70]. This suggests that interaction effects should be considered to explain such obser-

vations. Moreover, in the absence of magnetic field, it has been observed that the longitudinal resistance is linearly growing with the device length and the mean free path is also temperature independent. This is in contradiction to the topological protection of helical edge states against elastic backscattering when time-reversal symmetry is preserved. However, in the light of interaction effects that break time-reversal symmetry spontaneously, the temperature independence of the mean free path could be understood. The InAs/GaSb quantum well, is a well studied candidate to observe exciton condensation [87]. To put it simply, electrons from the conduction band and holes from the valence band can form bound states called excitons. These excitons can also form a condensate in certain conditions. Therefore, the role of excitons could be explored to study the low accuracy of the quantization observed in quantum spin Hall insulators. There are several recent experimental evidences of the presence of excitons in InAs/GaSb [88–92] and WTe<sub>2</sub> [93–95]. It has also been shown theoretically that excitons are important in HgTe/CdTe bilayers [96]. We will look into the role of excitons in InAs/GaSb quantum wells in more detail in Chapter 3 of this thesis.

## 1.5 Majorana zero modes

In solid-state systems, Majorana zero modes (MZMs) are highly localized quasiparticles with zero energy and fundamentally different from electrons and bosons. Upon an interchange of two electrons (bosons) the many-particle wavefunction acquires a factor of -1 (1). For a degenerate state of Majorana zero modes, the factor is in general a matrix, which makes these quasiparticles a manifestation of non-Abelian anyons [97–101] and their statistics is non-Abelian [102, 103]. This interesting property make the system supporting MZMs a viable candidate for topological quantum information processing. Additionally, MZMs are described by operators which are self-adjoint and square to 1 [97]:

$$\gamma = \gamma^\dagger, \implies \gamma^2 = 1, \quad (1.18)$$

$$[H, \gamma] = 0. \quad (1.19)$$

The localization of MZMs is determined from (1.19) [97]. The operator  $\gamma$  is considered as half a fermion, which means that two MZMs  $\gamma_1$  and  $\gamma_2$  can be combined to make one fermionic state  $f = (\gamma_1 + i\gamma_2)/2$  with a possible occupation of zero or one [98]. The two MZMs are related by the following anti-commutation rule:

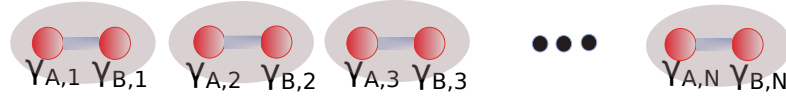
$$\{\gamma_i, \gamma_j\} = 2\delta_{ij}. \quad (1.20)$$

These quasiparticles have been theoretically shown to be present in spinless p-wave superconductors [98, 101]. More precisely, they will appear at the end of a spinless p-wave superconducting one dimensional chain and at vortices or defects of a two-dimensional  $p + ip$  superconductor (see Chapter 16 in Ref. [36] for a detailed discussion). Experimental realization of MZMs in solid state systems would confirm the existence of particles that are their own antiparticles, first proposed by Ettore Majorana [104], and allow to observe non-Abelian statistics [102, 103]. Their experimental confirmation would then pave the way for practical applications in quantum computing but also for developing fundamental theories in physics. This makes the study to realize MZMs in solid state systems an active research field in condensed matter physics.

There are some naturally occurring materials that in principle can host MZMs, but so far there are no experimental observation of their topological phase [105, 106]. Hence, the scientific community have resorted to artificially creating a spinless p-wave superconductor, which in its topological phase will host Majorana zero modes. The one-dimensional toy model is the Kitaev chain of length  $N$  [107], given by:

$$H = \sum_j \left[ -t(c_j^\dagger c_{j+1} + c_{j+1}^\dagger c_j) - \mu \left( c_j^\dagger c_j - \frac{1}{2} \right) + \Delta c_j c_{j+1} + \Delta^* c_{j+1}^\dagger c_j^\dagger \right]. \quad (1.21)$$

(a) Strong pairing : Trivial phase



(b) Weak pairing : Topological phase

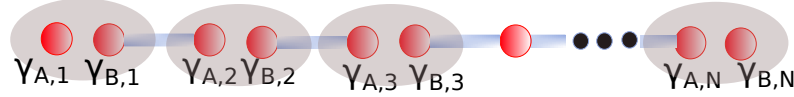


**Figure 1.8:** Schematic illustration of one-dimensional Kitaev's chain in two different topological regimes. (a) In the strong pairing, the on-site couplings dominate and there are no end states, hence is the trivial phase. (b) In the weak pairing phase, there appears unpaired MZMs at the end of the chain. The weak pairing phase becomes the topological regime. Figure adapted from [98]

where  $c$  and  $c^\dagger$  are fermionic annihilation and creation operators respectively. Each fermionic site  $j$  can be occupied by a pair of MZMs at subsites  $A$  and  $B$ :

$$\gamma_{A,j} = c_j + c_j^\dagger, \quad \gamma_{B,j} = \frac{c_j - c_j^\dagger}{i}. \quad (1.22)$$

Using the above relations, we can re-write the Hamiltonian (1.21) in terms of the Majorana operators  $\gamma$ . When  $|\Delta| = t = 0$  and  $\mu < 0$ , there is strong coupling between the MZMs at subsites  $A$  and  $B$  of the same site  $j$ . When  $|\Delta| = t > 0$  and  $\mu = 0$ , there is coupling between the MZMs at the neighbouring sites, this is also called the weak pairing regime. In the weak pairing regime, MZM are localized at the ends of the chain (see Fig. 1.8). A  $\mathbb{Z}_2$  topological invariant can be define which calculates the parity of the ground state. If the ground state is a superposition of even (odd) number of fermions, the parity is even (odd). In the topological (trivial) phase, the parity is odd (even) [107].

With the discovery of topological insulators, a way to capture Kitaev's toy model and realize MZMs was introduced [108–110]. These models make use of a topological insulator in proximity with an s-wave superconductor when a magnetic field is applied or the system is interfaced with a ferromagnetic insulator. The model can be considered to have the following components [98]:

$$H = H_{TI} + H_Z + H_{SC}. \quad (1.23)$$

The first component is the Hamiltonian for a topological insulator with strong spin-orbit coupling, which is needed to achieve the effective spinless p-wave superconductivity and necessary to obtain Majorana zero modes. The second Hamiltonian introduces broken time-reversal symmetry which is required to obtain unpaired localized MZMs (otherwise MZMs would necessarily come in time-reversed pairs). The third component is the Hamiltonian for an s-wave superconductor, which introduces particle hole symmetry and makes it possible to realize particles that are their own antiparticles.

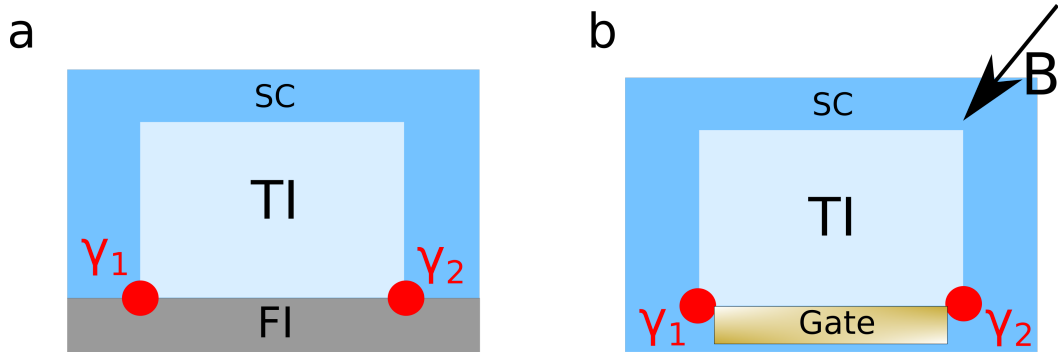


**Figure 1.9:** Schematic illustration of experimental setup to realize Majorana zero modes at (a) the interface of s-wave superconductor (SC), a two-dimensional topological insulator (TI) and ferromagnetic insulator (FI). At the interface of (b) s-wave superconductor (SC), two-dimensional topological insulator (TI) and a Zeeman field with electrostatic gating. [98].

Presently, there are several different indicators which help in confirming the existence of Majorana zero modes like zero-bias tunneling [111, 112],  $4\pi$  Josephson effect [113, 114] and quantum interferometry methods [115]. However, realizing Majorana zero modes has not been an easy quest as it requires high quality of sample, very low temperature, high strengths of magnetic field and perfect interfacing between materials [97, 116–118]. There have been several experiments which pointed to the realization of Majorana zero modes [115, 119–123], but there still lacks an unambiguous observation of these elusive quasiparticles. Therefore, the design of a system for realization of MZMs becomes an additional motivation for our paper attached in Chapter 5.

## 1.6 Quantum transport theory

We present here the quantum transport theory which is used to calculate the conductance through a sample. The numerical package Kwant [124] is used to calculate bulk and edge conductance in Paper I [125]. Kwant also implements the following theoretical model to calculate conductance. Let us consider the simplest setup where the conductance through a sample is measured using two terminals. The sample is connected to two contacts through two ideal waveguides called leads, as schematically shown in Fig.1.10.

The contact is an electron reservoir which is in thermal equilibrium but have dif-



**Figure 1.10:** Schematic illustration of a two-terminal setup to calculate conductance through a sample. The leads here are ideal waveguides which are connected to electron reservoirs called contacts. Figure adapted from [2].

ferent value of Fermi energies, say  $\mu_1$  and  $\mu_2$  and the difference between the Fermi energies is equal to the voltage. The interface between the contact and the lead is perfect. Also, the states moving to the right (left) have thermal distribution of the left (right) contact.

When the sample is not a clean system and contains impurities, it can be represented in the form of the scattering matrix. We start by solving the Schrodinger's equation of the sample and obtaining the asymptotic wavefunctions in both directions [126]. Only the propagating waves of the wavefunctions obtained, contribute to the conductance. The proportionality coefficients that measure the amplitude of the waves that emerge from the contacts in the two leads and of the waves that are transmitted through or reflected back from the sample in each lead, are obtained. These

coefficients are combined to form a scattering matrix  $\hat{s}$  that has the form

$$\hat{s} = \begin{pmatrix} \hat{r} & \hat{t}' \\ \hat{t} & \hat{r}' \end{pmatrix}. \quad (1.24)$$

The *reflection* matrix  $\hat{r}$  ( $\hat{r}'$ ) contains all the electron reflections to the left (right) lead. The *transmission* matrix contains transmission of electrons through the sample. Let us first consider that there is only one open channel in the two leads. For the lead 1 that connects contact 1 and the sample, there are right-moving states that emerge from contact 1 and are partially reflected back from the sample and then there are the left-moving states that arrived from contact 2 and were partially transmitted through the sample. The probability of the reflected (transmitted) states in the lead is  $R = |r|^2$  ( $T' = |t'|^2$ ). From the unitarity of the scattering matrix it follows that  $1 - R = T = T'$ . The current that flows in lead 1 is,

$$I = \frac{e}{h} \int dE T(E) [f(E - \mu_1) - f(E - \mu_2)], \quad (1.25)$$

where  $f(E)$  is the Fermi distribution at energy  $E$ , and  $\mu_1$  and  $\mu_2$  are the chemical potentials in the left and right lead respectively. Using  $\mu_1 = eV$  and  $\mu_2 = 0$  (Fermi energy chosen to be 0), one easily sees from Eq. (1.25) that the voltage-dependent differential conductance  $G_d(V) = dI/dV$  is given by

$$G_d(V) = \frac{e}{h} \int dE T(E) \frac{df(E - eV)}{dV}, \quad (1.26)$$

so that at zero temperature

$$G_d(V) = \frac{e^2}{h} T(E = eV). \quad (1.27)$$

This formula is the reason why we can probe the energy-dependent (voltage-dependent) transmission via the differential conductance. When there are more open channels

in the lead, then the generalized form of the conductance is,

$$G_d(eV) = \frac{e^2}{h} \sum_{n=1}^M T_n(E = eV), \quad (1.28)$$

where  $M$  is the total number of open channels in the lead and  $T_n$  are the eigenvalues of the transmission matrix  $tt^\dagger$  [37]. This is called the *Landauer formula*, which calculates the current across a sample in a two-terminal setup. To summarise the idea, the conductance is obtained from calculating the current flowing in a lead. The lead contains reflection and transmission coefficients of the states that are partially reflected and transmitted from (through) the sample. For a multi-lead setup, the current measured at one lead is obtained from summing over the contribution from all leads. This is known as *Landauer-Buttiker formula*. See [2, 37, 124, 126] for a detailed discussion and subtleties. A generalization of this approach to obtain differential conductance in normal-superconducting interfaces by using Andreev reflection also exists, and is called the *Blonder-Tinkham-Klapwijk formula* [127].

## 1.7 Motivation and outline

### 1.7.1 Motivation

So far we have looked at examples where a topological quantum phase transition takes place to give rise to interesting physics. The classification of phases in such examples relies on a topological invariant, which remains constant despite the system undergoing adiabatic changes. Typically, the topological invariant changes when the bulk-gap closes in the energy spectrum. The zero bulk-gap separates the phase diagram into states with non-zero bulk-gap and with different topological invariant. Based on the value of the topological invariant, one can identify the topological phase from a trivial one. As we have discussed, as long as no relevant symmetries have been broken, the topological phases hosts several interesting properties like a conducting edge with an insulating bulk, quantized conductance etc., which remain insensitive to perturbations. The closing of bulk-gap in these examples is akin to the

act of making a hole in the topological space.

We also point out that the accuracy of the quantization of conductance measured in quantum spin Hall experiments is significantly smaller than the accuracy measured for quantum Hall or quantum anomalous Hall materials. One of the sources for such low accuracy could be many-body interactions. The study of interactions in these systems serve two purposes - first, it may provide the reason to why the perfect quantization of edge conductance is not observed in such topological insulators. Second, it allows a way for the system to achieve topological phase transition *without* bulk-gap closing. This can be understood as an effort by the system to minimize energy during the topological phase transition.

We will be looking into the application of the BHZ model to InAs/GaSb double quantum well. This material goes from a trivial state to a quantum spin Hall state as a function of front and back gate voltages or as a function of the well width. In its topological phase, the material exhibits quantized edge conductance which is not destroyed even if a magnetic field of 10T is applied for short samples. Moreover, for long samples, the longitudinal resistance is linearly increasing with the sample length for zero magnetic field. The observation of a finite mean free path constant for a wide range of temperature of 20mK to 4.2K [70–72], called for an investigation of elastic backscattering effects in this material. For this reason, the role of excitons that arise when Coulomb interactions are introduced into InAs/GaSb quantum spin Hall insulator [85] is considered. This work shows through a mean-field approach, that the excitons gives rise to an insulating phase with spontaneously broken time-reversal symmetry. This insulating phase lives in between the trivial and quantum spin Hall phase in the topological phase diagram. There are several other works that confirm that there appears signatures of excitons in quantum Hall [128–131] and quantum spin Hall systems [88, 93–95]. However, there lacks an unambiguous observation of this insulating phase that arise due to excitons in quantum spin Hall insulators. We propose an experimental setup to observe this insulating phase that leads to a topological phase transition with no bulk-gap closing.

From the discussion on the Majorana zero modes before, we know that in order to

observe them, we need materials with strong spin-orbit coupling, proximity to superconductors to have particle-hole symmetry and breaking of time-reversal symmetry to lift Kramer's degeneracy to obtain well-localized Majorana zero modes. So far in the experimental setups, the time-reversal symmetry is broken by using a magnetic field or using ferromagnetic insulators. However, a strong magnetic field, which is often needed in these setups, is detrimental to superconductivity. Moreover, there is a lack of good interfacing between ferromagnetic and quantum spin Hall insulators. Therefore, an experimental observation of Majorana zero modes in two-dimensional materials is still missing. We can mitigate both the problems by utilizing the spontaneously broken time-reversal symmetry phase to realize Majorana zero modes. When superconductivity is induced through proximity to InAs/GaSb quantum well in time-reversal symmetry broken phase, we could observe the coveted Majorana zero modes. Further, we could use this system to experimentally observe Majorana zero modes as well by using a Josephson junction.

Therefore, the main questions that we address in this thesis are:

1. Can we propose an experimental setup to probe the appearance of exciton induced insulating phase with spontaneously broken time-reversal symmetry that appears in between the trivial and quantum spin Hall phase?
2. Can we use the excitons that break time-reversal symmetry to realize Majorana zero modes without using a ferromagnet or magnetic field?
3. If yes, how can one observe the Majorana zero modes experimentally?

### 1.7.2 Outline

In Chapter 1, we have given an overview of key theories which are important to understand quantum spin Hall effect. We have also discussed the motivation behind addressing the research problems considered in this thesis.

In Chapter 2, we will discuss the Bernevig-Hughes-Zhang (BHZ) model which describes quantum spin Hall effect in two-dimensional materials like type-I and type-II

quantum wells. Even though the two materials are described by the same BHZ models, we see interesting physics that arise out of the differences between the two types of quantum wells. We look at the energy band diagrams, the choice of topological invariant and the effect of magnetic field in the two types of quantum wells.

In Chapter 3, we argue that Coulomb interactions that lead to the formation of excitons can only be observed in type-II quantum wells. We include the Coulomb interactions into the BHZ model for type-II quantum wells and discuss the findings. We proceed to show that there exists an unconventional topological transition *without* bulk-gap closing as a result of interactions in these quantum wells.

In Chapter 4, the first paper that addresses the first research question is attached along with a short summary.

In Chapter 5, the second paper that tackles the second and third research question is attached along with a summary.

In Chapter 6, we conclude the thesis by discussing the results obtained along with prospective research based on the two papers that are attached.

## Chapter 2

# Bernevig-Hughes-Zhang model for the quantum spin Hall effect

From the previous chapter, we are familiar that the theoretical proposal to observe quantum spin Hall effect in HgTe/CdTe quantum well [13] was also followed by its experimental confirmation [14, 73, 132]. In another work, quantum spin Hall effect was also theoretically shown to exist in InAs/GaSb quantum well [60]. This quantum well has a double well structure and was also experimentally confirmed to be a quantum spin Hall insulator [70, 77, 120]. The main difference between the two quantum wells, is that in HgTe/CdTe quantum well, the electron and hole subbands appear in the same well whereas in InAs/GaSb quantum well, the subbands appear in different quantum wells. Moreover, the spin-sectors in the Hamiltonian are not (are) coupled in HgTe/CdTe (InAs/GaSb) quantum well. Despite the differences, they both are modeled by using an effective four band model introduced in Ref. [13]. In this chapter, we will look into how the nature of the bands around the Fermi level, give rise to an inverted band structure to host quantum spin Hall phase in both the quantum wells. We also discuss the distinct observations that arise from the differences between the two quantum wells.

## 2.1 Quantum well structure

HgTe, CdTe, InAs and GaSb have zinc-blend structures, which are two fcc lattices interpenetrating each other with a shifted body diagonal. Because each sublattice has a different atom, the inversion symmetry is broken. For all these materials, the relevant bands close to the Fermi energy and also around the  $\Gamma$  point in the Brillouin zone, are an s-type band  $\Gamma_6$  and a p-type band  $\Gamma_8$  with  $J = 3/2$  and  $\Gamma_7$  band with  $J = 1/2$  [13, 60, 133]. The band  $\Gamma_7$  lies far away from the Fermi energy and hence its contribution is ignored while developing the effective theory for the HgTe/CdTe and InAs/GaSb quantum wells.

### 2.1.1 Type-I quantum well

In HgTe/CdTe quantum well, HgTe and CdTe become the well and barrier material respectively (as show in Fig. 2.1). Around the Fermi energy, CdTe has the  $\Gamma_6$  band which is an s-type band and lies above the p-type  $\Gamma_8$  band. On the other hand, in HgTe, the negative energy gap indicates that the  $\Gamma_8$  band lies above the  $\Gamma_6$  band. When the two materials come together in a quantum well, the bands combine to give rise to two effective electron and hole subbands  $E1(H1)$  respectively around the  $\Gamma$  point. The  $E1$  subband is composed of  $|\Gamma_6, m_J = \pm 1/2\rangle$  and  $|\Gamma_8, m_J = \pm 1/2\rangle$ , and the  $H1$  subband is made up of  $|\Gamma_8, m_J = \pm 3/2\rangle$ .  $E1$  ( $H1$ ) subbands behave as conduction (valence) subband around the  $\Gamma$  point and near the Fermi energy [13]. These two subbands appear in the same well material, such heterostructures are also called type-I quantum wells. When the width of the well material  $d$  is less than a critical value  $d_c$ , the  $E1$  subband lies above the  $H1$  subband. It has a normal band progression and is adiabatically connected to a trivial insulator. When the width of the well is above the critical value, the subband  $H1$  lies above  $E1$  subband. This is the inverted band structure which hosts quantum spin Hall phase (see Fig. 2.1). Since the two phases are topologically distinct, there is necessarily a bulk gap-closing, which occurs when the width of the well is equal to the critical width  $d_c$ . This phase transition is possible because the Dirac mass term in the Hamiltonian

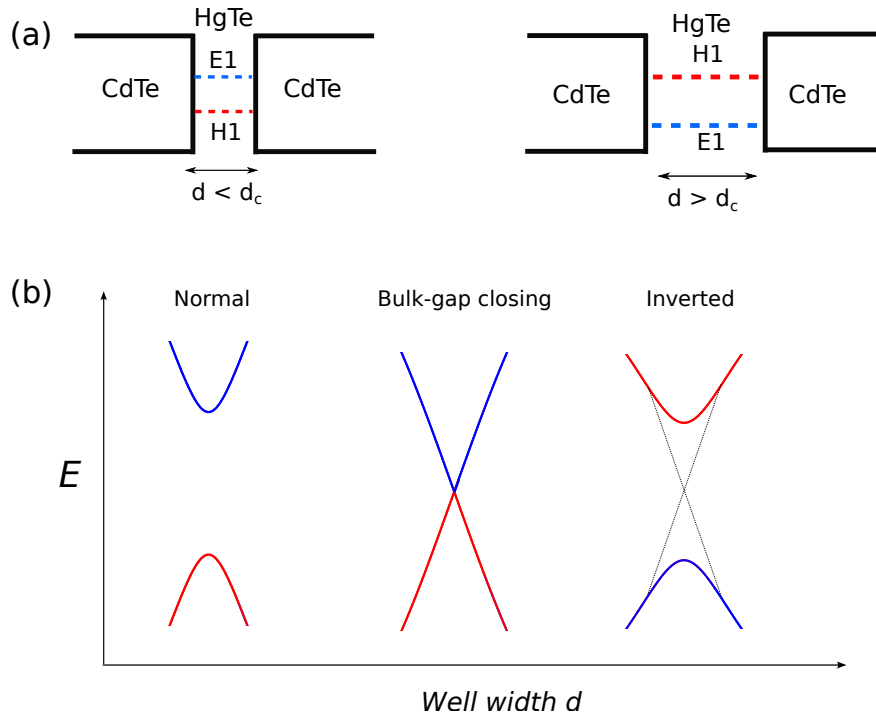


**Figure 2.1:** Schematic illustration of a HgTe/CdTe (a) quantum well and (b) energy band progression around  $\Gamma$  point as a function of well width. The quantum spin Hall phase exists when there is an inverted band structure. In this phase, there will appear helical edge states (dashed lines) in the edge spectrum. Figure adapted from [13].

changes sign after the bulk gap closing. The Dirac mass term is controlled in an experiment through the width of the well [13].

### 2.1.2 Type-II quantum well

This is a double quantum well structure, where there are two well materials, InAs and GaSb while the barrier material is AlSb. Just like in HgTe/CdTe quantum well, the  $E1$  subband becomes the conduction band. This subband is formed in InAs and lies below the valence band  $H1$ , which is formed in GaSb (as shown in Fig. 2.2).

The key difference in the quantum well is the separation of electron and hole like bands in different well materials. These quantum structures are also called type-II quantum wells or electron-hole bilayers. By varying the well width, below (above) a critical value of the width  $d_c$ ,  $E1$  ( $H1$ ) subband lies above (below)  $H1$  ( $E1$ ) subband. This means just like the type-I quantum well, the system has normal or inverted band structure depending on the width of the well. In the inverted regime, the system be-

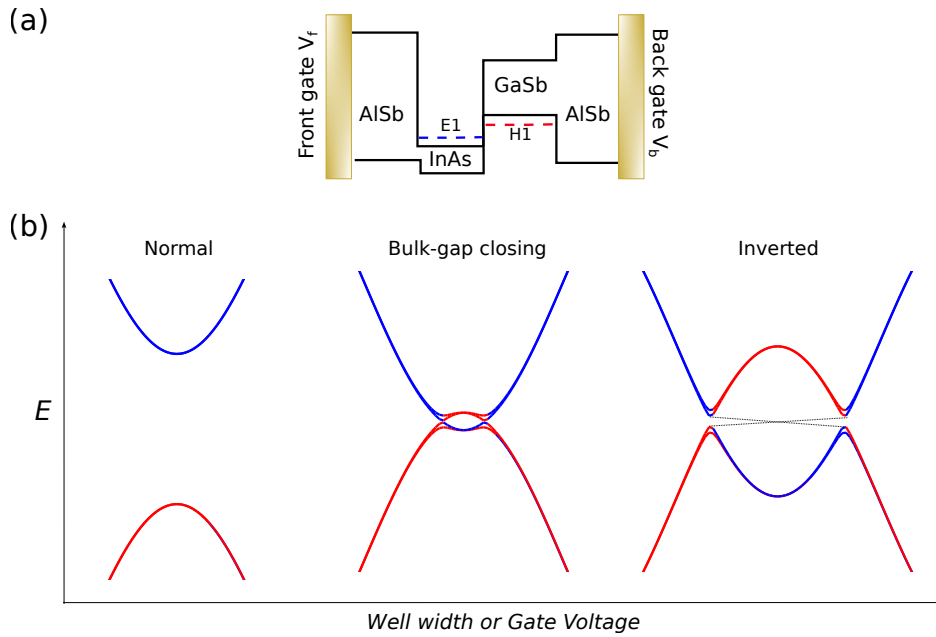


**Figure 2.2:** Schematic illustration of (a) quantum well structure of InAs/GaSb with Al/Sb as barrier material and (b) energy band progression as a function of well width or gate voltages. A front and back gate voltage is applied to continuously tune the quantum well from normal to inverted band structure. In the inverted regime, the system is in quantum spin Hall phase with helical edge states (dashed lines) will appear. Figure adapted from [60].

comes a quantum spin Hall phase (see Fig. 2.2). Because the two subbands are also in different materials, they are weakly coupled compared to type-I quantum well. Hence, it is possible to access them separately through front and back gate voltages [60]. The experimental realization for tuning the bands via gate voltages also exist [134]. Therefore, the Dirac mass term in these quantum wells can change as a function of well-width as well as gate voltages [60, 87, 135]. This is an advantage over the type-I quantum wells, as the bands can be continuously tuned from trivial to topological through gate voltages.

## 2.2 Non-interacting BHZ model

The presence of spin makes the subbands doubly degenerate, and along with time-reversal and inversion symmetry considerations, an effective four band model was proposed in Ref. [13]. The same model could also be used to describe type-II quantum wells [60]. Therefore, the general Hamiltonian for both the quantum wells

becomes:

$$H_0 = \left(E_G - \frac{\hbar^2 k^2}{2m}\right)\tau_z\sigma_0 + Ak_x\tau_x\sigma_z - Ak_y\tau_y\sigma_0 + \Delta_z\tau_y\sigma_y, \quad (2.1)$$

where  $\tau$ 's and  $\sigma$ 's are the Pauli matrices in the electron-hole and spin basis respectively. The parameters in this single-particle Hamiltonian  $E_G$ ,  $\frac{\hbar^2}{2m}$  and  $A$  correspond to  $M$ ,  $B$  and  $A$  parameters of the BHZ model respectively [13]. The terms proportional to  $C$  and  $D$ , and the  $k$  dependent structure inversion asymmetry [136] terms are ignored because they do not contribute qualitatively in understanding the quantum spin Hall phase [60, 85]. The term,  $A$  is the tunnelling parameter that couples electrons and holes,  $E_G$  is the gap between  $E1$  and  $H1$ , it also controls electron-hole density,  $m$  is the effective mass that is assumed equal for both electrons and holes and  $\Delta_z$  is bulk inversion asymmetry term that mixes the two spin sectors.

As has been already discussed before, a quantum spin Hall insulator can be thought of as two copies of quantum anomalous Hall insulator. This means, each spin-sector in the Hamiltonian, if not coupled, becomes a quantum anomalous Hall insulator with a fixed spin. The two spin copies are then related through the time-reversal symmetry. The spin-orbit coupling in each spin-sector acts as a time-reversal symmetry breaking term. This allows us to calculate a Chern number for each spin-sector (shown later). The spin-orbit coupling in the Hamiltonian is given by the tunneling term  $A$ , which describes the hopping from  $s$  to  $p$  orbitals.

## 2.3 Symmetries of the system

### 2.3.1 Inversion symmetry

The bulk inversion symmetry for the Hamiltonian in (2.1) is given by,

$$\tau_z\sigma_0 H_0(-\mathbf{k})\tau_z\sigma_0 = H_0(\mathbf{k}). \quad (2.2)$$

The only term that breaks this symmetry is the  $\Delta_z$  term. In type-I quantum well, the lack of inversion center in the lattice structure, weakly breaks the inversion symmetry. However, in developing the theoretical model, this symmetry can be assumed to

be present if the magnitude of  $\Delta_z$  is considerably small compared to the tunneling term, which is the case in type-I quantum wells. In type-II quantum wells, the lattice structure as well the quantum well structure breaks this symmetry. Therefore, the presence of bulk-inversion asymmetry cannot be as easily ignored.

### 2.3.2 Rotation symmetry

If the quantum well is grown along the z-axis, then the rotation symmetry about this axis by 180 degrees, is a true symmetry of the system. It is given by

$$\tau_z \sigma_z H_0(-\mathbf{k}) \tau_z \sigma_z = H_0(\mathbf{k}). \quad (2.3)$$

Every term in the Hamiltonian  $H_0(\mathbf{k})$  obeys this symmetry and both spin and position space is being rotated simultaneously.

### 2.3.3 Time-reversal symmetry

The time-reversal symmetry for the system is defined as,

$$\tau_0 \sigma_y H_0^T(-\mathbf{k}) \tau_0 \sigma_y = H_0(\mathbf{k}). \quad (2.4)$$

The Hamiltonian (2.1) obeys this symmetry. The time-reversal symmetry in the Hamiltonian establishes a connection between two spin-sectors of the Hamiltonian.

## 2.4 Model parameters

The values of the parameters chosen here are scaled by  $E_0$  and  $d_0$  where  $E_0 = \hbar^2/2md_0^2 = e^2/4\pi\epsilon\epsilon_0 d_0$ .  $E_0$  is the exciton binding energy and  $d_0$  is the exciton Bohr radius. This choice of scaling becomes relevant when Coulomb interactions will be considered in type-II quantum wells in the next chapter.

In reality, the bulk inversion asymmetry term is also present in type-I quantum wells,

Model parameter	HgTe/CdTe	InAs/GaSb
$A/E_0d_0$	1.2	0.06
$B = \hbar^2/2m$	0.5	0.5
$\Delta_z/E_0$	0	0.02

**Table 2.1:** Table of parameter values used for the calculations present in this thesis for HgTe/CdTe and InAs/GaSb. Table adapted from [133].

but the magnitude of the tunneling term  $A$  is so large compared to  $\Delta_z$ , that  $\Delta_z$  can be neglected in the Hamiltonian [13, 62, 133]. For the numerical calculations performed here, the  $\Delta_z$  term in type-I quantum well is zero. In type-II quantum wells, the separation of electron and hole subbands in different materials, reduces the magnitude of the tunneling term  $A$ . In this case, both  $\Delta_z$  and  $A$  have comparable magnitudes.

In this thesis, we will only consider the momentum-independent bulk inversion asymmetry  $\Delta_z$  term. This assumption greatly simplifies our calculations without affecting the closing of the bulk gap at finite  $k$  for these bilayer systems [85, 125, 137].

## 2.5 Effect of bulk inversion asymmetry $\Delta_z$ term

In the following subsections, we will look at the energy spectrums of type-I and type-II quantum wells, to study the topological phase transition. We will use the model parameter values in Table. (2.1). We will study the properties of the quantum wells as a function of  $E_G/E_0$ , which is the Dirac mass term and can be tuned in experiments. The other parameters are constant and take the values given in Table 2.1. To calculate the edge spectrum, a ribbon of finite width along the  $y$  direction and infinite along the  $x$  direction is considered.

### 2.5.1 Type-I quantum well

In the calculations presented here, when  $E_G/E_0 < 0$  ( $E_G/E_0 > 0$ ), the system has a normal (inverted) band progression, the electron (hole) subband is above the hole

(electron) subband (see Fig. 2.1). At  $E_G = 0$ , the bulk-gap closes at  $\Gamma$  point (see Fig. 2.1). In the inverted (normal) phase, the system becomes a quantum spin Hall (trivial) insulator with a non-zero bulk gap at  $\Gamma$  point. In the quantum spin Hall phase, there appears edge states with spin-momentum locking, which intersect at the  $\Gamma$  point. However, in the trivial phase, there are no edge states. This is seen in the edge spectrum presented in Fig. 2.3. At  $E_G = 0$ , the bulk-gap closes.

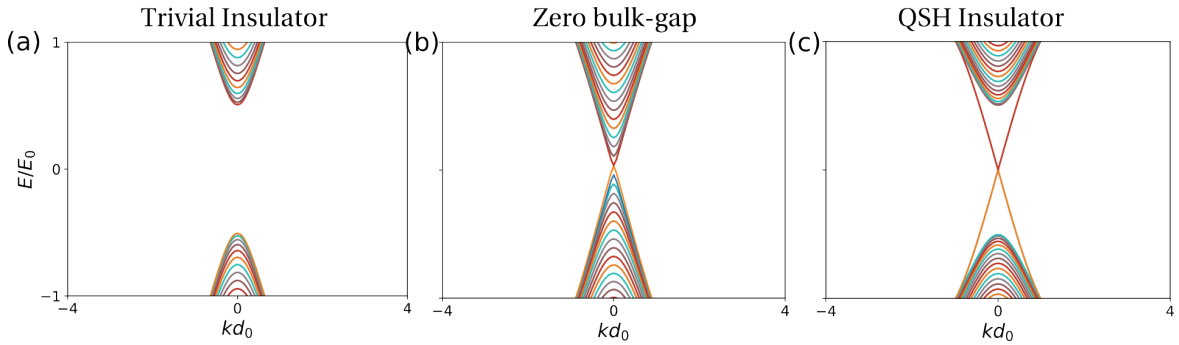


**Figure 2.3:** Topological phase transition in type-I quantum well when  $\Delta_z = 0$  as seen through the edge spectrum. In the quantum spin Hall phase, the helical edge states cross at  $\Gamma$  in the Brillouin zone.

As discussed before type-I quantum wells also have bulk inversion asymmetry, but because the tunneling term is so strong, the role of  $\Delta_z$  term could be neglected [13, 14, 138]. We check this statement by considering  $\Delta_z = 0.04E_0$  in (2.1):

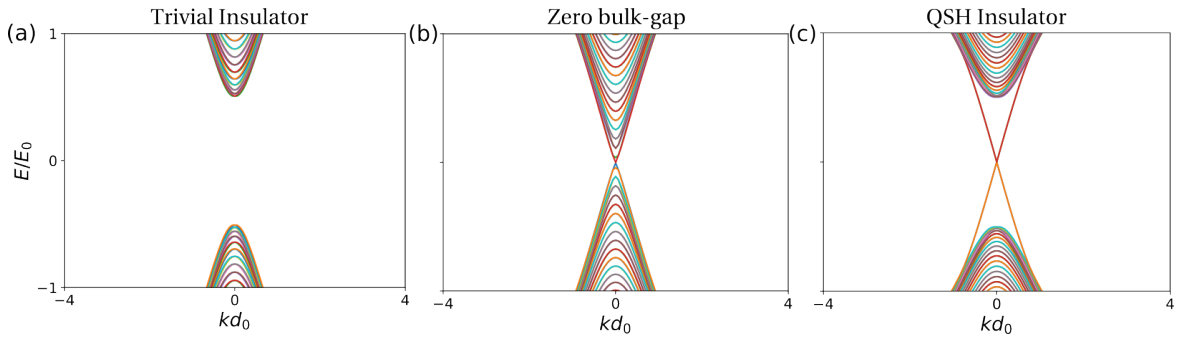


**Figure 2.4:** Topological phase transition in type-I quantum well when  $\Delta_z \neq 0$  as seen through the edge spectrum. We notice that due to the large tunneling term  $A$ , the  $\Delta_z$  term does not affect the phase transition. In the quantum spin Hall phase, the helical edge states cross at  $\Gamma$  in the Brillouin zone.

### 2.5.2 Type-II quantum well

The bulk-inversion asymmetry is naturally present in type-II quantum wells because of the lattice and quantum well structure. Moreover, the tunneling term is also small in type-II quantum wells. Hence the bulk-inversion asymmetry term cannot be neglected like before. The  $k$  independent bulk inversion asymmetry term  $\Delta_z$ , couples the spin sectors but does not break the time-reversal symmetry, since the coupling is not between the Kramer partners. Therefore, it will not destroy the edge states in quantum spin Hall phase, unless it is sufficiently large and closes the bulk-gap [62]. For  $E_G > 0 (< 0)$ , this case exhibits the inverted (normal) regime (see Fig. 2.2). The important difference is that the bulk gap closes at a finite value of  $E_G/E_0 = \frac{\Delta_z^2 d_0^2}{2A^2}$  and at a finite value of the wave vector  $k_{cross}$  [60, 77]. In the edge spectrum in Fig. 2.5, we see that in the quantum spin Hall (trivial) phase, there are (no) helical edge states that cross at  $\Gamma$  point.

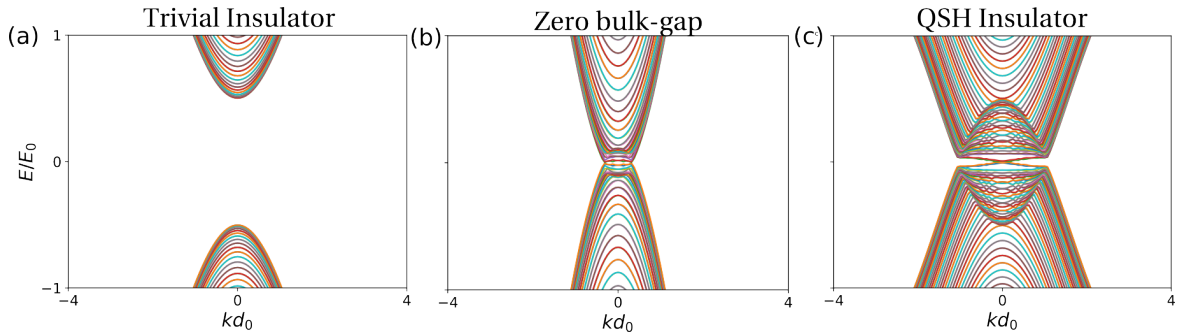


**Figure 2.5:** Topological phase transition for type-II quantum wells when  $\Delta_z = 0.02$  as seen through the edge spectrum. The bulk-gap closes for a finite value of  $kd_0$  and *not* at the *Gamma* point in the Brillouin zone.

## 2.6 Effect of mass asymmetry

In reality, there is always a mass asymmetry between electrons and holes, that is  $m_e \neq m_h$ , the Hamiltonian can be written as:

$$H_0 = \left( \frac{\hbar^2 k^2}{2m_e} - E_{G_e} \right) \frac{1}{2} (\tau_0 + \tau_z) \sigma_0 + \left( E_{G_h} - \frac{\hbar^2 k^2}{2m_h} \right) \frac{1}{2} (\tau_0 - \tau_z) \sigma_0 + \quad (2.5)$$

$$Ak_x \tau_x \sigma_z - Ak_y \tau_y \sigma_0 + \Delta_z \tau_y \sigma_y, \quad (2.6)$$

where  $E_{G_e} = \frac{2m_{\text{eff}}}{m_e} E_G$  and  $E_{G_h} = \frac{2m_{\text{eff}}}{m_h} E_G$  with  $1/m_{\text{eff}} = 1/m_e + 1/m_h$ . The exciton binding energy and radius now becomes,

$$E_0 = \frac{\hbar^2}{2m_{\text{eff}}d_0^2} = \frac{1}{4\pi\epsilon\epsilon_0} \frac{e^2}{d_0}. \quad (2.7)$$

When  $m_e = m_h = m$  and  $m_{\text{eff}} = m/2$ , and we recover the equations we considered in the Hamiltonian (2.1). We check the effect of mass asymmetry on the topological transition when  $m_e/m_h = 0.84$ . There is only a small effect due to the mass asymmetry in the dispersion of the electron and hole bands. We calculate the edge spectrum for type-I and type-II and see that the topological transition is not affected by the change in effective masses of electrons and holes (see Fig. 2.6).

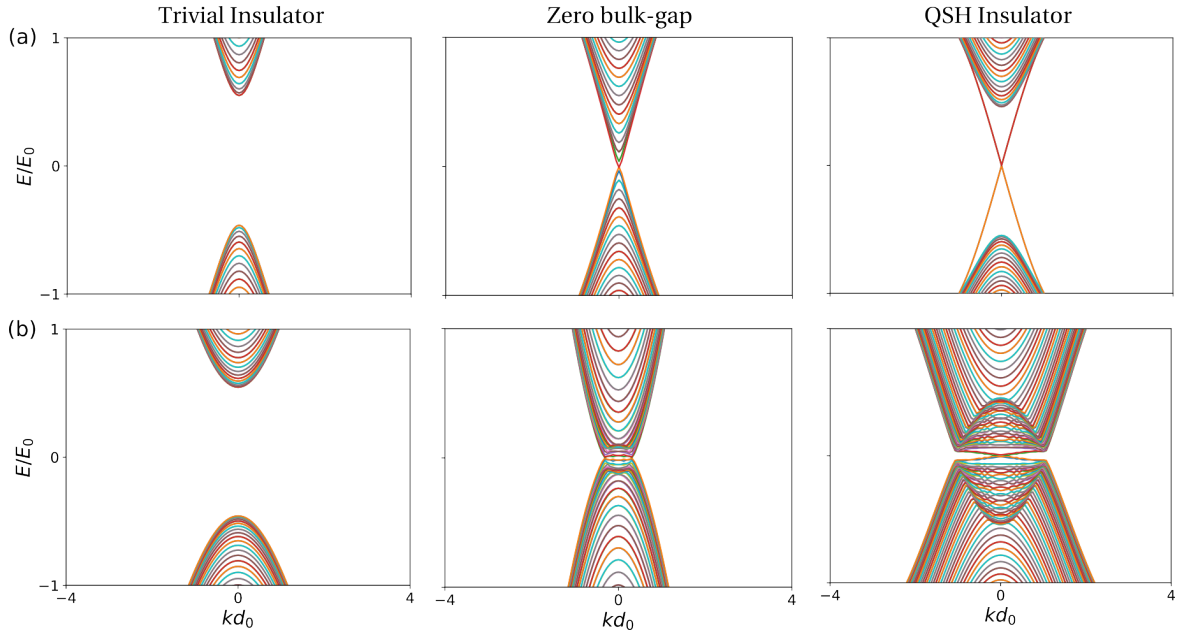


**Figure 2.6:** Topological phase transition with  $m_e/m_h = 0.84$  for (a) Type-I quantum well when  $\Delta_z = 0$  and (b) type-II quantum well when  $\Delta_z = 0.02$ . The gap closes at  $\Gamma$  if  $\Delta_z = 0$  and at  $E_G/E_0 = \frac{\Delta_z^2 d_0^2}{2A^2}$  and non-zero  $kd_0$  if  $\Delta_z \neq 0$ . The mass asymmetry has no effect on the topological phase transition.

## 2.7 Topological Invariant

In the previous chapter, we discussed that a topological phase is identified by calculating a topological invariant [69]. Below we look into the choice of topological

invariant when the spin sectors are (are not) coupled in the the Hamiltonian in (2.1).

### 2.7.1 Spin Chern topological invariant when $\Delta_z = 0$

The effective four band model for type-I quantum well, the rotation symmetry along the growth axis, inversion symmetry and time-reversal symmetry are preserved, which means that there is no coupling between the two spin sectors. Since the spin-sectors are independent of each other, the perpendicular component of the spin  $S_z$  along the growth axis  $z$  is a conserved quantity. This means, for each  $2 \times 2$  spin sector of the Hamiltonian, the Chern number can be calculated like it is calculated for the quantum anomalous Hall phase. This is possible because the spin-orbit coupling in each spin-block, which is the term proportional to  $A$ , acts as a time-reversal symmetry breaking term.

The Chern number is an integer and is equal to the Hall conductance of the filled bands. It is calculated when the system is gapped. Since the two spin-sectors are related by time-reversal symmetry, the Hall conductance of each spin-sector will be related through  $\sigma_{xy}(H(k)) = -\sigma_{xy}(H^*(-k))$ , where  $H(k)$  ( $H^*(-k)$ ) are the spin-up (down) sectors [13]. The Hall conductance can be obtained from calculating the Berry connection and integrating over the full Brillouin zone. Each spin-sector is a two-level Hamiltonian, which can be written as  $H(\mathbf{k}) = \mathbf{d}_i \cdot \sigma_i$ . Here  $\sigma_i$  and  $d_i$  are the Pauli matrices and components of the Hamiltonian respectively. The eigenvalues of this Hamiltonian will be  $\pm d$  where  $d = \sqrt{d_1^2 + d_2^2 + d_3^2}$  and the eigenvectors will be:

$$\psi_- = \frac{1}{\sqrt{2d(d+d_3)}} \begin{pmatrix} -d_1 + id_2 \\ d + d_3 \end{pmatrix}, \quad \psi_+ = \frac{1}{\sqrt{2d(d+d_3)}} \begin{pmatrix} d + d_3 \\ d_1 + id_2 \end{pmatrix} \quad (2.8)$$

Since, the Chern number is calculated from the filled bands, the Berry potential  $A_i$  and Berry connection  $\Omega_{xy}$  will be:

$$\begin{aligned} \mathcal{A}_i &= i \langle \psi_- | \partial_{k_i} | \psi_- \rangle = \frac{-1}{2d(d+d_3)} [d_2 \partial_i d_1 - d_1 \partial_i d_2], \quad k_i := k_x, k_y \\ \Omega_{xy} &= \frac{\partial \mathcal{A}_y}{\partial k_x} - \frac{\partial \mathcal{A}_x}{\partial k_y} \end{aligned} \quad (2.9)$$

The Hall conductance for each spin-sector can be obtained using:

$$\sigma_{xy} = \frac{e^2}{h} \frac{1}{2\pi} \int \int dk_x dk_y \Omega_{xy} \quad (2.10)$$

For the spin  $\uparrow$  sector of the Hamiltonian  $H_0$ , the components are  $d_1 = Ak_x$ ,  $d_2 = Ak_y$  and  $d_3 = E_G - B(k_x^2 + k_y^2)$ . The Berry potential and the curvature becomes:

$$\begin{aligned} \mathcal{A}_x &= \frac{-A^2 k_y}{2\sqrt{A^2 k^2 + (E_G - Bk^2)^2} \left( \sqrt{A^2 k^2 + (E_G - Bk^2)^2} + (E_G - Bk^2) \right)}, \\ \mathcal{A}_y &= \frac{A^2 k_x}{2\sqrt{A^2 k^2 + (E_G - Bk^2)^2} \left( \sqrt{A^2 k^2 + (E_G - Bk^2)^2} + (E_G - Bk^2) \right)} \end{aligned} \quad (2.11)$$

$$\Omega_{xy} = \frac{A^2(Bk^2 + E_G)}{2(A^2 k^2 + (E_G - Bk^2)^2)^{3/2}} \quad (2.12)$$

Substituting (2.12) in (2.10), we get,

$$\sigma_{xy} = \frac{e^2}{h} \frac{1}{2\pi} \int \int dk_x dk_y \frac{A^2(Bk^2 + E_G)}{2(A^2 k^2 + (E_G - Bk^2)^2)^{3/2}} \quad (2.13)$$

After performing the integration from  $-\infty$  to  $\infty$ , for negative valued  $E_G$ , the Chern number and the Hall conductance becomes zero. For positive values of  $E_G$  and spin-up sector, we obtain  $\sigma_{xy}(\uparrow) = 1e^2/h$  with Chern number  $n_\uparrow = 1$ . From the time-reversal symmetry, we get for the spin-down sector,  $\sigma_{xy}(\downarrow) = -1e^2/h$  and Chern number  $n_\downarrow = -1$ . The spin Chern invariant is give by  $n_\uparrow - n_\downarrow = 2$ , which gives the spin Hall conductance as  $\sigma_{xy}^s = 2e^2/h$  (see Fig. 2.7). The sum of the two Chern numbers is related to the charge Hall conductance and is  $n_\uparrow + n_\downarrow = 0$ . At  $E_G = 0$ , the bulk-gap closes and divides the phase diagram into trivial (quantum spin Hall) phase for  $E_G < 0$  ( $E_G > 0$ ).

We can also observe the bulk-gap closing from the lattice Hamiltonian. This can be obtained by replacing  $k_i \rightarrow \sin k_i$ ,  $k_i^2/2 \rightarrow (1 - \cos k_i)$  in the continuum Hamiltonian,

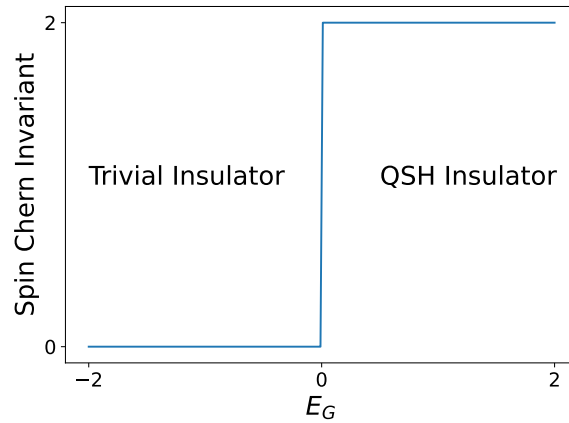


**Figure 2.7:** Spin Chern invariant calculated as a function of  $E_G$ . In trivial (quantum spin Hall) phase, the value of the invariant is zero (two). The value of edge conductance is equal to the spin Chern invariant in units of  $e^2/h$ .

where  $k_i := k_x, k_y$ . The lattice Hamiltonian becomes [13],

$$\begin{aligned} d_1 + id_2 &= A(\sin k_x + i \sin k_y) \\ d_3 &= -2B(2 - E_G/2B - \cos k_x - \cos k_y) \end{aligned} \quad (2.14)$$

The energy gap for this model is

$$E_{\text{gap}} = 2\sqrt{A^2(\sin^2 k_x + \sin^2 k_y) + 4B^2(2 - E_G/2B - \cos k_x - \cos k_y)^2} \quad (2.15)$$

which gives zero energy gap at  $(k_x, k_y) = (0, 0), (0, \pi), (\pi, 0), (\pi, \pi)$  for values of  $E_G/2B = 0, 2$  (for both  $(0, \pi)$  and  $(\pi, 0)$ ) and 4 respectively, which are the transition points in the Brillouin zone.

In this chapter we are studying the topological transition that occurs as a result of bulk-gap closing at  $\Gamma$  point (or close to this point for  $\Delta_z \neq 0$ ). Hence, the spin Chern invariant in the range  $E_G < 0$  (trivial) and  $0 < E_G/2B < 2$  (quantum spin Hall) in the lattice Hamiltonian will be relevant [13].

### 2.7.2 $Z_2$ topological invariant when $\Delta_z \neq 0$

When  $\Delta_z \neq 0$ , the spin-rotation symmetry breaks as  $\Delta_z$  couples the two spin sectors.  $S_z$  is no longer a conserved quantity, and the spin Hall conductance is no longer

quantized. As the time-reversal symmetry is still preserved, there will appear helical edge states as long as the bulk-gap is not closing.

The distinction between the different topological phases appears in the number of pairs of edge states that appear and in the way they behave in the energy gap in the two phases. In the trivial phase, the edge states typically do not cross the energy gap, and they always appear in an even number of pairs at each energy. This allows for elastic backscattering and localization of edge states. In the quantum spin Hall phase, the edge states appear in odd number of pairs and cross the energy gap. Since the time-reversal symmetry is preserved, these states are robust against weak perturbations, and therefore single-particle elastic backscattering is forbidden.

A quantized spin Hall conductance is not always a marker of the quantum spin Hall effect. This is argued by considering a cylinder with circumference  $L$  and by adiabatic introduction of a magnetic flux through the cylinder. A weak electric field appears along the circumference. When the rate of spin accumulation is calculated by utilizing a similar argument as in the Laughlin pump [139], the trivial phase has zero spin accumulation as the edge states are localized, whereas the quantum spin Hall system has a non-zero spin accumulation due to the particle-hole pair (whose spins do not compensate each other) that appears at the Fermi energy, which contributes to the spin Hall conductance. The spin accumulation is a robust property of quantum spin Hall effect, even though the spin Hall conductance is not quantized unless the particle and hole carry opposite spins [64]. Kane and Mele emphasize that the *quantum* does not refer to *quantized* in the context of quantum spin Hall insulators [64].

Since, the spin-sectors cannot be treated independently as was done in the case before, a new topological invariant that captures the distinct phases is required. The time-reversal symmetry operator  $\mathcal{T}$ , divides the Hamiltonian  $H_0$  and the occupied energy bands  $|\psi(\mathbf{k})\rangle$  into two subspaces. In the even subspace, the occupied bands,  $|\psi_1\rangle$  and  $|\psi_2\rangle$ , span the same space as  $\mathcal{T}\psi_1$  and  $\mathcal{T}\psi_2$ . Hence, the transformation matrix between the pairs of states is unitary. In the odd subspace, the  $\mathcal{T}|\psi_1\rangle$  and  $\mathcal{T}|\psi_2\rangle$  span the space of the unoccupied bands  $|\psi_3\rangle$  and  $|\psi_4\rangle$ . The transformation matrix

between  $|\psi_1\rangle$  and  $|\psi_2\rangle$  and  $\mathcal{T}|\psi_1\rangle$  and  $\mathcal{T}|\psi_2\rangle$  is now not unitary and can be zero. The aim is to find the region in  $\mathbf{k}$ , where the odd subspace occurs. This can be done by considering the overlap between  $|\psi_i\rangle$  and  $\mathcal{T}|\psi_j\rangle$ . We get a single complex number that give this information through the Pfaffian:

$$P(\mathbf{k}) = \text{Pf}[\langle\psi_i(\mathbf{k})|\mathcal{T}|\psi_j(\mathbf{k})\rangle] \quad (2.16)$$

If the occupied bands belongs to the even subspace,  $|P(\mathbf{k})| = 1$  and if it belongs to the odd subspace, then  $P(\mathbf{k}) = 0$ . There will always be a pair of zeros that occur at  $\pm\mathbf{k}^*$  points in the Brillouin zone because of time-reversal symmetry. They will not occur at time-reversal invariant momenta or TRIM points because  $P(\mathbf{k}) = 1$  necessarily at these points. The  $Z_2$  topological invariant is calculated by counting the number of zeros when the system is gapped, as the Pfaffian is undefined for zero bulk gap. In the trivial (topological) phase, there are even (odd) number of pair of zeros. As the Hamiltonian  $H_0$  has an additional two-fold rotational symmetry, there are lines instead of points, where the zeros occur, the zeros will lie on a curve enclosing the time-reversal invariant point, which in this case is  $\Gamma$  (see Fig. 2.8).

The  $Z_2$  topological invariant  $\nu$  is also related to the number of edge states through the formula:

$$\nu = N(E) \pmod{2}, \quad N(E) = N_+ + N_-, \quad (2.17)$$

where  $N_+$  and  $N_-$  are the edge states moving in opposite directions to each other. Since, the number of helical edge states in the trivial and quantum spin Hall phase will differ by an odd number. The topological invariant  $\nu$  is always 0 or 1, which counts the modulo 2 of the number of helical pairs that appear on the edge of the material. In the quantum spin Hall (trivial) phase, there always appear only odd (even) number helical edge states.

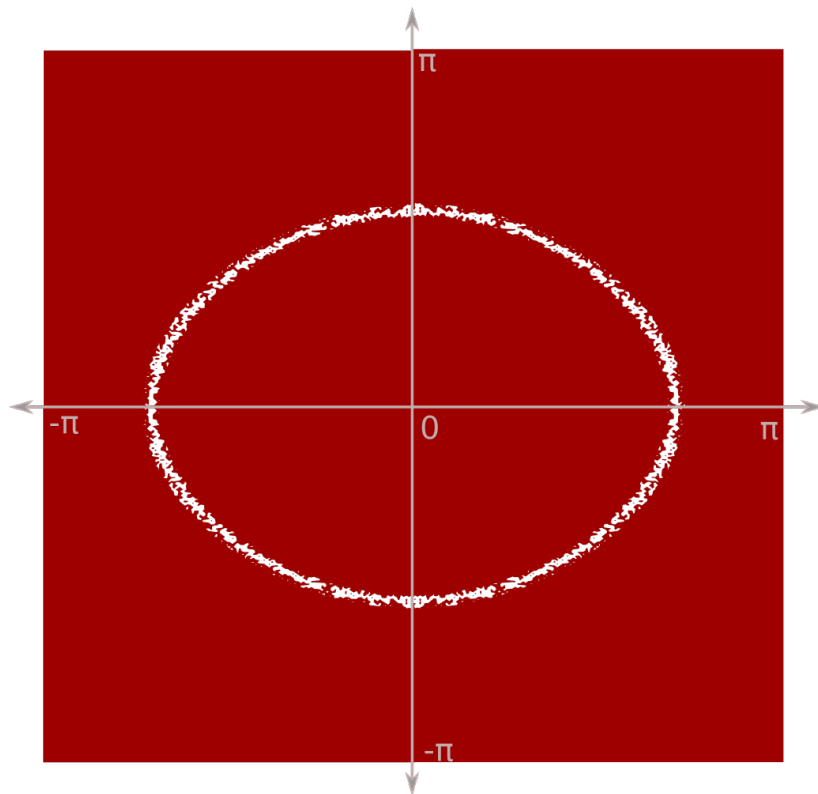


**Figure 2.8:** The zeros of  $P(k)$  lying on a curve enclosing the  $\Gamma$  point, when the system is in quantum spin Hall phase.

## 2.8 Effect of magnetic field

Even though qualitatively, type-I and type-II quantum wells behave similarly when there is no magnetic field. The two systems respond differently to an externally applied magnetic field. Below we discuss the effect of magnetic field, and also consider the role of disorder when considered additionally.

### 2.8.1 Perpendicular magnetic field

**Type-I quantum well:** A type-I quantum well in its inverted regime supports helical edge states, which are counter propagating pseudo spin states that appear along the edges of a two-dimensional sample (or the *helical edge states*). When a magnetic field is applied, the time-reversal symmetry breaks, and a gap opens in the helical edge states. For small values of the magnetic field, there is a small edge gap and the edge transport can still be observed. Increasing the magnetic field can close the bulk-gap and give a non-zero Chern number. In other words, for a critical value of a magnetic field, the bulk-gap closes and the quantum spin Hall gives way to a quantum Hall phase [140–143]. If the Landau level spectrum is observed, there is only one Landau level from the electron and hole band each, that appear inside the bulk-gap. The value of the bulk gap is measured when there is no magnetic field applied. This is because the value of the gap is maximum when there is zero magnetic field for the inverted band structure. In the inverted regime, as the magnetic field is increased, the gap decreases [144, 145]. In this case, there appears crossing of the Landau levels from the  $E1$  and  $H1$  subband at a critical value of the magnetic field  $B_c$  [146]. The main contribution of the perpendicular magnetic field in this material is the orbital effect. The energy gap opening due to the Zeeman effect is less than a 1 meV [138].

*Role of disorder:* In normal band progression, increasing disorder decreases the band gap [147]. However, in inverted band structure, the band gap increases with increasing disorder. This means, in the presence of strong disorder, it requires a large magnetic field to close the band gap and the system to go from quantum spin Hall to

quantum Hall state. In other words, the helical edge states remain robust for a large value of disorder strength.

**Type-II quantum well:** The type-II quantum well also is a quantum spin Hall insulator. In its inverted regime, when the magnetic field is increased, the gap between the electron and hole subbands decrease and cross each other at a critical magnetic field  $B_c$ . But, unlike the type-I quantum well, it does not become a quantum Hall insulator after this critical field. Due to the weak coupling between the electron and hole subbands, compared to the type-I quantum well, there are two more Landau levels that appear inside the bulk gap [146]. This leads to two separate crossing of the Landau levels at  $B'_c$  and  $B_c$ . From  $B'_c$  to  $B_c$ , there exists a quasi-metallic state, where there is bulk conduction [146]. At  $B_c$ , the system becomes a quantum Hall insulator with chiral edge states and insulating bulk. When the Zeeman effect is considered, there again exists a bulk-conducting region [146]. In the presence of electron-electron interactions, it has been observed that the Landau levels do not cross because of exciton condensation [148].

*Role of disorder:* In the case of type-II quantum wells, it is observed that as disorder increases, the critical value of magnetic field  $B'_c$  for which bulk conduction appears becomes smaller. This widens the  $B'_c \lesssim B \lesssim B_c$  region, thereby reducing the robustness of helical edge states. This behaviour is very different when compared to type-I quantum well, when disorder is introduced [146].

## 2.8.2 In-plane magnetic field

**Type-I quantum well:** The in-plane magnetic field in type-I quantum wells such as HgTe/CdTe only contribute to a Zeeman splitting and there is no observation of orbital effect.

*Zeeman Effect:* The Zeeman splitting leads to the opening of a small gap in energy of the order less than 1 meV.

**Type-II quantum well:** Preserving time-reversal symmetry is crucial for the protection of helical edge states in quantum spin Hall insulators. In InAs/GaSb, an in-plane magnetic field of 10T or more is shown to not destroy these edge states [70, 72].

Though the behaviour of these bilayers in the presence of perpendicular magnetic field is still somewhat understood, the persistence of edge states in the presence of large values of in-plane magnetic field is not. In Ref. [149], it is shown that, the spatial separation of electron and hole bands allows a non-zero magnetic flux between the two layer. This results in an orbital effect in InAs/GaSb which dominate the Zeeman splitting.

*Orbital Effect:* In the bulk spectrum, the main effect of the orbital effect is to shift the electron and hole bands by some amplitude,  $\pm k_M$ , in k-space respectively. The shift in the momentum  $k_M$  is directly proportional to the magnitude of the applied in-plane magnetic field. This results into a transition to a gapless indirect semimetal phase at a critical value of the magnetic field. Therefore, already at quite small magnetic field there is no bulk gap protecting the edge states.

Moreover, the top (bottom) of the hole (electron) band shifts upwards (downwards). This results in a lopsided looking edge spectrum, where a direct gap in absence of magnetic field becomes an indirect gap as the magnetic field is increased. At some critical value of the magnetic field, the electron and hole band overlap. Even so, there is no bulk-gap that is protecting these "edge" states. The consideration of interaction effects may explain this behaviour.

*Zeeman Effect:* Zeeman field breaks the time-reversal symmetry and opens a gap in the edge state spectrum. However, this effect is much weaker than the orbital effect which leads to bulk gap closing.

*Role of disorder:* If an on-site impurity potential is added in the presence of in-plane magnetic field, the quantized edge conductance is only weakly destroyed and localized states with relatively long localization length may appear [146, 149].

In this chapter, we looked into the main differences between a type-I and type-II quantum wells. The lower value of the tunneling term  $A$  and the bulk-inversion asymmetry term  $\Delta_z$  in type-II quantum wells, play an important role when Coulomb interactions are included. This will be studied in the next chapter.

# Chapter 3

## Interplay of excitons and the quantum spin Hall effect

In this chapter, we discuss why including Coulomb interactions in type-II quantum wells, lead to the formation of excitons in these systems. We study the effect of excitons on the topological phase transition. This forms the preliminary study of this system for the original work presented in next chapter.

### 3.1 Excitons in Type-II quantum well

An electron from a conduction band and a hole from a valence band form a bound state called exciton. The excitons can become a condensate under certain conditions [150, 151]. The Coulomb interactions between the electrons and holes is the main reason behind the formation of this bound state. In addition to optically generated excitons, it has been found that excitons are also created from spatially separated electron and hole layers [152–155] with experimental observations in bilayers [128–131]. The magnitude of the lifetime of excitons which are generated from a bilayer configuration is greater than the excitons created from optical excitations [152]. One of the requirements to obtain an exciton condensate phase in such systems is to have zero to very weak tunneling processes between the electron and hole layers. Therefore, the bilayer configuration in InAs/GaSb quantum wells, where the weakly

coupled electron and hole subbands are separated in different materials becomes a good setup to realize excitons [87, 151]. There have been several experimental signatures of the presence of exciton condensate phases in these double quantum well structures [88]. Contrary to type-II quantum wells, it is difficult to obtain an exciton condensate phase in type-I quantum well structures, as the electron and hole subband are strongly coupled [85, 133].

As has been discussed before, it has been observed in experiments that the conductance is quantized for very large values of magnetic field for short samples [70]. In long samples and in the absence of magnetic field, the longitudinal resistance increases linearly with the length of the device [85]. Moreover, the mean free path is found to be temperature independent for a temperature range of 20 mK to 4.2K [70–72]. Interactions and disorder have been considered as possible explanations for the above experimental observations. The temperature independent mean-free path suggest the presence of elastic backscattering effects. These backscattering effects could be a result of a spontaneously or dynamically broken time-reversal symmetry. The order of the observed mean free path suggests that dynamically broken time-reversal symmetry may be unlikely [85].

In Ref. [85], which becomes the motivation behind the publications comprising this thesis, the authors study the presence of Coulomb interactions in type-II quantum well, which is referred to as an electron-hole bilayer in the paper, by performing a mean-field analysis of the total Hamiltonian. The numerical Hartree-Fock mean-field calculations in the presence of the Coulomb interactions lead to a simplified mean-field potential which captures the spin structure of the excitons in the bilayer:

$$\begin{aligned} \Delta^{mf}(\mathbf{k}) = & \Re[\Delta_1]\tau_y\sigma_y + \Re[\Delta_2](k_x\tau_x\sigma_z - k_y\tau_y\sigma_0) \\ & + \Im[\Delta_1]\tau_x\sigma_y - \Im[\Delta_2](k_x\tau_y\sigma_z + k_y\tau_x\sigma_0), \end{aligned} \quad (3.1)$$

where  $\tau$ 's and  $\sigma$ 's are the Pauli matrices that stand for electron-hole and spin degrees of freedom, and  $\Delta_1$  and  $\Delta_2$  are complex valued, bosonic fields designated for s-wave and p-wave pairing between the excitons. The real and imaginary parts of these pairings have been written separately in (3.1) because the imaginary parts become order

parameters for TRS breaking, as shown subsequently. The simplified mean field term (3.1) acts as the interaction term  $H_{\text{EC}}$  which is added to the single particle Hamiltonian  $H_0$  (2.1), introduced in the previous chapter. As can be seen from (3.1), only interaction between the electron and hole bands are considered. Coulomb interactions within each band are neglected as they only result in renormalisation of the energy bands [85]. As was done in the previous chapter, the k-dependant spin-orbit couplings that arise from bulk and structural inversion asymmetry terms will also not be considered in the main calculations.

In the calculations present henceforth, we will see the effect of excitons that appear as a result of Coulomb interactions between the electron and hole band. As was done in the previous chapter, the natural units for all parameters used in the calculations will be  $E_0$  and  $d_0$ , which are the exciton binding energy and the Bohr radius, respectively. The values of these units are determined by equating the Bohr formula for the hydrogen atom with the Coulomb energy [85]:

$$E_0 = \frac{\hbar^2}{2m_{\text{eff}}d_0^2} = \frac{1}{4\pi\epsilon\epsilon_0} \frac{e^2}{d_0} \quad (3.2)$$

### 3.1.1 Obtaining the exciton pairings

The simplified expression for the mean-field potential, (3.1) is used in the Hartree-Fock mean field equations. This gives the following expressions to obtain the values of  $\Delta_1$  and  $\Delta_2$  [125]:

$$\begin{aligned} \Delta_1 &= \frac{g_s d_0^2}{(2\pi)^2} \int d^2k \left[ \langle c_{\mathbf{k}\downarrow 2}^\dagger c_{\mathbf{k}\uparrow 1} \rangle - \langle c_{\mathbf{k}\uparrow 2}^\dagger c_{\mathbf{k}\downarrow 1} \rangle \right] \\ \Delta_2 &= \frac{g_p d_0^4}{(2\pi)^2} \int \left[ - \langle c_{\mathbf{k}\uparrow 2}^\dagger c_{\mathbf{k}\uparrow 1} \rangle (k_x - ik_y) + \langle c_{\mathbf{k}\downarrow 2}^\dagger c_{\mathbf{k}\downarrow 1} \rangle (k_x + ik_y) \right] \end{aligned} \quad (3.3)$$

where  $g_s$  and  $g_p$  are the s-wave and p-wave pairing strengths of excitons. The electron annihilation operators are  $c_{k\sigma 2}$  and  $c_{k\sigma 1}$  for the electron and hole bands respectively. Choosing the best values of the interaction strengths  $g_s$  and  $g_p$  between excitons allows one to get approximately the same results from Hartree-Fock calculations in Ref [85].

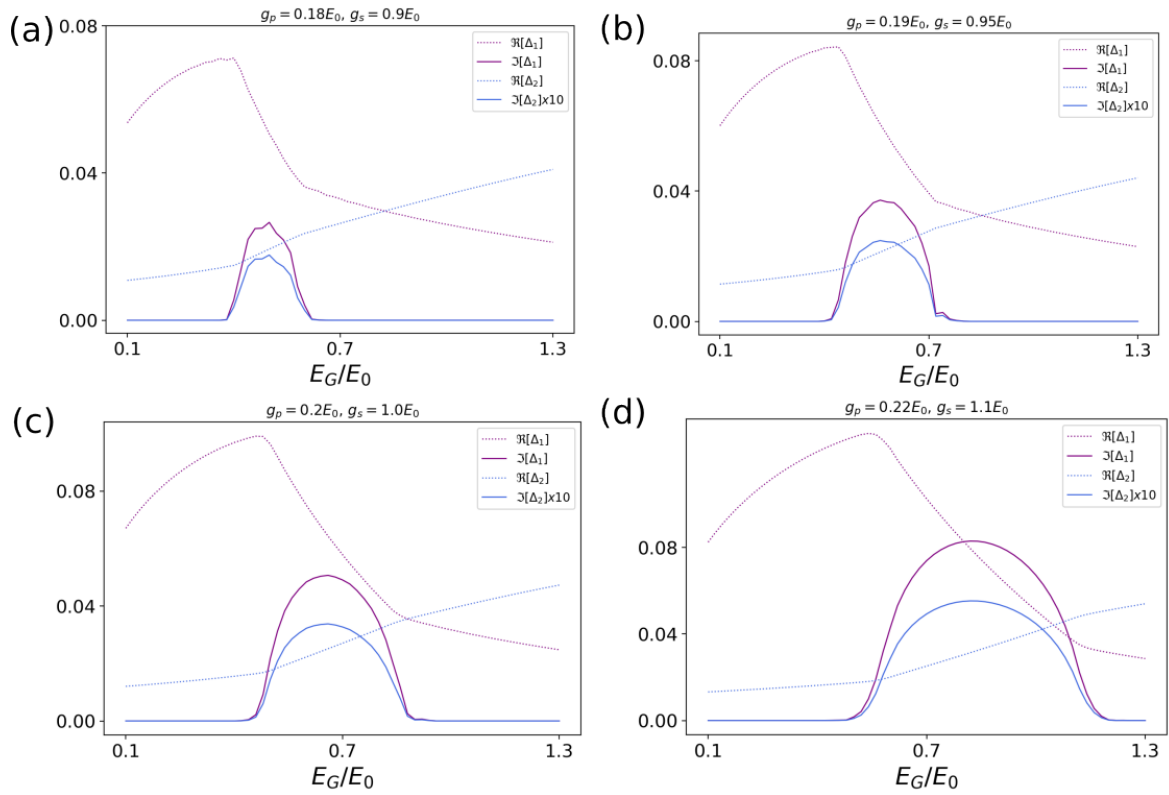


**Figure 3.1:** Phase diagram as a function of  $E_G$  for different fitting parameters. (a)  $g_p = 0.18E_0, g_s = 0.9E_0$ , (b)  $g_p = 0.19E_0, g_s = 0.95E_0$ , (c)  $g_p = 0.2E_0, g_s = 1.0E_0$  and (d)  $g_p = 0.22E_0, g_s = 1.1E_0$ .

For the choice of  $g_s = 1.0E_0$  and  $g_p = 0.2E_0$ , the time-reversal symmetry breaking order parameters become non-zero for approximately the same range as the Hartree-Fock calculations performed in Ref. [85]. From the phase diagram presented as a function  $E_G/E_0$  for  $g_s = 1.0E_0$  and  $g_p = 0.2E_0$ , we can see that for small values  $E_G$ ,  $\Re[\Delta_1] > \Re[\Delta_2]$  and for large values of  $E_G$ ,  $\Re[\Delta_1] < \Re[\Delta_2]$  while  $\Im[\Delta_1, \Delta_2] = 0$  for both cases. Only for intermediate values of  $E_G$  are the  $\Im[\Delta_1, \Delta_2]$  taking non-zero values (see Fig. 3.1c). In the following sections, all calculations have been performed with the above of choice of fitting parameters.

## 3.2 Topological Phase transition

The time-reversal symmetry operator is defined as  $\mathcal{T} = i\tau_0\sigma_y\mathcal{K}$  where  $\mathcal{K}$  is the complex conjugation operator. Let the total Hamiltonian be defined as  $H = H_0 + H_{\text{EC}}$ , the time reversal symmetry operator  $\mathcal{T}$  commutes with  $H$ , if the imaginary terms  $\Im[\Delta_1, \Delta_2] = 0$ . This suggests that the imaginary parts of excitonic pairings break time-reversal symmetry. From the previous section, we know that for intermediate values of  $E_G$ , there exists a region where  $\Im[\Delta_1, \Delta_2] \neq 0$ . This is the range of  $E_G$ , where the time-reversal symmetry is spontaneously broken [85].

The time reversal symmetry breaking order parameter is defined in the following way:

$$\mathcal{T}^{\text{br}} = \frac{\Delta_{\text{tot}}^{\text{br}}}{\Delta_{\text{tot}}^{\text{br}} + \Delta_{\text{tot}}^{\text{ts}}} \quad (3.4)$$

where

$$\begin{aligned} (\Delta_{\text{tot}}^{\text{ts}})^2 &= ((\Re[\Delta_2]k_{\text{F}})^2 + (\Re[\Delta_1])^2) \\ (\Delta_{\text{tot}}^{\text{br}})^2 &= ((\Im[\Delta_2]k_{\text{F}})^2 + (\Im[\Delta_1])^2) \end{aligned} \quad (3.5)$$

where the Fermi momentum  $k_{\text{F}} = \sqrt{2mE_G}/\hbar$ . The terms  $\Delta_{\text{tot}}^{\text{br}}$  and  $\Delta_{\text{tot}}^{\text{ts}}$  denote the relative strength of mean field amplitudes breaking and preserving the time-reversal symmetry respectively. For  $A = \Delta_z = 0$ , the exciton condensate phase appears in the

system. As  $A$  and  $\Delta_z$  is switched on, they act as symmetry breaking terms and turns the exciton condensate phase into a crossover, where correlated phases of excitons exist [85]. As is seen from the phase diagram Fig. 3.2, for small and large values of  $A$  and  $E_G$ , the  $\mathcal{T}^{\text{br}}$  is zero. However, there exists a region of non-zero values of  $\mathcal{T}_{\text{br}}$  where the excitons break time-reversal symmetry spontaneously.

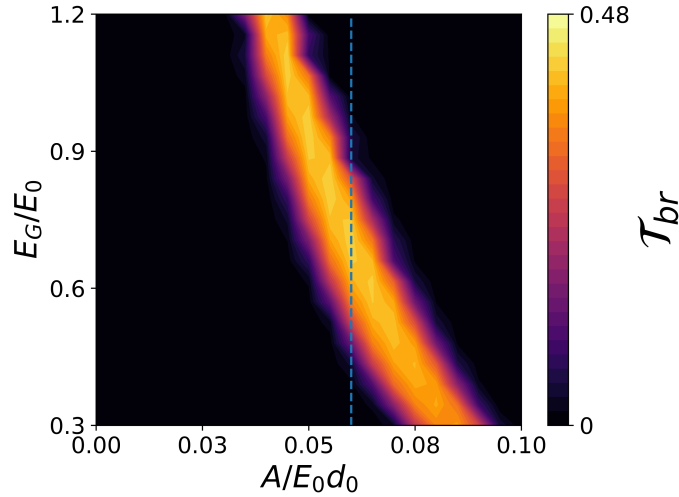


**Figure 3.2:** Phase diagram of the time-reversal symmetry broken order parameter  $\mathcal{T}_{br}$  as a function of  $E_G/E_0$  and  $A/E_0 d_0$ . The dark (colourful) region denotes the region where time-reversal symmetry is preserved (is spontaneously broken). The value of  $k_F$  considers  $m = \hbar = 1$ , therefore  $k_F = \sqrt{2E_G}$ .

In order to identify the topological nature of the phases on either side of this time-reversal symmetry broken phase, a parity operator  $\mathcal{P}$  is introduced. This is an indicator of the topological phase of the system and is defined as:

$$\mathcal{P} = \frac{\Delta_{\text{tot}}^{\text{even}} - \Delta_{\text{tot}}^{\text{odd}}}{\Delta_{\text{tot}}^{\text{even}} + \Delta_{\text{tot}}^{\text{odd}}} \quad (3.6)$$

where

$$\begin{aligned} (\Delta_{\text{tot}}^{\text{even}})^2 &= |\Delta_1|^2 \\ (\Delta_{\text{tot}}^{\text{odd}})^2 &= (|\Delta_2|k_F)^2. \end{aligned} \quad (3.7)$$

Let us now understand why  $\Delta_{\text{tot}}^{\text{even}}(\Delta_{\text{tot}}^{\text{odd}})$  is related to  $|\Delta_1|(|\Delta_2|)$ . When Coulomb interactions are included, the s-wave pairing potential  $\Delta_1$  couples with  $\Delta_z$  term,

whereas the p-wave excitonic potential  $\Delta_2$  pairs with the  $A$ . Therefore, the  $\Delta_1$  and  $\Delta_2$  terms also have even and odd parity respectively. The parity operator defined in (3.6) is similar to the  $Z_2$  topological invariant introduced in the previous chapter. The understanding of the parity operator  $\mathcal{P}$  as the  $Z_2$  topological invariant is only valid when the imaginary parts of the excitonic pairing terms are zero or in other words, the time-reversal symmetry is preserved.

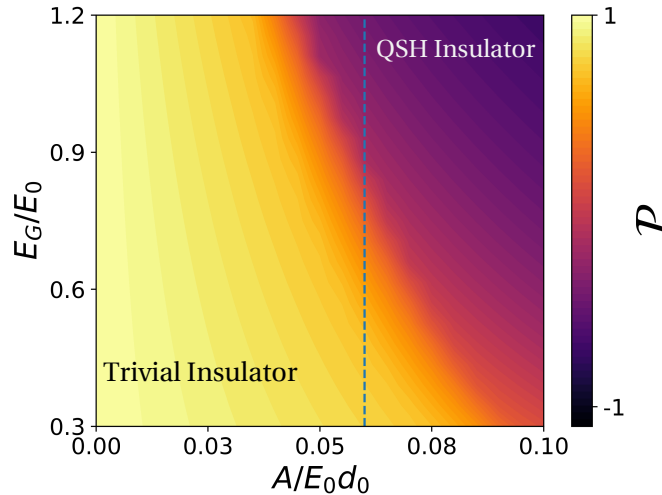


**Figure 3.3:** Parity of order parameter  $\mathcal{P}$  as a function of  $E_G/E_0$  and  $A/E_0 d_0$ . We notice that for even (odd) parity, the system is in trivial (quantum spin Hall) phase.

For small values of  $E_G$  and  $A$ ,  $\Re[\Delta_1] > \Re[\Delta_2]$ , this suggests that  $\mathcal{P} = 1$  as  $\Delta_{\text{tot}}^{\text{even}}$  will dominate in (3.6). On the other hand, for large values of  $E_G$  and  $A$ ,  $\mathcal{P} = -1$  because  $\Delta_{\text{tot}}^{\text{odd}}$  will dominate the even-parity contribution. The change in the sign of  $Z_2$ -like topological invariant for small and large values of  $E_G$  and  $A$  signifies a change in the topological state.

The phase diagrams of time-reversal symmetry order parameter in Fig. 3.2 and parity order parameter in Fig. 3.3, as a function of  $E_G/E_0$  and  $A/E_0 d_0$  are qualitatively similar to phase diagrams presented in Ref. [85]. The simplified mean-field term (3.1), successfully captures the qualitative features of the topological phase transition due to the presence of excitons in Ref. [85]. The energy dispersions for three different values of  $E_G$  for an intermediate value of  $A$  (denoted by the blue dashed line in Fig. 3.2 and Fig. 3.3) confirms the above analysis. For low value of  $E_G$ , the system is in a trivial state and for large values of  $E_G$ , the system has helical

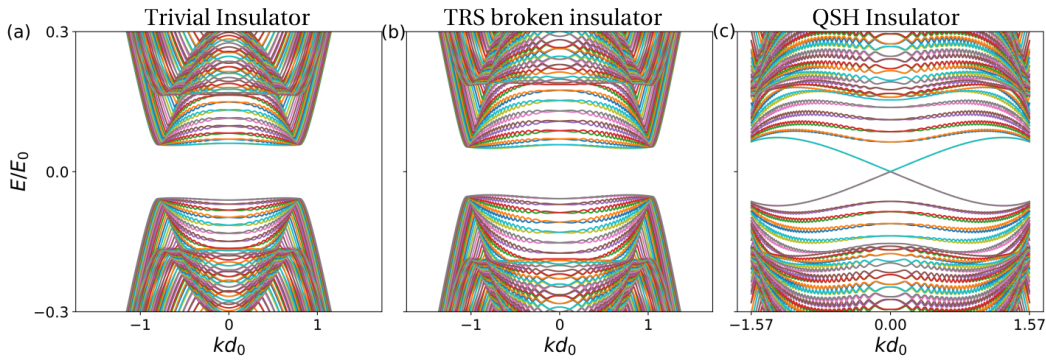


**Figure 3.4:** Energy bands when the system is a (a) trivial, (b) time-reversal symmetry (TRS) and (c) quantum spin Hall (QSH) insulator. As can be seen, the exciton interactions allow a topological phase transition with no bulk gap closing. The energy spectrums were obtained for  $A/E_0d_0 = 0.06$ , which is denoted as a blue dashed line in the phase diagrams for time-reversal symmetry and parity order parameters.

edge states which cross the zero energy at  $\Gamma$  point confirming the quantum spin Hall phase. In Ref. [85], the results have also been analysed from the perspective of Ginzburg-Landau theory where the exciton order parameter (3.1) and the tunneling between the two bands act as a perturbation in the free-energy. The first order terms in the expression of free energy are discussed to be proportional to  $-\Delta_z \Re[\Delta_1]$  and  $-A \Re[\Delta_2]$  and it is energetically favorable to keep the imaginary parts of excitonic pairings to zero. It is the fourth-order terms that try to make the imaginary parts of  $\Delta_1$  and  $\Delta_2$  non-zero and induce a spontaneous time-reversal symmetry broken phase.

A more intuitive way of understanding this interesting phenomenon is, when  $\mathcal{P} = 1$ , both  $A$  and  $\Delta_2$  can be adiabatically made zero, the resulting Hamiltonian resembles a BCS  $s$ -wave superconductor which does not support edge states and is trivial. Similarly, when  $\mathcal{P} = -1$ ,  $\Delta_z$  and  $\Delta_1$  can be turned off, the system becomes a BHZ Hamiltonian which is a quantum spin Hall insulator with helical edge states. In order to minimise the energy during the topological transition, the system remains gapped and therefore, a spontaneous time-reversal symmetry broken phase appears. Therefore, the consequence of introducing Coulomb interactions in the bilayer is a rich topological phase diagram where the bulk gap does not close.

### 3.3 Bulk inversion asymmetry term $\Delta_z$

So far, we have understood the role of modulating  $A$  and  $E_G$  in the bilayer system when Coulomb interactions are allowed. In this section, we will understand the role of  $\Delta_z$  on the phase diagrams for time-reversal symmetry breaking and parity order parameter.

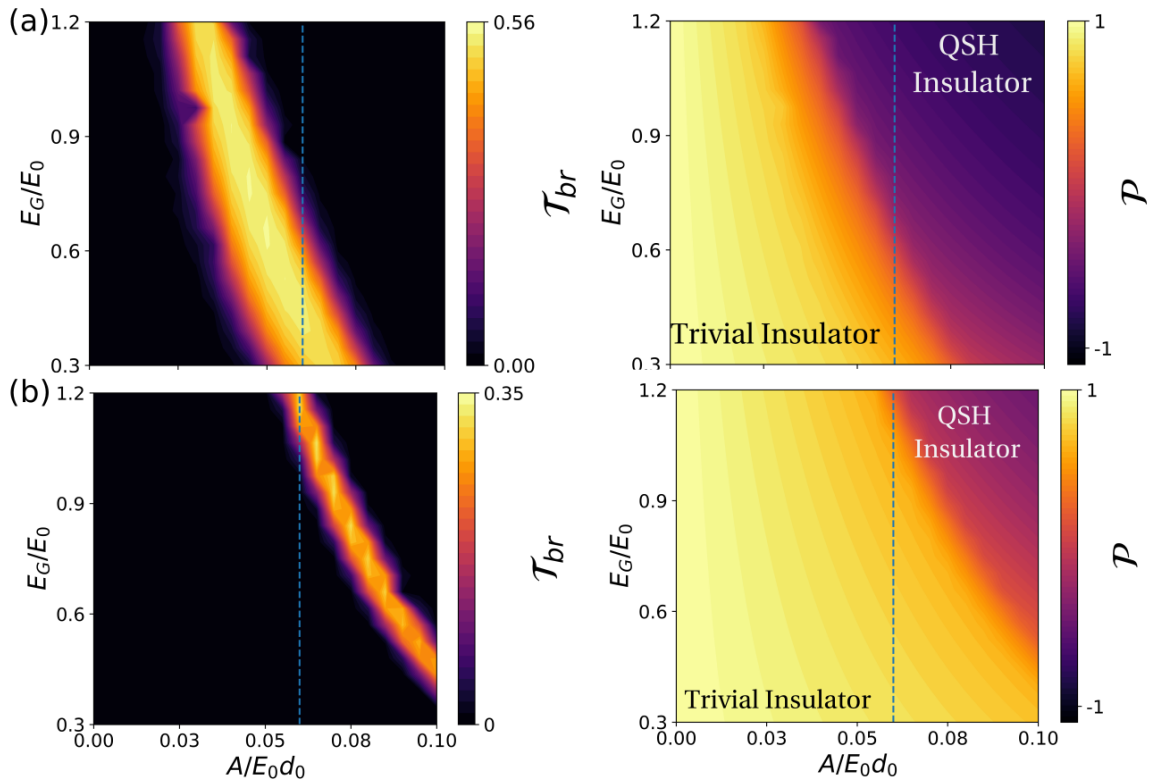


**Figure 3.5:** Phase diagram of time-reversal symmetry breaking and parity order parameter as a function of  $E_G/E_0$  and  $A/E_0 d_0$  for (a)  $\Delta_z = 0.01 E_0$  and (b)  $\Delta_z = 0.04 E_0$

Increasing  $\Delta_z$  has two effects: First, it drives the time-reversal symmetry to break for a larger value of  $A$ . The second effect is the reduction of the area of the time-reversal symmetry broken phase as  $\Delta_z$  increases. As discussed in the previous section, the natural tendency of the system is for the phases of the excitonic pairings to assume zero values. A large magnitude of  $\Delta_z$  forces the system to minimize the free energy and avoids spontaneously breaking the time-reversal symmetry. This could also explain why the type-I quantum wells do not exhibit an exciton condensate phase as

both  $\Delta_z$  and  $A$  are simultaneously larger compared to type-II quantum wells. Therefore, in order to obtain the TRS broken phase, the value of  $\Delta_z$  should be much less than  $0.1E_0$ , since for this value the excitonic pairings is larger than the tunneling amplitude [85].

### 3.4 Mass asymmetry

So far the effect of interactions were considered when the effective mass of electrons and holes are equal. However, InAs/GaSb display an asymmetry in effective masses of the order  $m_e/m_h = 0.84$  [133]. We first check the behaviour of  $\Delta_1$  and  $\Delta_2$  as function  $E_G/E_0$  and  $A/E_0d_0$ , shown as,

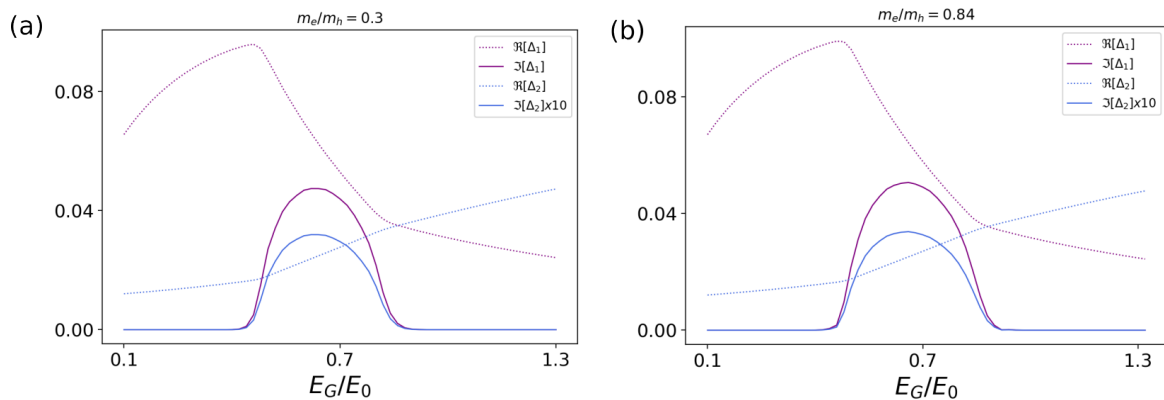


**Figure 3.6:** Phase diagram as a function of  $E_G$  when (a)  $m_e/m_h = 0.3$  and (b)  $m_e/m_h = 0.84$ .

As is visible from the energy phase diagram below, the mass asymmetry does not affect the appearance of the time-reversal symmetry broken phase. Increasing the mass asymmetry by increasing the hole mass, increases the effective mass which raises the critical temperature at which the exciton condensate appears for negligible tunneling term in such bilayers [153].

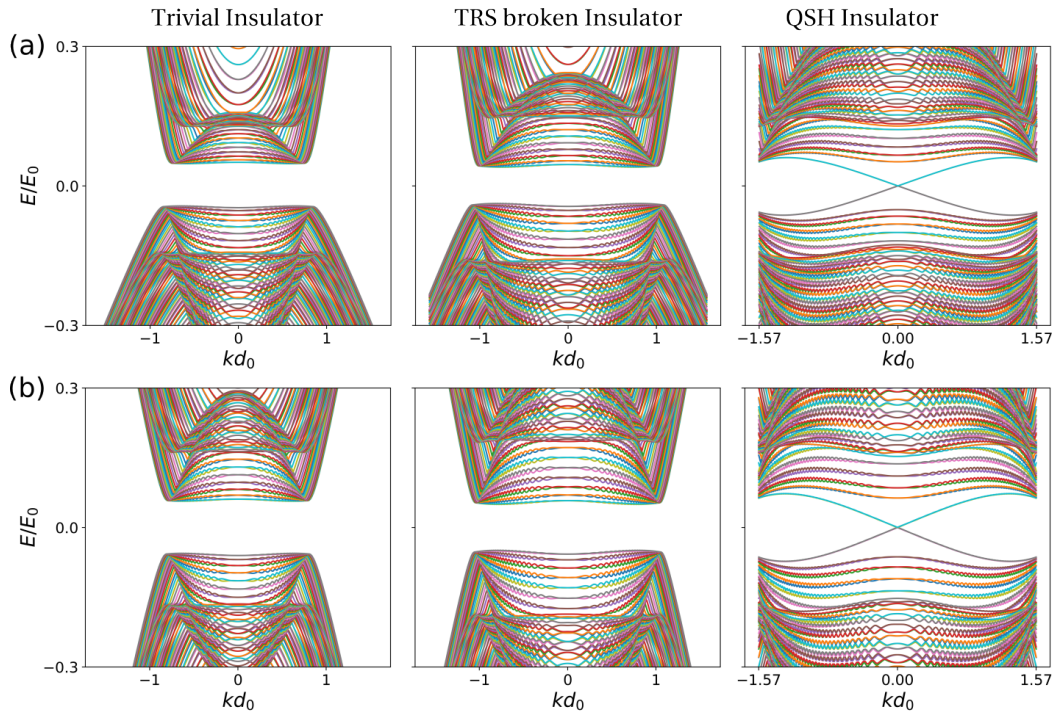


**Figure 3.7:** Energy bands for different values of  $E_G/E_0$  when (a)  $m_e/m_h = 0.3$  and (b)  $m_e/m_h = 0.84$

In this chapter, we have looked into how the excitons in type-II quantum wells, lead to an unconventional topological phase transition where there is no bulk-gap closing. Instead, due to the presence of interactions, the system tries to minimise the Free energy, when it is transitioning from trivial to quantum spin Hall phase. This results in a spontaneously broken time-reversal symmetry phase, where the system becomes an insulator.

## **Chapter 4**

**Paper I: Interplay of quantum spin  
Hall effect and spontaneous  
time-reversal symmetry breaking in  
electron-hole bilayers I. Transport  
properties**

## Summary

The electron-hole bilayer such as InAs/GaSb is a band-inverted system that also supports quantum spin Hall phase as a function of well width and electron-hole densities. However, in experiments, for long samples, this material has shown linearly increasing longitudinal resistance with device length, mean free path of which, is found to be temperature independent for a wide range of temperature of 20mK to 4.2K. An appearance of spontaneously broken time-reversal symmetry phase could allow elastic backscattering processes which may explain the magnitude and temperature independence of the mean free path. As this material is also a candidate for supporting correlated phases of excitons, it has been shown that there is a spontaneous time-reversal symmetry broken phase that appears between trivial and QSH phases in the topological phase diagram as a function of increasing electron-hole densities. The breaking of TRS due to the presence of excitons, leads to an unconventional topological transition where the bulk-gap closing is absent. In the paper below, we present a transport study on a Corbino disc which proposes that this TRS broken phase could be observed in an experiment through measuring bulk and edge conductances as a function of electron-hole densities. As the electron-hole densities are increased, the bulk-conductance remains zero while the edge conductance smoothly takes a quantized value around the Fermi energy, demonstrating the occurrence of a topological transition without bulk-gap closing.

# Interplay of quantum spin Hall effect and spontaneous time-reversal symmetry breaking in electron-hole bilayers. I. Transport properties

Tania Paul <sup>1</sup>, V. Fernández Becerra,<sup>1</sup> and Timo Hyart <sup>1,2,3</sup>

<sup>1</sup>*International Research Centre MagTop, Institute of Physics, Polish Academy of Sciences, Aleja Lotników 32/46, PL-02668 Warsaw, Poland*

<sup>2</sup>*Department of Applied Physics, Aalto University, 00076 Aalto, Espoo, Finland*

<sup>3</sup>*Computational Physics Laboratory, Physics Unit, Faculty of Engineering and Natural Sciences, Tampere University, FI-33014 Tampere, Finland*



(Received 3 June 2022; revised 15 November 2022; accepted 13 December 2022; published 20 December 2022)

The band-inverted electron-hole bilayers, such as InAs/GaSb, are an interesting playground for the interplay of quantum spin Hall effect and correlation effects because of the small density of electrons and holes and the relatively small hybridization between the electron and hole bands. It has been proposed that Coulomb interactions lead to a time-reversal symmetry broken phase when the electron and hole densities are tuned from the trivial to the quantum spin Hall insulator regime. We show that the transport properties of the system in the time-reversal symmetry broken phase are consistent with recent experimental observations in InAs/GaSb. Moreover, we carry out a quantum transport study on a Corbino disk where the bulk and edge contributions to the conductance can be separated. We show that the edge becomes smoothly conducting and the bulk is always insulating when one tunes the system from the trivial to the quantum spin Hall insulator phase, providing unambiguous transport signatures of the time-reversal symmetry broken phase.

DOI: [10.1103/PhysRevB.106.235420](https://doi.org/10.1103/PhysRevB.106.235420)

## I. INTRODUCTION

The advent of topological materials [1,2] has brought band-inverted semiconductors, with small electron and hole densities, to the focus of attention in the search for quantum spin Hall (QSH) insulators [3–8]. However, the electron-electron interactions are important in these materials if the hybridization of the electron and hole bands is small compared to the exciton binding energy, as can be appreciated by noting that the bilayer system of spatially separated electrons and holes is the well-known paradigm system for the realization of an exciton condensate state [9,10]. Indeed, it is now theoretically understood that interactions can lead to a plethora of correlated phases in band-inverted semiconductors [11–17] and recent experiments have shown evidence of excitonic phenomenology in InAs/GaSb quantum wells [18–22] as well as in WTe<sub>2</sub> [23,24]. We concentrate on the correlated phases appearing in the band-inverted electron-hole bilayers shown in Fig. 1(a) [4]. In these systems, the electron and hole bands are spatially separated and therefore only weakly hybridized. Moreover, the electron and hole densities (and hence also the band-inversion parameter  $E_G$ ) can be controlled *in situ* with front and back gate voltages,  $V_f$  and  $V_b$ , allowing the possibility to study the phase transition between trivial and QSH insulator phases [4,22,25], as schematically illustrated in Fig. 1(b). It has been theoretically predicted that, due to the excitonic correlations caused by the Coulomb interactions, a third phase with spontaneously broken time-reversal symmetry (TRS) will appear in the transition regime between the

two topologically distinct phases [11]. Within this phase, the helical edge states, originating from the QSH insulator phase, can exist but they are not protected against backscattering, and it was theoretically demonstrated [11] that these unprotected edge states can explain the temperature-independent mean-free path observed in InAs/GaSb bilayers in the presence of reasonably large applied currents [7,26,27]. However, an unambiguous experimental demonstration of the existence of the exotic insulating phase with spontaneously broken TRS symmetry is still lacking in these systems.

Here we demonstrate that the transport properties of the system in the TRS broken phase are also consistent with more recent transport experiments in InAs/GaSb bilayers with small applied currents [28], so the spontaneous TRS symmetry breaking provides a comprehensive explanation of the temperature, voltage, and length dependencies of the observed conductance [7,26–28]. Finally, we propose an experiment which can be used to unambiguously demonstrate the existence of the spontaneous TRS breaking in this system, namely, we show that the edge becomes smoothly conducting and the bulk remains insulating when one tunes across the TRS broken phase appearing between the trivial and QSH insulator phases in the Corbino geometry, where the bulk and edge contributions to the conductance can be separated [29]. In the presence of TRS symmetry, the bulk transport gap must close when the system is tuned between topologically distinct phases, and hence the experimental demonstration of a transition without a bulk transport gap closing constitutes a proof of an existence of TRS broken insulating phase.

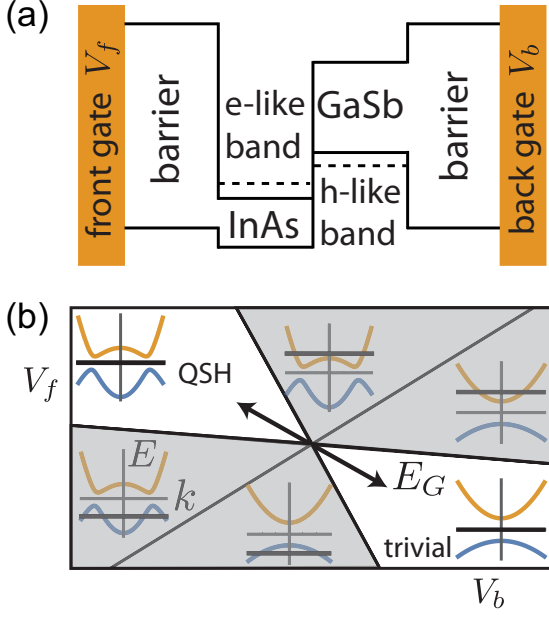


FIG. 1. Schematic illustration of the setup. (a) The densities of the electrons and holes can be controlled with gate voltages  $V_f$  and  $V_b$  in a heterostructure supporting spatially separated electron and hole bands. (b) This way, the gate voltages determine whether the electron and hole bands are inverted at the  $\Gamma$  point ( $E_G > 0$ ) or not ( $E_G < 0$ ), as well as whether the Fermi level (thick black line) is in the conduction band, band gap, or valence band. The insulating phase with  $E_G > 0$  ( $E_G < 0$ ) is the QSH (trivial) insulator phase.

## II. SPONTANEOUS TRS BREAKING IN ELECTRON-HOLE BILAYERS

In Ref. [11], it was shown using a full Hartree-Fock calculation that the Coulomb interactions in the Bernevig-Hughes-Zhang (BHZ) model [3] developed for InAs/GaSb bilayers [4,30] lead to three different phases as a function of the hybridization of the electron and hole bands  $A$  and the band-inversion parameter  $E_G$ , which is defined here so for  $E_G > 0$  ( $E_G < 0$ ) the electron and hole bands are (not) inverted at the  $\Gamma$  point, see Fig. 1(b). As intuitively expected, for small (large)  $A$  and  $E_G$  one realizes a trivial (QSH) insulator phase. However, interestingly, it was found that at intermediate values of  $A$  and  $E_G$  there exists an insulating phase with spontaneously broken TRS symmetry separating the topologically distinct phases. In this section, we describe a simplified *minimal model* that fully captures all the essential results obtained using the full Hartree-Fock calculations in Ref. [11].

The single particle BHZ Hamiltonian is

$$H_0 = \left( \frac{\hbar^2 k^2}{2m} - E_G \right) \tau_z \sigma_0 + A k_x \tau_x \sigma_z - A k_y \tau_y \sigma_0 + \Delta_z \tau_y \sigma_y, \quad (1)$$

where  $\tau$ 's and  $\sigma$ 's denote the Pauli matrices in the electron-hole and spin basis, respectively. The electron band is made out of  $s$  orbitals and the hole band is made out of only two  $p$  orbitals because the electric confining potential and the atomic spin-orbit coupling remove the degeneracies of the

$p$  orbitals. The tunneling between the layers is dominantly odd in momentum and opens a hybridization gap  $\propto A$ . Here, we have assumed the same effective mass  $m$  for electrons and holes, and included only the momentum-independent spin-orbit coupling term  $\Delta_z$  arising due to bulk inversion asymmetry. We have ignored the asymmetry of the masses and the momentum-dependent spin-orbit coupling terms because they are not essential for understanding the phase diagram of the InAs/GaSb bilayers [11].

The main effect of Coulomb interactions is the binding of the electrons and holes into excitons with the characteristic size  $d_0$  and binding energy  $E_0$  determined by the relation  $E_0 = \hbar^2 / (m d_0^2) = e^2 / (4\pi \epsilon_0 d_0)$  [31]. This leads to an excitonic mean field [11],

$$H_{\text{EC}} = \text{Re}[\Delta_1] \tau_y \sigma_y + \text{Re}[\Delta_2] [k_x \tau_x \sigma_z - k_y \tau_y \sigma_0] + \text{Im}[\Delta_1] \tau_x \sigma_y - \text{Im}[\Delta_2] [k_x \tau_y \sigma_z + k_y \tau_x \sigma_0], \quad (2)$$

where  $\Delta_1$  and  $\Delta_2$  are complex bosonic fields describing  $s$ -wave and  $p$ -wave excitonic correlations, respectively. For simplicity, we have expanded the fields  $\Delta_1$  and  $\Delta_2$  only to the lowest order in momentum and neglected the full  $|\mathbf{k}|$  dependence, which is present in the numerical solution of the Hartree-Fock equations [11]. It is easy to see by straightforward calculation that the terms on the first line of Eq. (2) obey the TRS  $T = i\tau_0 \sigma_y K$  ( $K$  is the complex conjugation operator) and the terms in the second line break it. Therefore, the imaginary parts of the fields  $\text{Im}[\Delta_1], \text{Im}[\Delta_2] \neq 0$  result in spontaneous TRS breaking.

We can solve the complex bosonic mean fields  $\Delta_1$  and  $\Delta_2$  by substituting the ansatz Eq. (2) to the Hartree-Fock mean field equations. This way, we arrive at the following mean field equations (see Appendix A for more details):

$$\Delta_1 = \frac{g_s d_0^2}{(2\pi)^2} \int d^2 k [(c_{\mathbf{k}\downarrow 2}^\dagger c_{\mathbf{k}\uparrow 1}) - (c_{\mathbf{k}\uparrow 2}^\dagger c_{\mathbf{k}\downarrow 1})] \quad (3)$$

and

$$\Delta_2 = \frac{g_p d_0^4}{(2\pi)^2} \int d^2 k [-(c_{\mathbf{k}\uparrow 2}^\dagger c_{\mathbf{k}\uparrow 1})(k_x - ik_y) + (c_{\mathbf{k}\downarrow 2}^\dagger c_{\mathbf{k}\downarrow 1})(k_x + ik_y)], \quad (4)$$

where  $g_s$  ( $g_p$ ) is the effective interaction strength for  $s$ -wave ( $p$ -wave) pairing and  $c_{1\sigma k}$  ( $c_{2\sigma k}$ ) is the electron annihilation operator with spin  $\sigma$  and momentum  $k$  in electron (hole) layer. In our numerical calculations, the integration is performed over the range  $|\mathbf{k}| \leq 2.26/d_0$ , but the exact values of the integration limits are not important. The effective interaction strengths  $g_s$  and  $g_p$  can be considered as fitting parameters, whose values should be fixed so one approximately reproduces the results obtained from Hartree-Fock calculations [11].

The values of the model parameters for InAs/GaSb can be estimated by combining theoretical calculations [4,10,11,30] and the experimentally observed energy gaps [7,18]. This way, we arrive at parameter values that are used in our calculations:  $E_0/k_B = 200$  K,  $d_0 = 10$  nm,  $A/(E_0 d_0) = 0.06$ ,  $\Delta_z/E_0 = 0.02$ ,  $g_s/E_0 = 1.0$ , and  $g_p/E_0 = 0.2$ . The band-inversion parameter  $E_G$  is a gate-tunable parameter (see Fig. 1), which is varied in our calculations to tune the system from a trivial

insulator to QSH insulator phase. As shown in Fig. 2, our simplified mean field approach, defined by Eqs. (1)–(4), reproduces the results obtained from full Hartree-Fock calculations [11]. For small (large) values of  $E_G$ , the system is in a trivial (QSH) insulator phase and, importantly, these two phases are separated from each other by an insulating phase with spontaneously broken TRS, where  $\text{Im}[\Delta_1], \text{Im}[\Delta_2] \neq 0$ . The bulk gap  $\Delta_{\text{bulk}}$  remains open for all values of  $E_G$  because the intermediate TRS broken phase enables the connection of the topologically distinct phases without bulk gap closing. The edge gap  $\Delta_{\text{edge}}$  decreases monotonously when one starts from the trivial phase and tunes the system across the TRS broken phase to the QSH phase, where the gapless edge excitations are protected by the topology. Here,  $\Delta_{\text{bulk}}$  and  $\Delta_{\text{edge}}$  have been computed from the spectra of an infinite system and a wide ribbon with open boundary conditions, respectively. The width of the ribbon  $W = 500d_0$  is sufficiently large so the finite size effects are negligible. The formation of the edge gap  $\Delta_{\text{edge}}$  due to the breaking of the TRS occurs in two different ways. The excitonic mean field  $\text{Im}[\Delta_1]$  couples the spin-up and spin-down edge modes directly, whereas  $\text{Im}[\Delta_2]$  contributes to the gap via a higher order process where it is combined with a spin-orbit coupling term  $\Delta_z$  and excitonic mean field  $\text{Re}[\Delta_1]$ .

The appearance of spontaneous TRS breaking can be understood with the help of topological considerations. The topological invariant distinguishing the QSH phase from the trivial insulator can change only if (i) *the bulk energy gap closes* or (ii) *TRS is broken in a regime between the topologically distinct phases*. The case (i) would be the only possibility if the local order were fixed. However, in an interacting system the order parameter corresponds to a minimum of the free energy, and it is energetically favorable to keep the system gapped. Due to this reason, there is a general tendency for the appearance of a TRS broken phase in the transition regime between QSH and trivial insulator phases.

### III. LENGTH, TEMPERATURE AND VOLTAGE DEPENDENCE OF THE CONDUCTANCE

The identification of the edge states in InAs/GaSb bilayers was initially problematic due to finite bulk density of states in the minigap [6]. The main breakthrough in eliminating the bulk conduction came from insertion of Si to the interface between the InAs and GaSb layers during the growth process [7]. After achieving a truly insulating bulk this way, Du *et al.* [7] managed to demonstrate in mesoscopic samples wide conductance plateaus quantized to the values expected for nonlocal helical edge transport (variations less than 1%). The accurate conductance quantization was reported for several devices of various lengths and three different geometries in Ref. [7]. Moreover, by imaging the distribution of the current flow inside the sample it has been confirmed that the current flows along the edge in agreement with helical edge conduction [27]. More careful measurements of temperature and voltage dependencies are also consistent with single-mode edge conduction [28]. In a different type of sample, where Si was not inserted and the observed thermal activation gap for the bulk transport is an order of magnitude smaller, multimode edge conduction has been reported by another group [33]. The

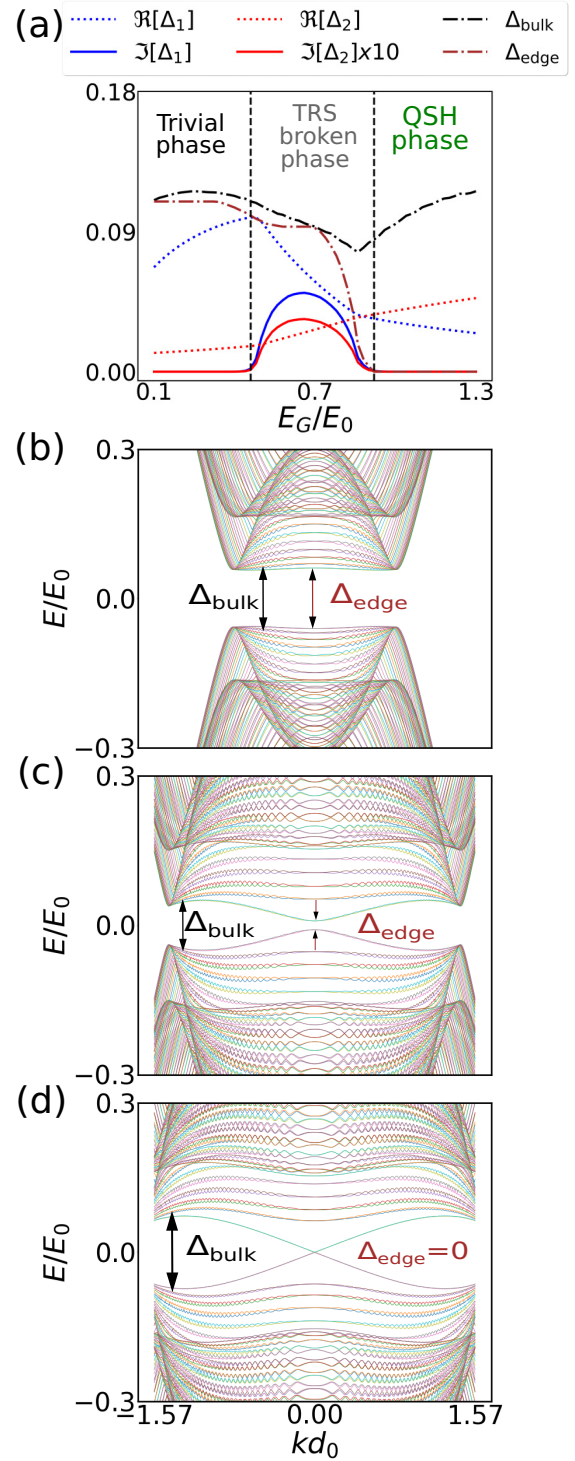


FIG. 2. (a) Phase diagram as a function of  $E_G$ . The trivial and QSH phases obey the TRS. In the TRS broken phase, the  $s$ - and  $p$ -wave excitonic mean fields obey  $\text{Im}[\Delta_1], \text{Im}[\Delta_2] \neq 0$ . The bulk gap  $\Delta_{\text{bulk}}$  remains open for all values of  $E_G$  and the edge gap  $\Delta_{\text{edge}}$  decreases from the bulk gap value to zero, when one tunes  $E_G$  across the TRS broken phase toward the QSH phase. The model parameters are described in the text. Energy bands in (b) trivial phase with  $E_G = 0.3E_0$ , (c) TRS broken phase with  $E_G = 0.86E_0$ , and (d) QSH phase with  $E_G = 1.12E_0$ . The eigenenergies are obtained by diagonalizing the tight-binding Hamiltonian which is generated from the continuum Hamiltonian, defined by Eqs. (1)–(4), using the KWANT software package [32].

explanation of the remarkably different transport properties observed in the presence and in absence of Si doping remains an open theoretical problem, but one possible explanation is that there exists additional unprotected edge modes [34] in the absence of Si doping, which are then shifted out of the energy gap in the presence of the Si doping. Because these observations in the two different types of samples are so different that they cannot be explained with the same model Hamiltonian, we concentrate here on the transport experiments in Si-doped samples with a large activation gap [7,28]. We show that these experiments are consistent with the transport properties theoretically obtained in the TRS broken phase.

In long samples, the conductance is not observed to be quantized [7], indicating that backscattering processes occur between the counterpropagating edge channels. It was found that in the limit  $eV \gg k_B T$ , the resistance is independent on temperature between 20 mK–4.2 K and it increases linearly with the edge length  $L$ . These observations are not surprising once the elastic backscattering processes are allowed and large voltage is applied, because under these conditions the inelastic scattering rate is expected to be approximately equal to the elastic one [35] and therefore the localization effects can be neglected and the resistance is expected to be temperature independent. In the QSH phase, the elastic backscattering is forbidden in the presence of TRS due to the topological protection, so these observations are not consistent with the system being in the QSH phase without additional assumptions about the existence of charge puddles that may lead to enhanced backscattering rate [36]. On the other hand, the TRS broken phase supports edge states but the elastic backscattering is now allowed, so the experimental observations are fully consistent with the system being in the TRS broken phase. Thus, the TRS broken phase provides an intrinsic explanation of these experiments, remaining applicable even if we assume that the samples are of high quality so no charge puddles are present in the system.

In short mesoscopic samples with small applied voltage and temperature, the voltage and temperature dependencies of the conductance are more complicated and we need to use a quantum transport approach to describe them. The disorder-averaged differential conductance  $G_d = dI/dV$  is obtained from

$$G_d(E_F + eV, T) = \int_{-\infty}^{+\infty} dE \frac{2G_0 \exp[-L/\ell(E)]}{4k_B T \cosh^2 \frac{E - E_F - eV}{2k_B T}}, \quad (5)$$

where  $G_0 = e^2/h$ ,  $E_F$  is the Fermi energy,  $V$  is voltage,  $T$  is temperature of the reservoirs,  $L$  is the length of the sample, and  $\ell(E)$  is the energy-dependent elastic mean-free path, which for  $E \gg \Delta_{\text{edge}}$  is given by [11]

$$\ell(E) = \frac{4a\hbar^2 v^2 E^2}{\xi V_{\text{dis}}^2 \Delta_{\text{edge}}^2}. \quad (6)$$

Here,  $E$  is the energy relative to the energy of the crossing of the edge states,  $v$  is the edge velocity,  $V_{\text{dis}}$  is the strength of the disorder potential,  $\xi$  is the disorder correlation length, and  $a \sim 1$  is a numerical factor. Although the exact expression for  $\ell(E)$  is model dependent, it must always satisfy  $\ell(E) \rightarrow \infty$  for  $E \gg \Delta_{\text{edge}}$ , so  $G_d \approx 2G_0$  for  $k_B T \gg \Delta_{\text{edge}}$ . Therefore,

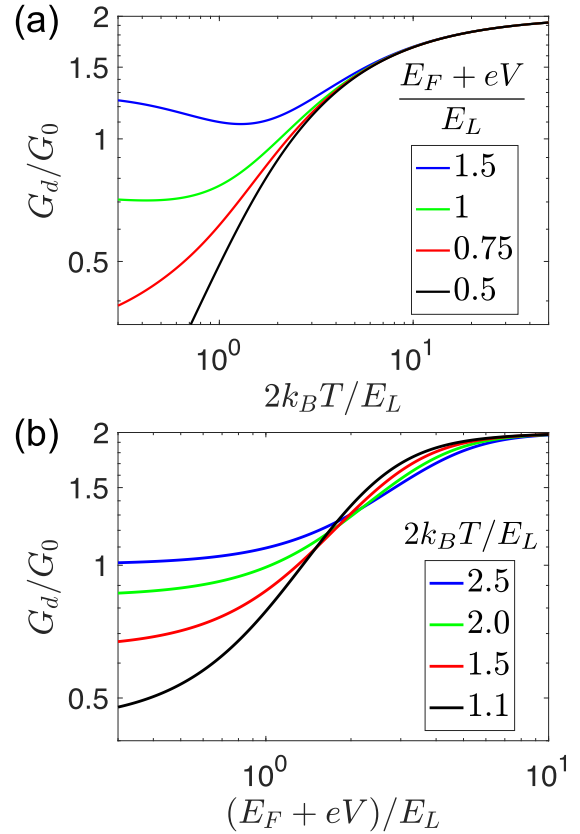


FIG. 3. (a) Differential conductance  $G_d$  as a function of  $T$  for  $(E_F + eV)/E_L = 1.5, 1, 0.75, 0.5$ . (b)  $G_d$  as a function of  $V$  for  $2k_B T/E_L = 2.5, 2, 1.5, 1.1$ .

there exists robust asymptotic limits

$$G_d \approx \begin{cases} 2G_0[1 - L/\ell(E_F + eV)], & k_B T \ll E_F + eV, \\ 2G_0, & k_B T \gg \Delta_{\text{edge}}, \end{cases} \quad (7)$$

which guarantee that  $G_d$  undergoes a crossover from non-quantized value to the quantized value  $G_d = 2G_0$ , both with increasing temperature and voltage.

To study the full temperature dependence, we introduce an energy scale  $E_L$ , which is defined in such a way that

$$\ell(E_L) \equiv L, \text{ i.e. } E_L = \sqrt{\frac{L\xi V_{\text{dis}}^2 \Delta_{\text{edge}}^2}{4a\hbar^2 v^2}}. \quad (8)$$

The differential conductance  $G_d$ , which depends on two parameters  $(E_F + eV)/E_L$  and  $2k_B T/E_L$ , is shown in Fig. 3. In this analysis, we have neglected the effects of electron-electron interactions beyond the mean-field theory and the energy and temperature dependence of the excitonic mean fields. Nevertheless, our results for the  $G_d$  crossovers from a nonquantized to the quantized value  $G_d = 2G_0$  with increasing voltage and temperature are in reasonable agreement with the experimental observations [28]. We consider the observations of these crossovers as very strong evidence of single-mode edge transport.

In the experiment [28], the temperature dependence of the conductance

$$G(E_F, V, T) = \frac{1}{V} \int_0^V dV G_d(E_F + eV, T) \quad (9)$$

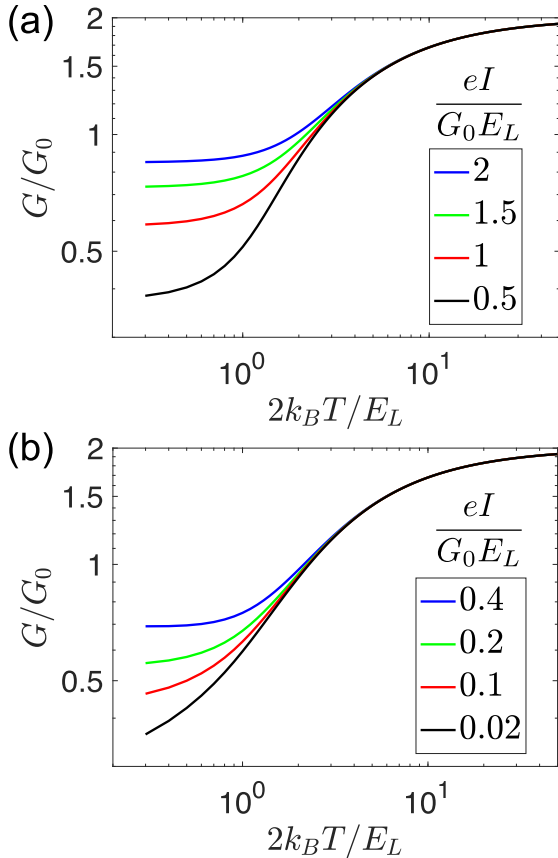


FIG. 4. (a) Conductance  $G$  as a function of  $T$  for  $E_F = 0$  and  $eI/(G_0 E_L) = 2, 1.5, 1, 0.5$ . (b) Same for  $E_F/E_L = 0.7$  and  $eI/(G_0 E_L) = 0.4, 0.2, 0.1, 0.02$ .

was reported also in a current  $I$  biased situation. The theoretical predictions for this situation, obtained using Eqs. (5), (6), (9), and  $I = GV$ , are shown in Fig. 4. In this case, the shapes of the curves in the crossover regime depend on the Fermi energy  $E_F$  and they resemble the experimental observations [28] more in the case of reasonably large values of  $E_F$ . In a more detailed microscopic description, the crossing of the edge states may be buried within the bulk bands [37,38] so reasonably large  $E_F$  compared the energy of the crossing could naturally be realized in the experiments.

The qualitative features observed in the transport experiments discussed above have been previously explained using various different mechanisms. The advantage of our approach is that a single mechanism provides a unified and comprehensive explanation for all these observations and this mechanism is also consistent with the other evidence of excitonic phenomenology in InAs/GaSb quantum wells [18–22]. We point out that the experimentally observed crossovers as a function of voltage and current already show clear saturation toward the quantized value [28], but the observation of an equally clear signature as a function of temperature may require optimization of the sample size because the saturation should occur at sufficiently low temperature so thermally activated bulk transport does not contribute significantly to the conductance. The quantitative comparison to the experiments goes beyond the scope of this paper because, in the crossover regime, the conductance depends on the Luttinger parameter

describing the interactions at the edge and the temperature and energy dependencies of the excitonic mean fields. We expect that once these effects are taken into account, our theory provides a reasonably good quantitative description of all the transport regimes as a function of temperature, voltage, current, and sample size.

#### IV. DECOUPLING OF BULK AND EDGE TRANSPORT IN CORBINO GEOMETRY

We have shown that the transport experiments performed so far with InAs/GaSb devices are consistent with the system being in the TRS broken phase. However, it is difficult to rule out other theoretical explanations [36,39–43] based on these experimental observations. In this section, we propose a transport experiment, which could be used to prove the existence of the exotic TRS broken phase based on robust topological arguments. This kind of experiment would also directly probe the main difference between the transport theories because our theory is so far the only proposal where the backscattering originates from the spontaneous TRS breaking in the bulk.

For this purpose, we consider a Corbino device where the differential conductances corresponding to the bulk  $G_{\text{bulk}}$  and edge  $G_{\text{edge}}$  transport can be decoupled as illustrated in Fig. 5. The dimensions of the Corbino disk  $R_{\text{in}} \approx 1 \mu\text{m}$  and  $R_{\text{out}} = 2 \mu\text{m}$  are chosen so the transport is (approximately) ballistic and the decay lengths of the evanescent bulk modes in the middle of the bulk gap are much shorter than the transport paths. This guarantees that  $G_{\text{bulk}} \approx 0$  for the applied voltage satisfying  $|eV_{dc}| < \Delta_{\text{bulk}}/2$ . Importantly, this allows us to demonstrate that the transport gap does not close when the system is tuned from trivial to the QSH insulator phase by varying  $E_G$  [see Fig. 5(b)]. On the other hand, the edge conductance changes smoothly from  $G_{\text{edge}} = 0$  (trivial phase) to  $G_{\text{edge}} = 2G_0$  (QSH phase) upon increasing  $E_G$ , demonstrating the closing of the edge gap  $\Delta_{\text{edge}}$  at the transition to the QSH insulator phase [see Fig. 5(c)]. Importantly, the bulk and edge conductances can be elegantly measured in the same device when the system is tuned *in situ* from the trivial to the QSH insulator phase using the gate voltages. Such kind of experimental demonstration of a topological transition without a bulk transport gap closing would constitute proof of the existence of TRS broken insulating phase.

In Appendices B and C, we consider the effects of mass asymmetry and disorder on the bulk and edge conductances in the Corbino device. We find that although the high-energy bulk transport is significantly affected by these effects, all the important qualitative features in the low-energy transport are robust also in the presence of large mass asymmetry and strong disorder.

#### V. CONCLUSIONS AND DISCUSSION

We have discussed the possibility of unconventional topological phase transition between trivial and QSH insulator phases in band-inverted electron-hole bilayers. The hallmark of this transition is the existence of an intermediate insulating phase with spontaneously broken TRS. We have demonstrated that the transport properties of the system in the TRS broken phase are consistent with the observed transport

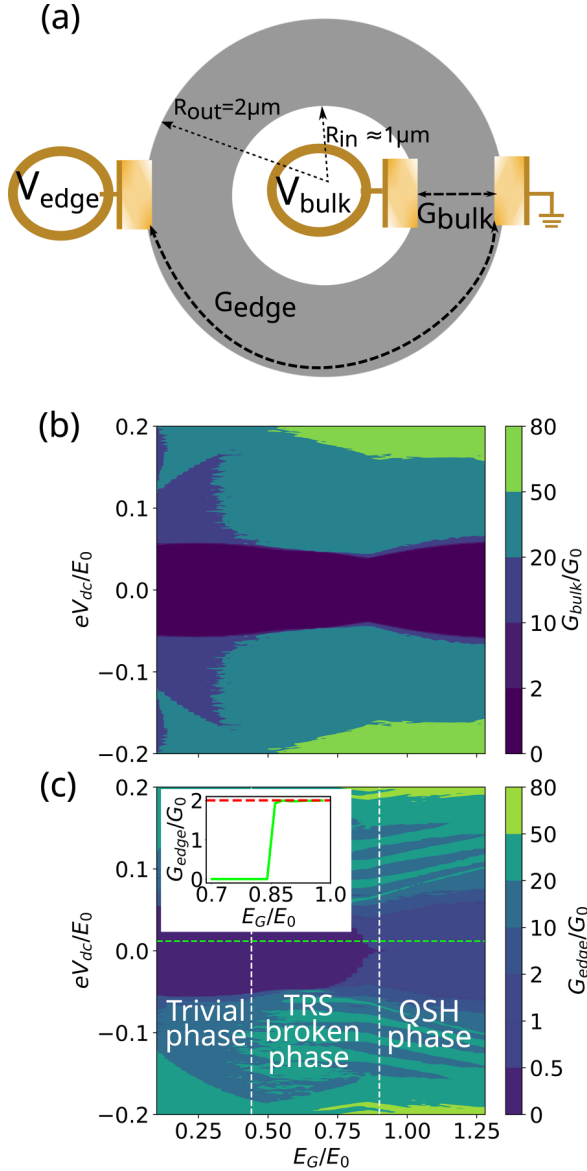


FIG. 5. (a) Schematic illustration of a Corbino device and the transport paths corresponding to the bulk and edge differential conductances  $G_{\text{bulk}}$  and  $G_{\text{edge}}$ . The dimensions of the Corbino disk  $R_{\text{in}} \approx 1 \mu\text{m}$  and  $R_{\text{out}} = 2 \mu\text{m}$  are chosen so the transport is (approximately) ballistic and the decay lengths of the evanescent bulk modes in the middle of the bulk gap are much shorter than the transport paths. (b), (c)  $G_{\text{bulk}}$  and  $G_{\text{edge}}$  as a function of  $E_G$  and applied voltage  $V_{\text{dc}}$ . The inset in (c) shows  $G_{\text{edge}}$  as a function of  $E_G$  (green line) for  $eV_{\text{dc}} = 0.012E_0$ . The red dashed line is a guide to the eye. The conductances have been calculated with the help of the tight-binding Hamiltonian which is generated from the continuum Hamiltonian, defined by Eqs. (1)–(4), using the KWANT software package [32].

characteristics of InAs/GaSb devices, and we have shown that the measurement of the bulk and edge conductances in a Corbino device can provide unambiguous transport signatures of a topological transition without a bulk transport gap closing, proving the existence of the TRS broken phase. In this paper, we have demonstrated that because of the TRS broken phase the edge becomes smoothly conducting when one tunes the system from the trivial to the QSH insulator phase, and

we expect similar smooth transitions also in other observables related to the topological invariant. For example, the spin Hall conductivity is expected to change smoothly in the case of unconventional transition via the TRS broken phase although it changes abruptly in the case of a conventional transition with a bulk gap closing. We expect that the spontaneous TRS breaking would also show up in the spectrum of the collective modes. In this work we have assumed that the disorder is not so strong that it would influence the excitonic mean fields, but we think that the investigation of the effect of strong disorder on the appearance of the spontaneous TRS breaking would be an important direction for future research.

Although we have focused on InAs/GaSb bilayers, we point out that band-inverted electron-hole systems can be realized in many semiconducting bilayers by creating a strong electric field at the barrier between the layers [44–48]. In principle, all these systems are potential candidates for supporting the interplay of excitonic correlations and the QSH effect, but for most of the semiconductors the barrier thickness may have to be so large that the hybridization gap between the electron and hole bands becomes too small to realize a sufficiently large topological gap in the QSH insulator phase. Our theory may also be applicable to HgTe bilayers [12].

Finally, we point out that if an insulating barrier is inserted between the electron and hole layers to suppress the tunneling between the layers, the excitonic correlations can be probed also with the help of a Josephson-like tunneling anomaly and counterflow supercurrents as demonstrated in quantum Hall exciton condensates [49–54] and more recently in double bilayer graphene systems where the exciton condensate is realized in the absence of magnetic field [55–57]. The tunneling barrier also allows us to study the physics discussed in this paper in more detail because it affects the competition between the  $s$ -wave and  $p$ -wave excitonic mean fields and the appearance of the TRS broken phase [11].

In a separate work [58], we show that in the presence of induced superconductivity the spontaneous TRS breaking allows us to realize Majorana zero modes in the absence of magnetic field.

## ACKNOWLEDGMENTS

We thank D. I. Pikulin for useful discussions and comments. The paper is supported by the Foundation for Polish Science through the IRA Programme cofinanced by EU within SG OP and the Academy of Finland Project No. 331094. We acknowledge the computational resources provided by the Aalto Science-IT project and the access to the computing facilities of the Interdisciplinary Center of Modeling at the University of Warsaw, Grants No. GB82-13, No. G78-13, and No. G75-10.

## APPENDIX A: MINIMAL MODEL AND MEAN-FIELD EQUATIONS FOR EXCITONIC CORRELATIONS

Based on the numerical solution of the Hartree-Fock mean field theory [11], we know that the main effect of intraband interactions (in the relevant part of the parameter space) is to renormalize the band structure. Therefore, we consider only

the interband interactions

$$\hat{H}_I = - \sum_{s,s'} \sum_{\mathbf{k},\mathbf{k}'} V_{\mathbf{k},\mathbf{k}'} c_{\mathbf{k}s1}^\dagger c_{\mathbf{k}s'2} c_{\mathbf{k}'s'2}^\dagger c_{\mathbf{k}'s1}, \quad (\text{A1})$$

$$Q_{\uparrow\uparrow} = \begin{pmatrix} 0 & 0 & 0 & 0 \\ 0 & 0 & 0 & 0 \\ 1 & 0 & 0 & 0 \\ 0 & 0 & 0 & 0 \end{pmatrix}, \quad Q_{\uparrow\downarrow} = \begin{pmatrix} 0 & 0 & 0 & 0 \\ 0 & 0 & 0 & 0 \\ 0 & 0 & 0 & 0 \\ 1 & 0 & 0 & 0 \end{pmatrix},$$

where  $V_{\mathbf{k},\mathbf{k}'}$  describes the Coulomb interactions between the layers. On a mean-field level, the Hamiltonian is

$$\hat{H}_{\text{mf}} = \hat{H}_0 - \sum_{\mathbf{k},s,s'} [\Delta_{ss'}(\mathbf{k}) c_{\mathbf{k}s1}^\dagger c_{\mathbf{k}s'2} + \text{H.c.}], \quad (\text{A2})$$

$$Q_{\downarrow\uparrow} = \begin{pmatrix} 0 & 0 & 0 & 0 \\ 0 & 0 & 0 & 0 \\ 0 & 1 & 0 & 0 \\ 0 & 0 & 0 & 0 \end{pmatrix}, \quad Q_{\downarrow\downarrow} = \begin{pmatrix} 0 & 0 & 0 & 0 \\ 0 & 0 & 0 & 0 \\ 0 & 0 & 0 & 0 \\ 0 & 1 & 0 & 0 \end{pmatrix}, \quad (\text{A5})$$

where

$$\Delta_{s,s'}(\mathbf{k}) = \sum_{\mathbf{k}'} V_{\mathbf{k},\mathbf{k}'} f_{s,s'}(\mathbf{k}'), \quad (\text{A3})$$

$$f_{s,s'}(\mathbf{k}) \equiv \langle c_{\mathbf{k}s'2}^\dagger c_{\mathbf{k}s1} \rangle = \sum_m n_F(E_{m\mathbf{k}}) [U_{\mathbf{k}} Q_{ss'} U_{\mathbf{k}}^\dagger]_{mm}, \quad (\text{A4})$$

$n_F(E) = (e^{E/(k_B T)} + 1)^{-1}$  is the Fermi function,  $T$  is the temperature, and the transformation  $U_{\mathbf{k}}$  diagonalizes

$$\text{diag}(E_{1\mathbf{k}}, E_{2\mathbf{k}}, E_{3\mathbf{k}}, E_{4\mathbf{k}}) = U_{\mathbf{k}} H_{\text{mf}}(\mathbf{k}) U_{\mathbf{k}}^\dagger, \quad (\text{A6})$$

the mean-field Hamiltonian:

$$H_{\text{mf}}(\mathbf{k}) = \begin{pmatrix} \frac{\hbar^2 k^2}{2m} - E_G & 0 & (A + \Delta_2)(k_x + ik_y) & -(\Delta_1 + \Delta_z) \\ 0 & \frac{\hbar^2 k^2}{2m} - E_G & (\Delta_1 + \Delta_z) & -(A + \Delta_2)(k_x - ik_y) \\ (A + \Delta_2)^*(k_x - ik_y) & (\Delta_1 + \Delta_z)^* & E_G - \frac{\hbar^2 k^2}{2m} & 0 \\ -(\Delta_1 + \Delta_z)^* & -(A + \Delta_2)^*(k_x + ik_y) & 0 & E_G - \frac{\hbar^2 k^2}{2m} \end{pmatrix}. \quad (\text{A7})$$

Here we have utilized the fact that the excitonic mean field can be approximated as

$$\Delta^{\text{mf}} = i\Delta_1\sigma_2 - \Delta_2(k_x\sigma_3 + ik_y\sigma_0), \quad (\text{A8})$$

where  $\Delta_1$  and  $\Delta_2$  are complex bosonic fields describing  $s$ -wave and  $p$ -wave excitonic correlations, respectively.

By inverting the interaction matrix and substituting the ansatz Eq. (A8) to the mean-field equation, we obtain

$$\frac{d_0^2}{L^2} \sum_{\mathbf{k}} [f_{\uparrow,\downarrow}(\mathbf{k}) - f_{\downarrow,\uparrow}(\mathbf{k})] = 2 \frac{d_0^2}{L^2} \sum_{\mathbf{k},\mathbf{k}'} V_{\mathbf{k}\mathbf{k}'}^{-1} \Delta_1 = \frac{1}{g_s} \Delta_1 \quad (\text{A9})$$

and

$$\frac{d_0^2}{L^2} \sum_{\mathbf{k}} [-f_{\uparrow,\uparrow}(\mathbf{k})(k_x - ik_y) + f_{\downarrow,\downarrow}(\mathbf{k})(k_x + ik_y)] = 2 \frac{d_0^2}{L^2} \sum_{k,k'} V_{\mathbf{k},\mathbf{k}'}^{-1} \Delta_2(k_x k'_x + k_y k'_y) = \frac{1}{g_p d_0^2} \Delta_2, \quad (\text{A10})$$

where we have defined effective interaction strengths  $g_s$  and  $g_p$  for the  $s$ -wave and  $p$ -wave excitonic correlations as

$$g_s^{-1} = 2 \frac{d_0^2}{L^2} \sum_{k,k'} V_{\mathbf{k},\mathbf{k}'}^{-1}, \quad g_p^{-1} = 2 \frac{d_0^4}{L^2} \sum_{k,k'} V_{\mathbf{k},\mathbf{k}'}^{-1} (k_x k'_x + k_y k'_y). \quad (\text{A11})$$

The length scale  $d_0$  is introduced to guarantee that the interaction strengths have a unit of energy, and it can in principle be chosen arbitrarily. However, we know that in the case of Coulomb interaction the natural length  $d_0$  and energy  $E_0$  scales are determined so the kinetic and interaction energies are equal:

$$E_0 = \frac{\hbar^2}{d_0^2} \frac{1}{m} = \frac{1}{4\pi\epsilon\epsilon_0} \frac{e^2}{d_0}. \quad (\text{A12})$$

This way, we obtain the mean field Eqs. (3) and (4) given in the main text.

## APPENDIX B: EFFECTS OF EFFECTIVE MASS ASYMMETRY ON THE TRANSPORT CHARACTERISTICS IN THE CORBINO DEVICES

In typical semiconductors, the effective masses of the electrons  $m_e$  and holes  $m_h$  are different. It was shown in Ref. [11] that this does not influence the phase diagram of InAs/GaSb

bilayer qualitatively if one uses the first-principle estimate for the effective mass asymmetry  $m_e/m_h = 0.84$  [30]. Here, we study the effects of the effective mass asymmetry on the results reported in the main text of this paper.

In the presence of the effective mass asymmetry, the exciton binding energy and radius are determined from the equation

$$E_0 = \frac{\hbar^2}{2m_{\text{eff}} d_0^2} = \frac{1}{4\pi\epsilon\epsilon_0} \frac{e^2}{d_0}, \quad (\text{B1})$$

where the reduced mass  $m_{\text{eff}}$  satisfies equation  $m_{\text{eff}}^{-1} = m_e^{-1} + m_h^{-1}$ . Moreover, the mean-field Hamiltonian can be written as

$$H_{\text{mf}}(\mathbf{k}) = \begin{pmatrix} \frac{\hbar^2 k^2}{2m_e} - \frac{2m_{\text{eff}}}{m_e} E_G & 0 & (A + \Delta_2)(k_x + ik_y) & -(\Delta_1 + \Delta_z) \\ 0 & \frac{\hbar^2 k^2}{2m_e} - \frac{2m_{\text{eff}}}{m_e} E_G & (\Delta_1 + \Delta_z) & -(A + \Delta_2)(k_x - ik_y) \\ (A + \Delta_2)^*(k_x - ik_y) & (\Delta_1 + \Delta_z)^* & \frac{2m_{\text{eff}}}{m_h} E_G - \frac{\hbar^2 k^2}{2m_h} & 0 \\ -(\Delta_1 + \Delta_z)^* & -(A + \Delta_2)^*(k_x + ik_y) & 0 & \frac{2m_{\text{eff}}}{m_h} E_G - \frac{\hbar^2 k^2}{2m_h} \end{pmatrix}. \quad (\text{B2})$$

Notice that if  $m_e = m_h = m$ , we obtain  $m_{\text{eff}} = m/2$ , and therefore these equations reduce back to the equations considered in the main text. Moreover, we have defined  $E_G$  analogously with the earlier analysis: tuning  $E_G$  allows us to vary the electron and hole densities so they remain equal to each other.

The transport characteristics in the Corbino geometry for  $m_e/m_h = 0.84, 0.3$  are shown in Fig. 6. By comparing Fig. 6 to Fig. 5, we conclude that the low-energy transport characteristics are unaffected by the effective mass asymmetry, but the asymmetry leads to visible changes in the bulk conductance at high energies.

### APPENDIX C: EFFECTS OF DISORDER ON THE TRANSPORT CHARACTERISTICS IN THE CORBINO DEVICES

In Ref. [11], it was shown that in the presence of spontaneous TRS breaking the nonmagnetic disorder can cause backscattering. The more detailed length, temperature, and voltage dependence of the conductance in the presence of the disorder was discussed in Sec. III. In Sec. IV, we concentrated on the transport characteristics in mesoscopic Corbino devices where the mean-free path of the edge modes is longer than the distance between the contacts but the decay length of

the evanescent bulk modes in the middle of the gap is much shorter than the width of the Corbino ring. In such kind of situation, we expect that the disorder is unimportant for the low-energy transport characteristics but it can influence the conductance at energies above the bulk gap. In this Appendix, we explicitly calculate the effects of a disorder potential on the conductances in this geometry by modeling the disorder as uncorrelated uniformly distributed on-site energies between  $[-V_{\text{dis}}, V_{\text{dis}}]$ . We assume that the disorder is not so strong that it would influence the excitonic mean fields. In particular, this assumption is justified in the range of the disorder strengths where the effects of the disorder can be treated using the self-consistent Born approximation [59,60], because in this case the disorder just renormalizes the band structure parameters so the phase diagram remains qualitatively the same.

In Fig. 7, we show the edge and bulk conductance as a function of  $E_G$  and  $eV_{\text{dc}}$  in the case of moderate  $V_{\text{dis}} = 0.1E_0$  and strong  $V_{\text{dis}} = 0.5E_0$  disorder strengths. The results show that the main qualitative transport features, i.e., the bulk gap remains open while the edge gap smoothly decreases to zero in the TRS-broken phase, can be observed also in the presence of strong disorder. The bulk conductance is

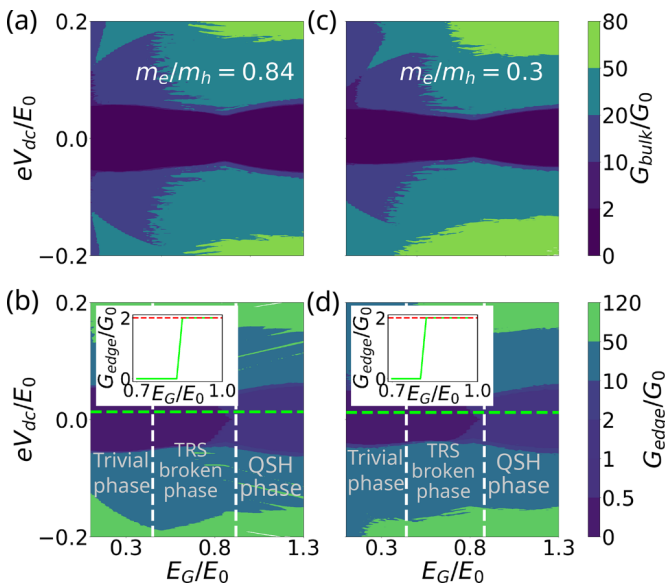


FIG. 6.  $G_{\text{bulk}}$  and  $G_{\text{edge}}$  for the Corbino geometry shown in Fig. 5 as a function of  $E_G$  and  $V_{\text{dc}}$  calculated for different values of mass asymmetry: (a), (b)  $m_e/m_h = 0.84$  and (c), (d)  $m_e/m_h = 0.30$ . The insets show  $G_{\text{edge}}$  as a function of  $E_G$  for small  $eV_{\text{dc}}$  (green line). We have used  $eV_{\text{dc}} = 0.013E_0$  in (b) and  $eV_{\text{dc}} = 0.012E_0$  in (d).

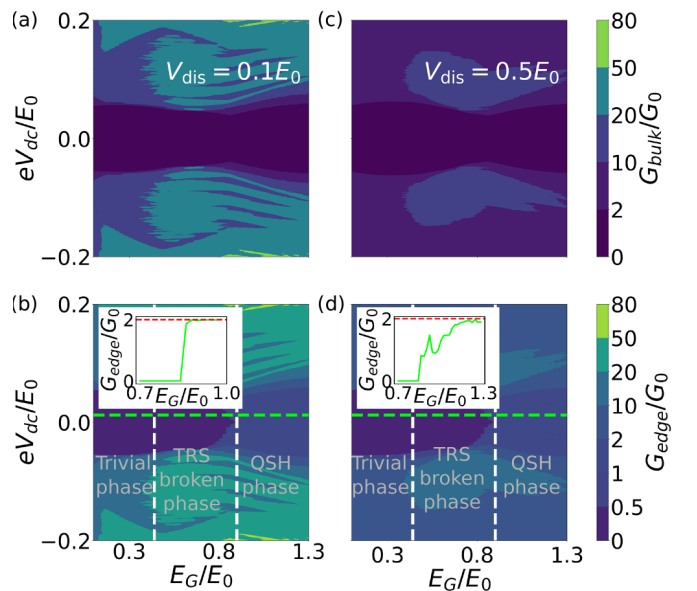


FIG. 7.  $G_{\text{bulk}}$  and  $G_{\text{edge}}$  for the Corbino geometry shown in Fig. 5 as a function of  $E_G$  and  $V_{\text{dc}}$  calculated for different values of the disorder strength: (a), (b)  $V_{\text{dis}} = 0.1E_0$  and (c), (d)  $V_{\text{dis}} = 0.5E_0$ . The insets show  $G_{\text{edge}}$  as a function of  $E_G$  for small  $eV_{\text{dc}}$  (green lines). The conductances have been calculated by taking the average over 20 disorder realizations.

significantly affected by the disorder in both cases. On the other hand, in the case of moderate disorder strength the edge conductance remains practically identical to the clean case,

whereas in the case of strong disorder the interval of  $E_G$  where the conductance increases from 0 to the quantized value is extended.

- 
- [1] M. Z. Hasan and C. L. Kane, Colloquium: Topological insulators, *Rev. Mod. Phys.* **82**, 3045 (2010).
- [2] X.-L. Qi and S.-C. Zhang, Topological insulators and superconductors, *Rev. Mod. Phys.* **83**, 1057 (2011).
- [3] B. A. Bernevig, T. L. Hughes, and S.-C. Zhang, Quantum spin Hall effect and topological phase transition in HgTe quantum wells, *Science* **314**, 1757 (2006).
- [4] C. Liu, T. L. Hughes, X.-L. Qi, K. Wang, and S.-C. Zhang, Quantum Spin Hall Effect in Inverted Type-II Semiconductors, *Phys. Rev. Lett.* **100**, 236601 (2008).
- [5] M. König, S. Wiedmann, C. Brüne, A. Roth, H. Buhmann, L. W. Molenkamp, X.-L. Qi, and S.-C. Zhang, Quantum spin Hall insulator state in HgTe quantum wells, *Science* **318**, 766 (2007).
- [6] I. Knez, R.-R. Du, and G. Sullivan, Evidence for Helical Edge Modes in Inverted InAs/GaSb Quantum Wells, *Phys. Rev. Lett.* **107**, 136603 (2011).
- [7] L. Du, I. Knez, G. Sullivan, and R.-R. Du, Robust Helical Edge Transport in Gated InAs/GaSb Bilayers, *Phys. Rev. Lett.* **114**, 096802 (2015).
- [8] S. Wu, V. Fatemi, Q. D. Gibson, K. Watanabe, T. Taniguchi, R. J. Cava, and P. Jarillo-Herrero, Observation of the quantum spin Hall effect up to 100 kelvin in a monolayer crystal, *Science* **359**, 76 (2018).
- [9] Y. Lozovik and V. Yudson, New mechanism for superconductivity: Pairing between spatially separated electrons and holes, *Sov. Phys. JETP* **44**, 389 (1976).
- [10] Y. Naveh and B. Laikhtman, Excitonic Instability and Electric-Field-Induced Phase Transition Towards a Two-Dimensional Exciton Condensate, *Phys. Rev. Lett.* **77**, 900 (1996).
- [11] D. I. Pikulin and T. Hyart, Interplay of Exciton Condensation and the Quantum Spin Hall Effect in InAs/GaSb Bilayers, *Phys. Rev. Lett.* **112**, 176403 (2014).
- [12] J. C. Budich, B. Trauzettel, and P. Michetti, Time Reversal Symmetric Topological Exciton Condensate in Bilayer HgTe Quantum Wells, *Phys. Rev. Lett.* **112**, 146405 (2014).
- [13] L.-H. Hu, C.-C. Chen, C.-X. Liu, F.-C. Zhang, and Y. Zhou, Topological charge-density and spin-density waves in InAs/GaSb quantum wells under an in-plane magnetic field, *Phys. Rev. B* **96**, 075130 (2017).
- [14] F. Xue and A. H. MacDonald, Time-Reversal Symmetry-Breaking Nematic Insulators Near Quantum Spin Hall Phase Transitions, *Phys. Rev. Lett.* **120**, 186802 (2018).
- [15] Q. Zhu, M. W.-Y. Tu, Q. Tong, and W. Yao, Gate tuning from exciton superfluid to quantum anomalous Hall in van der Waals heterobilayer, *Sci. Adv.* **5**, eaau6120 (2019).
- [16] D. Varsano, M. Palummo, E. Molinari, and M. Rontani, A monolayer transition-metal dichalcogenide as a topological excitonic insulator, *Nat. Nanotechnol.* **15**, 367 (2020).
- [17] Y. Zeng, F. Xue, and A. H. MacDonald, In-plane magnetic field induced density wave states near quantum spin Hall phase transitions, *Phys. Rev. B* **105**, 125102 (2022).
- [18] L. Du, X. Li, W. Lou, G. Sullivan, K. Chang, J. Kono, and R.-R. Du, Evidence for a topological excitonic insulator in InAs/GaSb bilayers, *Nat. Commun.* **8**, 1971 (2017).
- [19] X. Wu, W. Lou, K. Chang, G. Sullivan, and R.-R. Du, Resistive signature of excitonic coupling in an electron-hole double layer with a middle barrier, *Phys. Rev. B* **99**, 085307 (2019).
- [20] X.-J. Wu, W. Lou, K. Chang, G. Sullivan, A. Ikhlassi, and R.-R. Du, Electrically tuning many-body states in a Coulomb-coupled InAs/InGaSb double layer, *Phys. Rev. B* **100**, 165309 (2019).
- [21] D. Xiao, C.-X. Liu, N. Samarth, and L.-H. Hu, Anomalous Quantum Oscillations of Interacting Electron-Hole Gases in Inverted Type-II InAs/GaSb Quantum Wells, *Phys. Rev. Lett.* **122**, 186802 (2019).
- [22] H. Irie, T. Akiho, F. Couëdo, K. Suzuki, K. Onomitsu, and K. Muraki, Energy gap tuning and gate-controlled topological phase transition in InAs/In<sub>x</sub>Ga<sub>1-x</sub>Sb composite quantum wells, *Phys. Rev. Mater.* **4**, 104201 (2020).
- [23] Y. Jia, P. Wang, C.-L. Chiu, Z. Song, G. Yu, B. Jäck, S. Lei, S. Klemenz, F. A. Cevallos, M. Onyszczak, N. Fishchenko, X. Liu, G. Farahi, F. Xie, Y. Xu, K. Watanabe, T. Taniguchi, B. A. Bernevig, R. J. Cava, L. M. Schoop *et al.*, Evidence for a monolayer excitonic insulator, *Nat. Phys.* **18**, 87 (2022).
- [24] B. Sun, W. Zhao, T. Palomaki, Z. Fei, E. Runburg, P. Malinowski, X. Huang, J. Cenker, Y.-T. Cui, J.-H. Chu, X. Xu, S. S. Ataei, D. Varsano, M. Palummo, E. Molinari, M. Rontani, and D. H. Cobden, Evidence for equilibrium exciton condensation in monolayer WTe<sub>2</sub>, *Nat. Phys.* **18**, 94 (2022).
- [25] F. Qu, A. J. A. Beukman, S. Nadj-Perge, M. Wimmer, B.-M. Nguyen, W. Yi, J. Thorp, M. Sokolich, A. A. Kiselev, M. J. Manfra, C. M. Marcus, and L. P. Kouwenhoven, Electric and Magnetic Tuning Between the Trivial and Topological Phases in InAs/GaSb Double Quantum Wells, *Phys. Rev. Lett.* **115**, 036803 (2015).
- [26] I. Knez, C. T. Rettner, S.-H. Yang, S. S. P. Parkin, L. Du, R.-R. Du, and G. Sullivan, Observation of Edge Transport in the Disordered Regime of Topologically Insulating InAs/GaSb Quantum Wells, *Phys. Rev. Lett.* **112**, 026602 (2014).
- [27] E. M. Spanton, K. C. Nowack, L. Du, G. Sullivan, R.-R. Du, and K. A. Moler, Images of Edge Current in InAs/GaSb Quantum Wells, *Phys. Rev. Lett.* **113**, 026804 (2014).
- [28] T. Li, P. Wang, H. Fu, L. Du, K. A. Schreiber, X. Mu, X. Liu, G. Sullivan, G. A. Csáthy, X. Lin, and R.-R. Du, Observation of a Helical Luttinger Liquid in InAs/GaSb Quantum Spin Hall Edges, *Phys. Rev. Lett.* **115**, 136804 (2015).
- [29] B.-M. Nguyen, A. A. Kiselev, R. Noah, W. Yi, F. Qu, A. J. A. Beukman, F. K. de Vries, J. van Veen, S. Nadj-Perge, L. P. Kouwenhoven, M. Kjaergaard, H. J. Suominen, F. Nichele, C. M. Marcus, M. J. Manfra, and M. Sokolich, Decoupling Edge Versus Bulk Conductance in the Trivial Regime of an InAs/GaSb Double Quantum Well using Corbino Ring Geometry, *Phys. Rev. Lett.* **117**, 077701 (2016).
- [30] C. Liu and S. Zhang, Models and materials for topological insulators, in *Topological Insulators*, edited by M. Franz and L. Molenkamp, Contemporary Concepts of Condensed Matter Science, Vol. 6 (Elsevier, 2013), Chap. 3, pp. 59–89.

- [31] X. Zhu, P. B. Littlewood, M. S. Hybertsen, and T. M. Rice, Exciton Condensate in Semiconductor Quantum Well Structures, *Phys. Rev. Lett.* **74**, 1633 (1995).
- [32] C. W. Groth, M. Wimmer, A. R. Akhmerov, and X. Waintal, Kwant: A software package for quantum transport, *New J. Phys.* **16**, 063065 (2014).
- [33] F. Nichele, H. J. Suominen, M. Kjaergaard, C. M. Marcus, E. Sajadi, J. A. Folk, F. Qu, A. J. A. Beukman, F. K. de Vries, J. van Veen, S. Nadj-Perge, L. P. Kouwenhoven, B.-M. Nguyen, A. A. Kiselev, W. Yi, M. Sokolich, M. J. Manfra, E. M. Spanton, and K. A. Moler, Edge transport in the trivial phase of InAs/GaSb, *New J. Phys.* **18**, 083005 (2016).
- [34] N. M. Nguyen, G. Cuono, R. Islam, C. Autieri, T. Hyart, and W. Brzezicki, Unprotected edge modes in quantum spin Hall insulator candidate materials, [arXiv:2209.06912](https://arxiv.org/abs/2209.06912).
- [35] D. A. Bagrets, I. V. Gornyi, and D. G. Polyakov, Nonequilibrium kinetics of a disordered Luttinger liquid, *Phys. Rev. B* **80**, 113403 (2009).
- [36] J. I. Väyrynen, M. Goldstein, Y. Gefen, and L. I. Glazman, Resistance of helical edges formed in a semiconductor heterostructure, *Phys. Rev. B* **90**, 115309 (2014).
- [37] R. Skolasinski, D. I. Pikulin, J. Alicea, and M. Wimmer, Robust helical edge transport in quantum spin Hall quantum wells, *Phys. Rev. B* **98**, 201404(R) (2018).
- [38] C.-A. Li, S.-B. Zhang, and S.-Q. Shen, Hidden edge Dirac point and robust quantum edge transport in InAs/GaSb quantum wells, *Phys. Rev. B* **97**, 045420 (2018).
- [39] Y. Tanaka, A. Furusaki, and K. A. Matveev, Conductance of a Helical Edge Liquid Coupled to a Magnetic Impurity, *Phys. Rev. Lett.* **106**, 236402 (2011).
- [40] J. C. Budich, F. Dolcini, P. Recher, and B. Trauzettel, Phonon-Induced Backscattering in Helical Edge States, *Phys. Rev. Lett.* **108**, 086602 (2012).
- [41] A. M. Lunde and G. Platero, Helical edge states coupled to a spin bath: Current-induced magnetization, *Phys. Rev. B* **86**, 035112 (2012).
- [42] A. Del Maestro, T. Hyart, and B. Rosenow, Backscattering between helical edge states via dynamic nuclear polarization, *Phys. Rev. B* **87**, 165440 (2013).
- [43] G. Dolcetto, M. Sassetti, and T. L. Schmidt, Edge physics in two-dimensional topological insulators, *Riv. Nuovo Cimento* **39**, 113 (2016).
- [44] U. Sivan, P. M. Solomon, and H. Shtrikman, Coupled Electron-Hole Transport, *Phys. Rev. Lett.* **68**, 1196 (1992).
- [45] B. E. Kane, J. P. Eisenstein, W. Wegscheider, L. N. Pfeiffer, and K. W. West, Separately contacted electron-hole double layer in a GaAs/Al<sub>x</sub>Ga<sub>1-x</sub>As heterostructure, *Appl. Phys. Lett.* **65**, 3266 (1994).
- [46] S. Shapira, E. H. Linfield, and M. Pepper, A simple lateral transport device of strongly interacting electron and hole layers, *Appl. Phys. Lett.* **74**, 1603 (1999).
- [47] M. Pohl, M. Lynass, J. G. S. Lok, W. Dietsche, K. v. Klitzing, K. Eberl, and R. Mühle, Closely spaced and separately contacted two-dimensional electron and hole gases by in situ focused-ion implantation, *Appl. Phys. Lett.* **80**, 2105 (2002).
- [48] J. A. Seamons, D. R. Tibbetts, J. L. Reno, and M. P. Lilly, Undoped electron-hole bilayers in a GaAs/AlGaAs double quantum well, *Appl. Phys. Lett.* **90**, 052103 (2007).
- [49] I. B. Spielman, J. P. Eisenstein, L. N. Pfeiffer, and K. W. West, Resonantly Enhanced Tunneling in a Double Layer Quantum Hall Ferromagnet, *Phys. Rev. Lett.* **84**, 5808 (2000).
- [50] I. B. Spielman, J. P. Eisenstein, L. N. Pfeiffer, and K. W. West, Observation of a Linearly Dispersing Collective Mode in a Quantum Hall Ferromagnet, *Phys. Rev. Lett.* **87**, 036803 (2001).
- [51] Y. Yoon, L. Tiemann, S. Schmult, W. Dietsche, K. von Klitzing, and W. Wegscheider, Interlayer Tunneling in Counterflow Experiments on the Excitonic Condensate in Quantum Hall Bilayers, *Phys. Rev. Lett.* **104**, 116802 (2010).
- [52] T. Hyart and B. Rosenow, Quantitative description of Josephson-like tunneling in  $\nu_T = 1$  quantum Hall bilayers, *Phys. Rev. B* **83**, 155315 (2011).
- [53] A. D. K. Finck, J. P. Eisenstein, L. N. Pfeiffer, and K. W. West, Exciton Transport and Andreev Reflection in a Bilayer Quantum Hall System, *Phys. Rev. Lett.* **106**, 236807 (2011).
- [54] X. Huang, W. Dietsche, M. Hauser, and K. von Klitzing, Coupling of Josephson Currents in Quantum Hall Bilayers, *Phys. Rev. Lett.* **109**, 156802 (2012).
- [55] A. Perali, D. Neilson, and A. R. Hamilton, High-Temperature Superfluidity in Double-Bilayer Graphene, *Phys. Rev. Lett.* **110**, 146803 (2013).
- [56] G. W. Burg, N. Prasad, K. Kim, T. Taniguchi, K. Watanabe, A. H. MacDonald, L. F. Register, and E. Tutuc, Strongly Enhanced Tunneling at Total Charge Neutrality in Double-Bilayer Graphene-WSe<sub>2</sub> Heterostructures, *Phys. Rev. Lett.* **120**, 177702 (2018).
- [57] D. K. Efimkin, G. W. Burg, E. Tutuc, and A. H. MacDonald, Tunneling and fluctuating electron-hole Cooper pairs in double bilayer graphene, *Phys. Rev. B* **101**, 035413 (2020).
- [58] T. Paul, V. Fernández Becerra, and T. Hyart, Interplay of quantum spin Hall effect and spontaneous time-reversal symmetry breaking in electron-hole bilayers. II. Zero-field topological superconductivity, *Phys. Rev. B* **106**, 235421 (2022).
- [59] C. W. Groth, M. Wimmer, A. R. Akhmerov, J. Tworzydło, and C. W. J. Beenakker, Theory of the Topological Anderson Insulator, *Phys. Rev. Lett.* **103**, 196805 (2009).
- [60] D. I. Pikulin, T. Hyart, S. Mi, J. Tworzydło, M. Wimmer, and C. W. J. Beenakker, Disorder and magnetic-field-induced breakdown of helical edge conduction in an inverted electron-hole bilayer, *Phys. Rev. B* **89**, 161403(R) (2014).

## **Chapter 5**

**Paper II: Interplay of quantum spin  
Hall effect and spontaneous  
time-reversal symmetry breaking in  
electron-hole bilayers II. Zero-field  
Topological Superconductivity**

## Summary

It has been theoretically proposed that by applying a magnetic field or using ferromagnetic insulators to break TRS in quantum spin Hall insulators in proximity with s-wave superconductors, Majorana zero modes could be realized. The breaking of TRS is necessary to lift the Kramer's degeneracy and obtain well localized Majorana zero modes (MZMs). So far, there has been no successful observation of MZMs from the proposed setup. This is mainly because magnetic field has a detrimental effect on superconductivity and there exists a lack of suitable ferromagnetic insulator materials that can be interfaced with quantum spin Hall insulators. In the paper below, we show that MZMs appear at the interface of an electron-hole bilayer in its TRS broken phase and a superconductor. We calculate a  $\mathbb{Z}_2$  topological invariant  $\nu$  that indicates the parity of the ground state, where the odd (even) value indicates if the system is in topological (trivial) phase. We developed an effective edge theory and analytically show the presence of MZMs at the interface of TRS broken insulator and superconductor. We also propose an experimental setup of superconductor/TRS broken insulator/superconductor Josephson junction, that allows the measurement of the  $4\pi$  periodic Josephson current, which is one of the experimental signatures of the presence of MZMs. We present an in depth study to find the optimal region of parametric values where the MZMs are experimentally visible. Moreover, a mechanism to demonstrate Majorana fusion-rule is also introduced.

## Interplay of quantum spin Hall effect and spontaneous time-reversal symmetry breaking in electron-hole bilayers. II. Zero-field topological superconductivity

Tania Paul <sup>1</sup>, V. Fernández Becerra,<sup>1</sup> and Timo Hyart <sup>1,2,3</sup>

<sup>1</sup>*International Research Centre MagTop, Institute of Physics, Polish Academy of Sciences, Aleja Lotników 32/46, PL-02668 Warsaw, Poland*

<sup>2</sup>*Department of Applied Physics, Aalto University, 00076 Aalto, Espoo, Finland*

<sup>3</sup>*Computational Physics Laboratory, Physics Unit, Faculty of Engineering and Natural Sciences, Tampere University, FI-33014 Tampere, Finland*



(Received 3 June 2022; revised 3 December 2022; accepted 12 December 2022; published 20 December 2022)

It has been proposed that band-inverted electron-hole bilayers support a phase transition from an insulating phase with spontaneously broken time-reversal symmetry to a quantum spin Hall insulator phase as a function of increasing electron and hole densities. Here we show that in the presence of proximity-induced superconductivity, it is possible to realize Majorana zero modes in the time-reversal symmetry broken phase in the absence of magnetic field. We develop an effective low-energy theory for the system in the presence of a time-reversal symmetry-breaking order parameter to obtain analytically the Majorana zero modes and we find good agreement between the numerical and analytical results in the limit of weakly broken time-reversal symmetry. We show that the Majorana zero modes can be detected in superconductor/time-reversal symmetry broken insulator/superconductor Josephson junctions through the measurement of a  $4\pi$  Josephson current. Finally, we demonstrate that the Majorana fusion-rule detection is feasible by utilizing the gate voltage dependence of the spontaneous time-reversal symmetry breaking order parameter.

DOI: [10.1103/PhysRevB.106.235421](https://doi.org/10.1103/PhysRevB.106.235421)

### I. INTRODUCTION

One of the hallmarks of topological insulators is the spin-momentum locking of the surface states [1–8], which in the presence of induced superconductivity facilitates the realization of Majorana zero modes (MZMs) [9–11]. The special property of these quasiparticles, following from their identical creation and annihilation operators, is that they obey non-Abelian braiding statistics [12–14], which could be utilized in topological quantum computing [15,16]. In one of the theoretically most elegant setups, the MZM appears at the interface between regions where the helical edge modes of a quantum spin Hall (QSH) insulator are gapped by the proximity effects from a superconductor and a ferromagnetic insulator, respectively [10–14]. From the theoretical perspective, the topologically robust single-mode propagation in each direction along the edge makes these systems ideal for the observation of transport signatures of MZMs, such as the zero-bias conductance peak due to resonant Andreev reflection [17,18] and the  $4\pi$  Josephson effect [10,19,20].

Experimentally, unambiguous observation of MZMs in QSH insulators is still missing even though signatures of edge mode superconductivity [21,22], Andreev reflection [23], and  $4\pi$  Josephson effect [24] have been observed in these systems. One of the problems is that the creation of hybrid structures of QSH insulators and ferromagnetic insulators has been quite challenging despite recent progress in manufacturing hybrid nanowire-ferromagnetic insulator devices [25]. Moreover, although the gap can also be opened by applying sufficiently

large external magnetic field instead of the utilization of the ferromagnetic insulator, this has detrimental effects on the quality of the superconductors, and therefore this approach is expected to lead to similar difficulties which have so far prevented the unambiguous observation of the MZMs in the nanowire devices.

In this paper, we demonstrate that neither the ferromagnetic insulator nor the external magnetic field is needed for the realization of the MZMs. Our approach is based on previous theoretical work, where it was shown that band-inverted electron-hole bilayers support an unconventional topological phase transition from the trivial to the QSH insulator phase via an intermediate insulating phase with spontaneously broken time-reversal symmetry (TRS), arising from the excitonic correlations between the electrons and holes [26]. This exotic TRS broken phase is one of the most prominent candidates for the correlated phases appearing in band-inverted semiconductors due to Coulomb interactions [26–33], and it is consistent with the accumulating experimental evidence of excitonic phenomenology reported in InAs/GaSb quantum wells [34–38] as well as in WTe<sub>2</sub> [39,40]. Moreover, the properties of the TRS broken phase provide a comprehensive explanation [41] of the temperature, voltage, and length dependencies of the observed conductance in InAs/GaSb bilayers [7,42–44].

We show that MZM appears at the interface between the regions where the helical edge modes are gapped by the TRS breaking order parameter and proximity-induced superconductivity, respectively. Because the TRS is intrinsically

broken in this system, the MZMs can be realized in the absence of magnetic field and ferromagnetic insulators. We study the Josephson effect in superconductor/TRS broken insulator/superconductor junctions and conclude, by checking that all necessary conditions are satisfied [24,45], that the MZMs in this system can be detected through the measurement of the  $4\pi$  Josephson effect. We compare various device geometries and vary the tunable parameters of the system to find the optimal conditions for the observation of the  $4\pi$  Josephson effect. Finally, building on the previous proposals for the manipulation of MZMs [46–49], we demonstrate that the Majorana fusion-rule detection is also feasible in this system by utilizing the gate voltage dependence of the spontaneous TRS breaking order parameter.

## II. PHASE DIAGRAM FOR ZERO-FIELD TOPOLOGICAL SUPERCONDUCTIVITY

Our starting point is the minimal model for band-inverted electron-hole bilayers [5,26,41,50],

$$H_0 = \left( \frac{\hbar^2 k^2}{2m} - E_G \right) \tau_z \sigma_0 + A k_x \tau_x \sigma_z - A k_y \tau_y \sigma_0 + \Delta_z \tau_y \sigma_y, \quad (1)$$

where  $\tau$ 's and  $\sigma$ 's denote the Pauli matrices in the electron-hole and spin basis, the band-inversion parameter  $E_G$  is defined so for  $E_G > 0$  ( $E_G < 0$ ) the electron and hole bands are (not) inverted at the  $\Gamma$  point,  $A$  describes the tunneling between layers,  $m$  is the effective mass, and  $\Delta_z$  is a spin-orbit coupling term arising due to bulk inversion asymmetry. We have ignored the asymmetry of the masses and the momentum-dependent spin-orbit coupling terms, because they are not essential for understanding the phase diagram of the InAs/GaSb bilayers [26,41]. The main effect of Coulomb interactions is the binding of the electrons and holes into excitons with the characteristic size  $d_0$  and binding energy  $E_0$  determined by the relation  $E_0 = \hbar^2/(md_0^2) = e^2/(4\pi\epsilon\epsilon_0 d_0)$ . This leads to an excitonic mean field [26,41]

$$H_{\text{EC}} = \text{Re}[\Delta_1] \tau_x \sigma_y + \text{Re}[\Delta_2] [k_x \tau_x \sigma_z - k_y \tau_y \sigma_0] + \text{Im}[\Delta_1] \tau_x \sigma_y - \text{Im}[\Delta_2] [k_x \tau_y \sigma_z + k_y \tau_x \sigma_0], \quad (2)$$

where the gap equations for the  $s$ -wave and  $p$ -wave excitonic correlations  $\Delta_1$  and  $\Delta_2$  are [41]

$$\begin{aligned} \Delta_1 &= \frac{g_s d_0^2}{(2\pi)^2} \int d^2 k [\langle c_{\mathbf{k}\downarrow 2}^\dagger c_{\mathbf{k}\uparrow 1} \rangle - \langle c_{\mathbf{k}\uparrow 2}^\dagger c_{\mathbf{k}\downarrow 1} \rangle], \\ \Delta_2 &= \frac{g_p d_0^4}{(2\pi)^2} \int d^2 k [-\langle c_{\mathbf{k}\uparrow 2}^\dagger c_{\mathbf{k}\uparrow 1} \rangle (k_x - ik_y) \\ &\quad + \langle c_{\mathbf{k}\downarrow 2}^\dagger c_{\mathbf{k}\downarrow 1} \rangle (k_x + ik_y)]. \end{aligned} \quad (3)$$

Here  $g_s$  ( $g_p$ ) is the effective interaction strength for  $s$ -wave ( $p$ -wave) pairing and  $c_{1\sigma k}$  ( $c_{2\sigma k}$ ) is the electron annihilation operator with spin  $\sigma$  and momentum  $k$  in electron (hole) layer. In our calculations, the integration is performed over the range  $|\mathbf{k}| \leq 2.26/d_0$ , but the exact values of the integration limits are not important.

The values of the model parameters for InAs/GaSb can be estimated by combining theoretical calculations [5,26,27,50] and the experimentally observed energy gaps [7,34]. This

way, we arrive at parameter values [41]:  $E_0/k_B = 200$  K,  $d_0 = 10$  nm,  $A/(E_0 d_0) = 0.06$ ,  $\Delta_z/E_0 = 0.02$ ,  $g_s/E_0 = 1.0$  and  $g_p/E_0 = 0.2$ . The gate-voltage dependent parameter  $E_G$  is varied in our calculations to tune the system from a trivial insulator to QSH insulator phase. For small (large) values of  $E_G$ , the system is in a trivial (QSH) insulator phase, and these two phases are separated from each other by an insulating phase with spontaneously broken TRS, where  $\text{Im}[\Delta_1], \text{Im}[\Delta_2] \neq 0$  [26,41]. The bulk gap  $\Delta_{\text{bulk}}$  remains open for all values of  $E_G$  because the intermediate TRS broken phase enables the connection of the topologically distinct phases without bulk gap closing. The edge gap  $\Delta_{\text{edge}}$  decreases monotonously when one starts from the trivial phase and tunes the system across the TRS broken phase to the QSH phase, where the gapless edge excitations are protected by the topology [26,41].

Here we consider the properties of the system in the presence of proximity-induced superconductivity in certain regions of the sample. The Bogoliubov–de Gennes Hamiltonian in the Nambu basis  $\Psi = (c_{\mathbf{k}\uparrow}, c_{\mathbf{k}\downarrow}, c_{-\mathbf{k}\downarrow}^\dagger, -c_{-\mathbf{k}\uparrow}^\dagger)$  can be written compactly as

$$H_{\text{BdG}}(\mathbf{k}, \mathbf{x}) = \begin{pmatrix} H(\mathbf{k}, \mathbf{x}) & \Delta_s(\mathbf{x}) \\ \Delta_s^*(\mathbf{x}) & -\sigma_y H^T(-\mathbf{k}, \mathbf{x}) \sigma_y \end{pmatrix}, \quad (4)$$

where  $H(\mathbf{k}, \mathbf{x}) = H_0(\mathbf{k}, \mathbf{x}) + H_{\text{EC}}(\mathbf{k}, \mathbf{x})$ . The induced superconductivity has two effects in the regions proximitized by the superconductor. First, it leads to induced superconducting gap  $|\Delta_s(\mathbf{x})| = \Delta_0 \neq 0$  in the regions of  $\mathbf{x}$  covered by the superconductor. Second, it affects the parameters of the normal state Hamiltonian  $H(\mathbf{k}, \mathbf{x})$ . We assume that the superconductor completely screens the Coulomb interactions and renormalizes the band-inversion parameter, so  $H_{\text{EC}}(\mathbf{k}, \mathbf{x}) = 0$  and  $E_G(x) = E_G^S$  in the regions of  $\mathbf{x}$  covered by superconductors. In the normal regions, the spatially dependent parameters have values  $|\Delta_s(\mathbf{x})| = 0$ ,  $E_G(x) = E_G^N$  and  $H_{\text{EC}}(\mathbf{k}, \mathbf{x})$  is determined by Eqs. (2) and (3).

We start by investigating the edge excitations in the presence of induced superconductivity and TRS breaking order parameter. For this purpose, we utilize a low-energy theory (valid at energies much smaller than the bulk gap  $|E| \ll \Delta_{\text{bulk}}$ ),

$$H_e = \begin{pmatrix} A_{\text{eff}}(x) k_x & -i\Delta_{\text{ex}}(x) & \Delta_s(x) & 0 \\ i\Delta_{\text{ex}}(x) & -A_{\text{eff}}(x) k_x & 0 & \Delta_s(x) \\ \Delta_s^*(x) & 0 & -A_{\text{eff}}(x) k_x & -i\Delta_{\text{ex}}(x) \\ 0 & \Delta_s^*(x) & i\Delta_{\text{ex}}(x) & A_{\text{eff}}(x) k_x \end{pmatrix}, \quad (5)$$

where  $A_{\text{eff}}(x)$  is the velocity of the helical edge states,  $\Delta_{\text{ex}}(x)$  is the TRS breaking order parameter in the normal regions of  $x$ , and  $\Delta_s(x) = \Delta_0(x) e^{i\varphi(x)}$  is the induced superconducting pairing potential in the regions of  $x$  covered by the superconductors. If the TRS broken insulator (superconductor) covers the region  $x < 0$  ( $x > 0$ ), there is a MZM localized at  $x = 0$  (see Fig. 1), namely, there exists a zero-energy solution of the

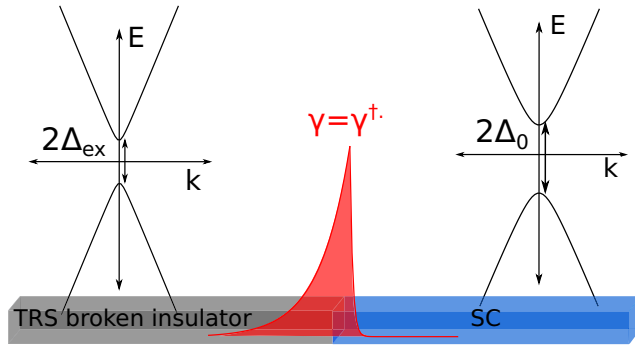


FIG. 1. Schematic illustration of MZM  $\gamma = \gamma^\dagger$  localized at the interface between regions, where the helical edge modes are gapped by the TRS breaking order parameter  $\Delta_{\text{ex}}$  and proximity-induced superconducting pairing amplitude  $\Delta_0$ .

Hamiltonian Eq. (5) of the form (see Appendix A)

$$\psi(x) = \begin{cases} \frac{1}{\mathcal{N}} \begin{pmatrix} -e^{-i\pi/4} e^{i\varphi/2} \\ e^{-i\pi/4} e^{i\varphi/2} \\ e^{i\pi/4} e^{-i\varphi/2} \\ e^{i\pi/4} e^{-i\varphi/2} \end{pmatrix} e^{\Delta_{\text{ex}}x/A_{\text{eff}}^N}, & x < 0 \\ \frac{1}{\mathcal{N}} \begin{pmatrix} -e^{-i\pi/4} e^{i\varphi/2} \\ e^{-i\pi/4} e^{i\varphi/2} \\ e^{i\pi/4} e^{-i\varphi/2} \\ e^{i\pi/4} e^{-i\varphi/2} \end{pmatrix} e^{-\Delta_0x/A_{\text{eff}}^S}, & x > 0, \end{cases} \quad (6)$$

where we can approximate  $A_{\text{eff}}^N = A + |\Delta_2|$ ,  $A_{\text{eff}}^S = A$  and  $\Delta_{\text{ex}} = \sqrt{\text{Im}[\Delta_1]^2 + \text{Im}[\Delta_2]^2}$ . The corresponding field operator  $\gamma$  in the second quantized form obeys  $\gamma = \gamma^\dagger$ , and by choosing the normalization constant  $\mathcal{N}$  properly, we obtain  $\gamma^2 = 1$ . Therefore, this solution satisfies the algebra of the MZMs. The appearance of the MZM in this system is mathematically analogous to the case of QSH insulator-ferromagnetic insulator-superconductor hybrid systems [10], but the important difference is that here the ferromagnetic insulator is not needed because the spontaneous TRS breaking leads to opening of an energy gap in the edge state spectrum.

We can also study the appearance of the MZM beyond the limits of validity of the effective edge theory using the full two-dimensional Hamiltonian Eq. (4). For this purpose, we consider a sample with region  $-L_y/2 \leq y \leq 0$  in the normal state and region  $0 \leq y \leq L_y/2$  covered by a superconductor [see Fig. 2(a)]. Such kind of system supports a  $\mathbb{Z}_2$  topological invariant [19],

$$\nu = \text{sgn}[\text{Pf}M(0)\text{Pf}M(\pi)], \quad M(k_x) = \tau_y \sigma_y H_{\text{BdG}}(k_x), \quad (7)$$

where the Pfaffians of the antisymmetric matrices  $M(k_x = 0, \pi)$  are real. The topologically nontrivial (trivial) gapped phases with  $\nu = -1$  ( $\nu = 1$ ) have odd (even) ground-state parity and they do (do not) support unpaired MZMs at the end of the system, which for the geometry shown in Fig. 2(a) corresponds to the interface of the normal and superconducting regions along the edge [see Fig. 2(b)]. Additionally, the system can also support gapless phases.

We have numerically calculated the topological invariant  $\nu$  as a function of  $E_G^S$  and  $E_G^N$  using the algorithm developed in Ref. [51] [see Fig. 2(c)]. For small values of  $E_G^N$ , the normal

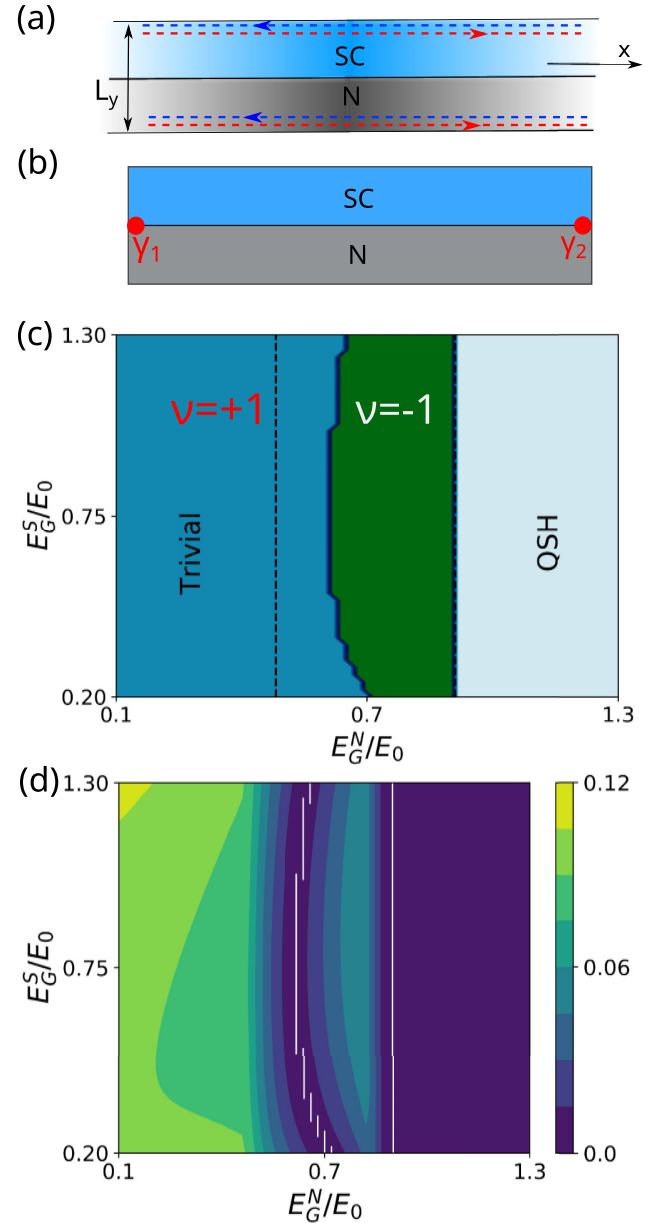


FIG. 2. (a)  $\mathbb{Z}_2$  topological invariant  $\nu$ , Eq. (7), is computed for a wide sample  $L_y \gg d_0$  with upper half covered by the superconductor (SC) and lower half in the normal state (N). The dashed lines illustrate the edge states when the effective edge theory is valid. (b) When a boundary is introduced in the  $x$  direction, MZMs  $\gamma_1$  and  $\gamma_2$  appear at the interface of the SC and N regions along the edge if the system is in the topologically nontrivial phase with  $\nu = -1$ . (c) Topological phase diagram as a function of  $E_G^S$  and  $E_G^N$ . In the dark blue trivial phase,  $\nu = 1$  and the hybrid system does not support MZMs. In the green topologically nontrivial phase,  $\nu = -1$  and the system supports MZMs at the interface of the TRS broken insulator and superconducting regions. The dashed lines indicate the values of  $E_G^N$ , where the normal half of the system has transitions from the TRS broken insulator phase to trivial insulator and QSH insulator phases. (d) Energy gap as a function of  $E_G^S/E_0$  and  $E_G^N/E_0$ . The white lines indicate the phase boundaries where the topological invariant  $\nu$  changes from 1 to  $-1$  and the energy gap closes. Here we have used  $L_y = 250d_0$  and  $\Delta_0 = 0.1E_0$ .

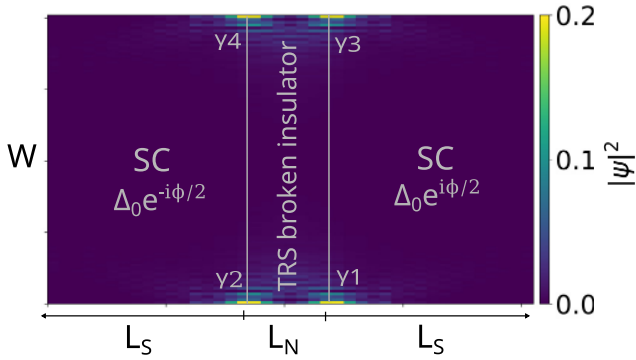


FIG. 3. Superconductor/TRS broken insulator/superconductor Josephson junction for detection of the MZMs via the  $4\pi$  Josephson effect. The system supports two MZMs  $\gamma_1$  and  $\gamma_2$  ( $\gamma_3$  and  $\gamma_4$ ) on the bottom (top) edge with the corresponding low-energy local density of states indicated with the colors. The hybridization of the MZMs across a TRS broken regime of length  $L_N$  gives rise to a  $4\pi$ -periodic component in the Josephson current-phase characteristic  $I(\phi)$ . The width is assumed to be large  $W \gg d_0$  so the parities  $\mathcal{P}_{12} = i\gamma_1\gamma_2$  and  $\mathcal{P}_{34} = i\gamma_3\gamma_4$  within each edge are conserved.

region is in a trivial insulator phase and the hybrid system is also in a topologically trivial phase  $\nu = 1$ . Upon increasing  $E_G^N$ , the normal region enters the TRS broken phase [dashed vertical line around  $E_G^N = 0.48E_0$  in Fig. 2(c)] but at this transition the hybrid system still remains trivial with  $\nu = 1$ . Only by further increasing  $E_G^N$ , we find a separate phase transition of the hybrid system to a topologically nontrivial phase with  $\nu = -1$ , and this transition can be controlled with both  $E_G^N$  and  $E_G^S$  [see Fig. 2(c)]. If we increase  $E_G^N$  further, the normal region finally enters into the QSH phase so the hybrid system becomes gapless and the MZMs leak and delocalize into the QSH insulator region along the edge [see Figs. 2(c) and 2(d)]. We have checked with comprehensive numerical calculations that within the topologically nontrivial phase with  $\nu = -1$ , the system always supports MZMs at the interfaces of the TRS broken insulator and superconductor regions. These results are consistent with our effective edge theory, which is expected to be valid on the QSH side of the TRS broken phase where the edge gap is smaller than the bulk gap, but the numerical approach allows us to establish the phase transition line also on the trivial side of the TRS broken phase.

### III. $4\pi$ JOSEPHSON EFFECT

We now proceed to the consideration of the experimental signatures of the MZMs in superconductor/TRS broken insulator/superconductor Josephson junctions. We first consider the simplest geometry, where two large superconducting leads are connected by a wide  $W \gg d_0$  normal region of length  $L_N$  as shown in Fig. 3. Such a Josephson junction has a qualitatively different spectrum (see Fig. 4) depending on whether the hybrid system is in a  $\nu = 1$ ,  $\nu = -1$ , or QSH part of the phase diagram shown in Fig. 2. In the trivial phase  $\nu = 1$ , there exists only gapped Andreev bound states [Fig. 4(a)], and therefore the application of a phase bias across the superconductors  $\Delta_s(\mathbf{x}) = \Delta_0(e^{i\phi/2}\theta(x - L_n) + e^{-i\phi/2}\theta(-x))$  leads to a conventional  $2\pi$  periodic Josephson effect. In the topo-

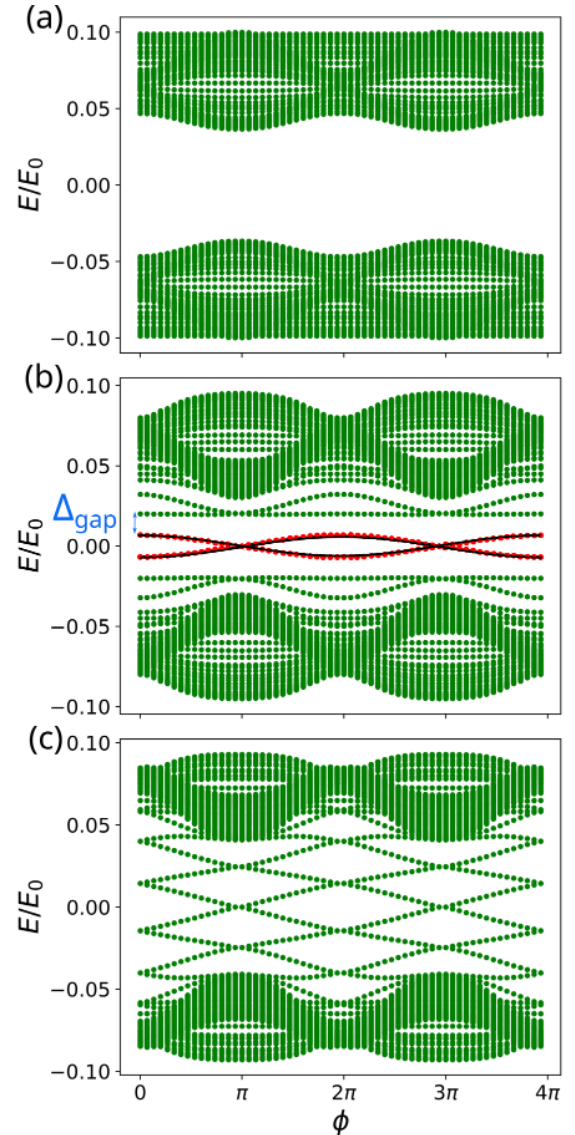


FIG. 4. Spectrum of the Josephson junction (Fig. 3) as a function of the phase bias  $\phi$  when the hybrid system is in (a)  $\nu = 1$  ( $E_G^N = 0.3E_0$ ), (b)  $\nu = -1$  ( $E_G^N = 0.86E_0$ ), and (c) QSH ( $E_G^N = 1.1E_0$ ) part of the phase diagram in Fig. 2. (a) All the Andreev bound states are gapped. (b) The hybridization of MZMs across the TRS-broken regime leads to  $\phi$  dependence of their energies (red lines corresponding to each edge). There exists an energy gap  $\Delta_{\text{gap}}$  between the MZMs and other Andreev levels. (c) In the QSH regime,  $\Delta_{\text{gap}} = 0$ . In all figures, the other parameters are  $E_G^S = 1.3E_0$ ,  $\Delta_0 = 0.1E_0$ ,  $L_N = 10d_0$ ,  $W = 150d_0$ , and  $L_S = 15d_0$ .

logically nontrivial  $\nu = -1$  state, the system supports four MZMs  $\gamma_i$  ( $i = 1, \dots, 4$ ) at the interfaces of the TRS broken insulator and superconducting regions [see Figs. 3 and 4(b)]. Because  $W \gg d_0$ , the coupling between the Majoranas across the width of the sample can be neglected so the parities  $\mathcal{P}_{12} = i\gamma_1\gamma_2$  and  $\mathcal{P}_{34} = i\gamma_3\gamma_4$  within each edge are good quantum numbers, and the application of the phase bias  $\phi$  leads to a Josephson current, which in addition to the conventional  $2\pi$ -periodic component also has parity-dependent  $4\pi$ -periodic

component [10,19,20],

$$I(\phi) = I_{2\pi} \sin(\phi) + I_{4\pi} \frac{\mathcal{P}_{12} + \mathcal{P}_{34}}{2} \sin(\phi/2) + \text{h.h.}, \quad (8)$$

where h.h. denotes the higher harmonics. The magnitude of the  $4\pi$  Josephson effect,

$$I_{4\pi} = \frac{e}{\hbar} \frac{2}{4\pi} \int_0^{4\pi} d\phi \sum_M \frac{dE_M(\phi)}{d\phi} \sin(\phi/2), \quad (9)$$

is determined by the quasiparticle energies  $E_M(\phi)$ , originating from the hybridization of MZMs  $\gamma_1$  and  $\gamma_2$  ( $\gamma_3$  and  $\gamma_4$ ) at bottom (top) edge, which cross  $E = 0$  at  $\phi = \pi$  [doubly degenerate red lines in Fig. 4(b)]. In the asymptotic limit,  $L_N \gg A_{\text{eff}}^N / \Delta_{\text{ex}}$  (see Appendices A and B),

$$I_{4\pi} = 2 \frac{e}{\hbar} \frac{\Delta_0 \Delta_{\text{ex}}}{\Delta_0 + \Delta_{\text{ex}}} e^{-\Delta_{\text{ex}} L_N / A_{\text{eff}}^N}. \quad (10)$$

On the other hand,

$$I_{2\pi} = \frac{e}{\hbar} \frac{2}{2\pi} \int_0^{2\pi} d\phi \sum_k \frac{dE_k(\phi)}{d\phi} \sin \phi \quad (11)$$

includes contributions from all other Andreev levels  $k$  with  $E_k < 0$  except the MZMs. The methods for calculating  $I(\phi)$ , including hybrid kernel polynomial method (KPM) [52], exact diagonalization, and the low-energy effective edge theory, are discussed in Appendix B. In all our calculations, the current is expressed in units of  $I_0 = eE_0/\hbar \approx 4 \mu\text{A}$ . We concentrate only on  $I_{2\pi}$  and  $I_{4\pi}$ , which can be experimentally measured independently from the other harmonics in the Josephson radiation spectrum [24,45]. In this type of experiments, the applied voltage  $V$  across the Josephson junction leads to ac Josephson effect  $\phi(t) = 2eVt/\hbar$ , so  $I_{4\pi}$  ( $I_{2\pi}$ ) results in Josephson radiation at frequency  $f_{4\pi} = eV/h$  ( $f_{2\pi} = 2eV/h$ ). In addition to  $I_{4\pi}$  and  $I_{2\pi}$  the energy gap  $\Delta_{\text{gap}}$  between the MZMs and other Andreev levels is also important for the robustness of the  $4\pi$  Josephson effect. In the presence of TRS breaking order parameter  $\Delta_{\text{gap}} \neq 0$ , whereas in the QSH regime  $\Delta_{\text{gap}} = 0$  [cf. Figs. 4(b) and 4(c)].

Several conditions need to be satisfied so the  $4\pi$  Josephson effect can be robustly detected. (i) It is important that the frequencies are much larger than the quasiparticle poisoning rate and the hybridization of the MZMs localized at the different edges  $f_{4\pi} \gg 1/T_{\text{pois}}, \Delta_{\text{hyb}}/h$ . These do not pose fundamental problems because the hybridization  $\Delta_{\text{hyb}}$  can be made arbitrarily small by increasing the width of the sample  $W$  and the quasiparticle poisoning time  $T_{\text{pois}}$  can be as large as seconds in state-of-the-art superconducting devices in the absence of magnetic field [53–55]. Nevertheless, such kind of quasiparticle poisoning rates only apply to small superconducting islands, so in practice the experiment is expected to be less challenging if the Josephson radiation frequencies are reasonably large. Indeed, based on the earlier experiments [24,45], we expect that the ideal operation regime for probing the  $4\pi$  Josephson effect is achieved by tuning the Josephson frequencies to the gigahertz frequency range with the applied voltage  $V$ . (ii) The energy gap  $\Delta_{\text{gap}}$  between the MZMs and other Andreev bound states should be sufficiently large to avoid Landau-Zener tunneling  $\hbar d\phi/dt = \hbar f_{2\pi} \ll \Delta_{\text{gap}}$  and thermal excitations  $k_B T \ll \Delta_{\text{gap}}$ . Violation of these conditions

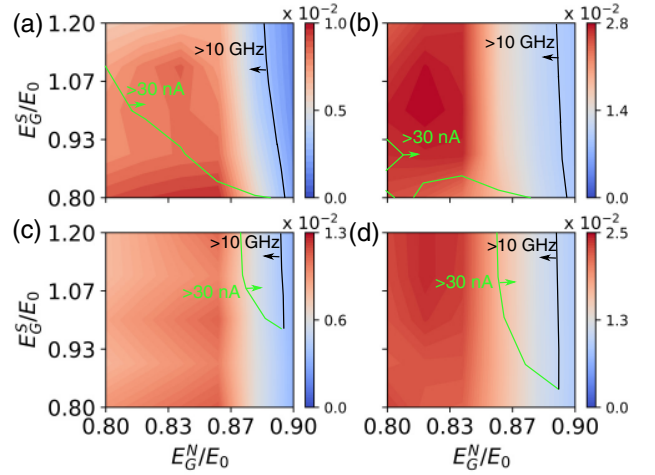


FIG. 5. Energy gap  $\Delta_{\text{gap}}/E_0$  between the MZMs and the other Andreev levels as a function of  $E_G^N/E_0$  and  $E_G^S/E_0$  for (a)  $\Delta_0 = 0.03E_0$  and  $L_N = 5d_0$ , (b)  $\Delta_0 = 0.1E_0$  and  $L_N = 5d_0$ , (c)  $\Delta_0 = 0.03E_0$  and  $L_N = 10d_0$ , and (d)  $\Delta_0 = 0.1E_0$  and  $L_N = 10d_0$ . In all figures,  $L_S = 15d_0$  and  $W = 150d_0$ . The optimal parameter regimes for the observation of the  $4\pi$  Josephson effect is the region between black and green lines. The upper bound of  $E_G^N$  (black line) is determined by the condition that  $\Delta_{\text{gap}}$  is sufficiently large, whereas the lower bounds of  $E_G^N$  and  $E_G^S$  (green line) are determined by the condition that  $I_{4\pi}$  (shown in Fig. 6) is sufficiently large.

gives rise to  $2\pi$ -periodic occupation of the Andreev levels, which suppresses the  $4\pi$  Josephson effect, and the remaining signatures of  $4\pi$  Josephson effect depend on the details of the relaxation processes [20,24,56]. Thus, in the most robust operation conditions,  $\Delta_{\text{gap}}/h > 10 \text{ GHz}$ . (iii) Finally,  $I_{4\pi}$  should be sufficiently large to overcome the detector sensitivity. Based on the earlier experiment [24,45], we estimate that  $I_{4\pi} > 30 \text{ nA}$  would allow robust detection of the  $4\pi$  Josephson effect. Although  $I_{4\pi}$  and  $I_{2\pi}$  give separate peaks in the ideal detection, in practice very large  $I_{2\pi}$  can cause problems due to the broadening of the peaks in the case of imperfect detection of the radiation spectrum.

As discussed in the previous section, the low-energy physics is quite well captured by the effective edge theory. Therefore,  $I_{4\pi}$  and  $\Delta_{\text{gap}}$  can be accurately calculated analytically using Eq. (10) and the approach discussed in Appendix A in a large part of the parameter space  $E_G^N, E_G^S, \Delta_0$ , and  $L_N$  (see Appendix B). On the other hand, we find that there exists a large number of Andreev levels which contribute to  $I_{2\pi}$  because they have a significant dispersion as a function of  $\phi$  (see Fig. 4). Therefore, we utilize the hybrid KPM [52] implemented within KWANT software package [57] for calculation of the  $I_{2\pi}$  (see Appendix B). Our results for  $\Delta_{\text{gap}}, I_{4\pi}$ , and  $I_{2\pi}$  for various different model parameters are shown in Figs. 5–7, respectively. We find that there exists a large region in parameter space where the conditions (ii) and (iii) for the robust detection  $4\pi$  Josephson effect are satisfied (see the optimal parameter regimes indicated in Figs. 5 and 6). However, we also notice that  $I_{2\pi}$  is typically an order of magnitude larger than  $I_{4\pi}$  (cf. Figs. 6 and 7). This is not a problem in the case of an ideal detection because the  $4\pi$  and

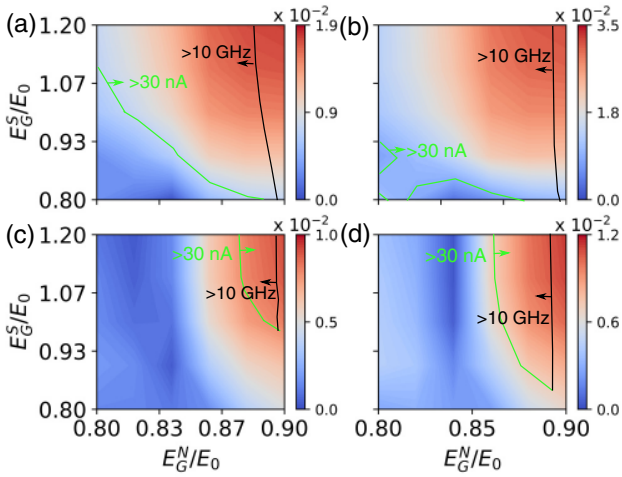


FIG. 6. (a)–(d) Magnitude of the  $4\pi$  Josephson effect  $I_{4\pi}/I_0$  for the same set of model parameters as described in Figs. 5(a)–5(d), respectively. The requirement that  $I_{4\pi}$  is sufficiently large determines the lower bounds of  $E_G^N$  and  $E_G^S$  in the optimal parameter regimes shown in Figs. 5 and 6.

$2\pi$  Josephson effects give rise to peaks at separate frequencies in the Josephson radiation spectrum. However, the large peak caused by  $I_{2\pi}$  may overshadow the peak caused by the  $I_{4\pi}$  due to the broadening of the peaks in the case of imperfect detection of the radiation spectrum. We point out that if this becomes a problem it is possible to significantly reduce  $I_{2\pi}$  by changing the device geometry so the superconducting leads are coupled only to one of the edges of the sample. Moreover,  $I_{2\pi}$  can also be reduced by decreasing the width of the sample  $W$  while still keeping it large enough so coupling between MZMs located at the top and bottom edges remains sufficiently small (see Appendix B).

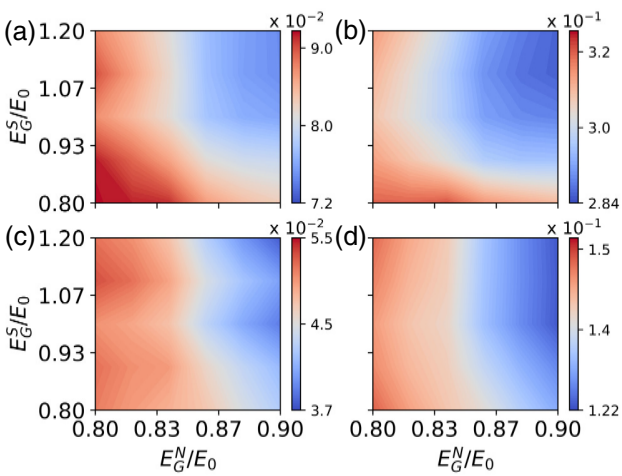


FIG. 7. (a)–(d) Magnitude of the  $2\pi$  Josephson effect  $I_{2\pi}/I_0$  for the same set of model parameters as described in Figs. 5(a)–5(d), respectively.  $I_{2\pi}$  is typically an order of magnitude larger than  $I_{4\pi}$  shown in Figs. 6.

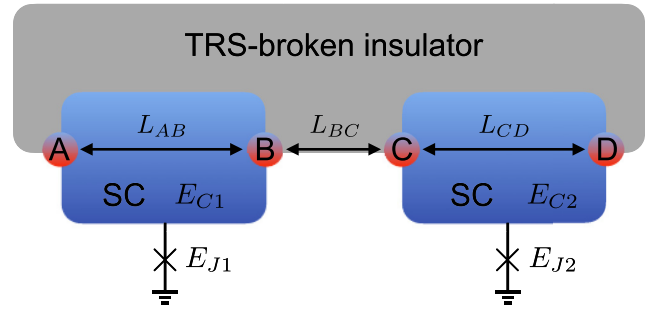


FIG. 8. Setup for detection of fusion rules. The couplings between MZMs can be controlled with the tunable Josephson energies  $E_{J1}$ ,  $E_{J2}$ , and the gate-tunable energy gap  $\Delta_{\text{ex}}$  appearing due to the spontaneous TRS breaking.

#### IV. FUSION-RULE DETECTION

The fusion rules are a fundamental property of non-Abelian anyons describing how they coalesce. Equivalently with the nontrivial braiding statistics, the nontrivial fusion rules also require the existence of the topological ground state degeneracy, and they can be used to define the non-Abelian anyons, but they are much simpler to detect [49], namely, the previously considered setups can be easily generalized for the fusion-rule detection and validation of the topological qubit by introducing tunable Josephson energies  $E_{J1}$  and  $E_{J2}$  of two superconducting islands coupled to a superconducting ground (see Fig. 8), in analogy to the proposal suggested in Ref. [49] for the fusion-rule detection in nanowires. The superconducting islands contain a macroscopic number of electrons but they are sufficiently small so the charging energies of the islands,  $E_{C1}$  and  $E_{C2}$ , exceed temperature. The setup shown in Fig. 8 contains four MZMs, which we denote as  $\gamma_i$  ( $i = A, B, C, D$ ), and they are spatially separated by distances  $L_{AB}$ ,  $L_{BC}$ , and  $L_{CD}$ , respectively. The MZMs satisfy the algebra  $\gamma_i = \gamma_i^\dagger$  and  $\{\gamma_i, \gamma_j\} = 2\delta_{ij}$ , and they can be used to define a topological qubit. Assuming that the total parity is fixed (all operations need to be performed faster than the quasiparticle poisoning time), the MZMs admit two ground states. For even total parity, we can write these two logical states of the topological qubit as

$$|0_{AB}, 0_{CD}\rangle, \quad |1_{AB}, 1_{CD}\rangle, \quad (12)$$

where  $N_{AB}, N_{CD} \in \{0, 1\}$  refer to occupation numbers of ordinary fermions  $f_{AB}^\dagger = (\gamma_A + i\gamma_B)/2$  and  $f_{CD}^\dagger = (\gamma_C + i\gamma_D)/2$ . The measurement of the state in this basis can be performed by coupling (fusing) the MZMs  $\gamma_A$  and  $\gamma_B$  (or  $\gamma_C$  and  $\gamma_D$ ) and then utilizing microwaves, charge sensor, or charge pumping for read-out of the fermion occupation number as described in detail in Refs. [47,49]. The fusion rule of MZMs is

$$\sigma \times \sigma = I + \psi, \quad (13)$$

which states that two MZMs can coalesce into identity  $I$  (occupation number of the fermion corresponding to the pair of MZMs is 0) or a fermion  $\psi$  (occupation number is 1). The simplest manifestation of this fusion rule in our setup is to initialize the system into a state with well-defined occupation numbers of the fermions  $f_{AD}^\dagger = (\gamma_A + i\gamma_D)/2$  and

$f_{BC}^\dagger = (\gamma_B + i\gamma_C)/2$  and to measure the occupation number  $N_{AB}$  (or  $N_{CD}$ ). The probabilities for measuring occupation numbers 0 and 1 are then equal, because (see Appendix C)

$$\begin{aligned} |0_{AD}0_{BC}\rangle &= \frac{1}{\sqrt{2}}(|0_{AB}0_{CD}\rangle + |1_{AB}1_{CD}\rangle), \\ |1_{AD}1_{BC}\rangle &= \frac{i}{\sqrt{2}}(|1_{AB}1_{CD}\rangle - |0_{AB}0_{CD}\rangle). \end{aligned} \quad (14)$$

However, some care is required to make sure the outcome of the measurement can be interpreted as evidence of the Majorana fusion rules. We will describe the necessary protocol for fusion-rule detection [49] and identify the optimal

$$U_{AB(CD)} = \begin{cases} \frac{16}{(2\pi^2)^{1/4}} E_{C1(2)} \left(\frac{E_{J1(2)}}{E_{C1(2)}}\right)^{3/4} e^{-\sqrt{8E_{J1(2)}/E_{C1(2)}}} \cos(\pi q_k/e), & \text{charging - energy dominant} \\ \frac{\Delta_0 \Delta_{\text{ex}}}{\Delta_0 + \Delta_{\text{ex}}} e^{-\Delta_0 L_{AB(CD)}/A_{\text{eff}}^S}, & \text{Majorana - overlap dominant} \end{cases} \quad (16)$$

and

$$U_{BC} = \frac{\Delta_0 \Delta_{\text{ex}}}{\Delta_0 + \Delta_{\text{ex}}} e^{-\Delta_{\text{ex}} L_{BC}/A_{\text{eff}}^N} \cos(\phi/2). \quad (17)$$

Here the offset charge  $q_k$  can be controlled with the help of a voltage applied to a nearby gate electrode, and we have assumed that  $U_{ij} < \Delta_{\text{gap}}$ , so the excitations above the energy gap  $\Delta_{\text{gap}}$  can be neglected. In the fusion-rule detection protocol [49], it is important that each coupling  $U_{ij}$  ( $ij = AB, BC, CD$ ) can be turned on  $U_{ij} = U_{\text{max}}$  and off  $U_{ij} = U_{\text{min}}$ , so  $U_{\text{min}} \ll U_{\text{max}}$ . In the case  $U_{AB(CD)}$ , we assume that  $L_{AB(CD)}$  is sufficiently large so we are always in the charging-energy dominant regime (see conditions below). Thus, these couplings are controlled with  $E_{J1(2)}$ . Importantly,  $U_{AB(CD)}$  depends exponentially on  $E_{J1(2)}$ , so a moderate tuning of the Josephson couplings leads to  $U_{\text{min}} \ll U_{\text{max}}$ . We point out that it is only important to be in the regime  $E_{J1(2)} \gg E_{C1(2)}$  when the couplings are turned off:  $U_{ij} = U_{\text{min}}$ . When the couplings are turned on,  $U_{ij} = U_{\text{max}}$ , the charging energy can even be larger than the Josephson coupling as long as  $U_{\text{max}} < \Delta_{\text{gap}}$  is satisfied. If  $E_{J1(2)} \ll E_{C1(2)}$ , one obtains  $U_{\text{max}} = E_{C1(2)}/2$  [47,49]. Similarly, one also needs to tune  $U_{BC}$  during the fusion protocol. Because of the exponential dependence on  $\Delta_{\text{ex}}$ , the best way to turn  $U_{BC}$  on and off is to control  $\Delta_{\text{ex}}$  with the gate voltages. Also, in this case it is important to be in the asymptotic limit ( $\Delta_{\text{ex}} \gg A_{\text{eff}}^N/L_{BC}$ ) when the coupling is turned off,  $U_{BC} = U_{\text{min}}$ , and it is only important that  $U_{\text{max}} < \Delta_{\text{gap}}$  is satisfied when the coupling is turned on. In the description of the fusion rule detection protocol, we set  $U_{\text{min}} \rightarrow 0$ . In practice, it means that the timescale operations  $T_{\text{op}}$  must satisfy  $T_{\text{op}} \ll \hbar/U_{\text{min}}$ . All the operations should be performed adiabatically with respect to the gap  $T_{\text{op}} \gg \hbar/\Delta_{\text{gap}}$  and the turned-on coupling  $T_{\text{op}} \gg \hbar/U_{\text{max}}$ .

The fusion-rule detection protocol, which is based on the proposal in Ref. [49], is shown in Fig. 9. It consists of a two different sequences of operations called fusion experiment and control experiment. In the basis of logical states of the topological qubit Eqs. (12), the low-energy Hamiltonian

operation regime below. We point out that the detection of the braiding statistics and more complicated manipulations of the MZMs are also possible using our platform, but these operations would require a branched geometry [18,46–49], which is much more challenging to realize experimentally. Thus, we do not consider these possibilities in this paper.

The fusion-rule detection protocol outlined in Ref. [49] requires that the couplings between the MZMs can be varied as a function of time. In the limit  $E_{Jk} \gg E_{Ck}$  ( $k = 1, 2$ ),  $L_{AB}, L_{CD} \gg A_{\text{eff}}^S/\Delta_0$  and  $L_{BC} \gg A_{\text{eff}}^N/\Delta_{\text{ex}}$ , the low-energy Hamiltonian for the MZMs is [18,46–49]

$$H_{\text{eff}} = -iU_{AB}\gamma_A\gamma_B - iU_{BC}\gamma_B\gamma_C - iU_{CD}\gamma_C\gamma_D, \quad (15)$$

where (see Appendix A)

Eq. (15) can be written as

$$H_{\text{eff}} = -(U_{AB} + U_{CD})\sigma_z - U_{BC}\sigma_x, \quad (18)$$

so the eigenenergies and eigenstates of the Hamiltonian Eq. (18) are (we assume  $U_{BC} > 0$  for simplicity)

$$E_{\pm} = \pm\sqrt{(U_{AB} + U_{CD})^2 + U_{BC}^2}, \quad (19)$$

$$\psi_{\pm} = \frac{1}{\sqrt{2}} \left( \sqrt{1 \mp \frac{U_{AB} + U_{CD}}{|E_{\pm}|}}, \mp \sqrt{1 \pm \frac{U_{AB} + U_{CD}}{|E_{\pm}|}} \right)^T. \quad (20)$$

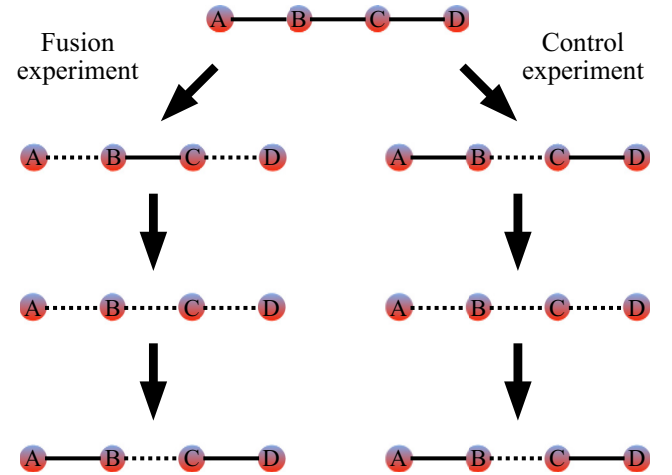


FIG. 9. Protocol for detection of fusion rules. The solid (dashed) lines indicate couplings  $U_{ij}$  between the MZMs  $\gamma_i$  and  $\gamma_j$ , which are turned on (off). In the final state, the occupation numbers  $[N_{AB}, N_{CD}]$  are measured. In the fusion experiment, the sequence of the operations lead to measurements of occupation numbers  $[0_{AB}, 0_{CD}]$  and  $[1_{AB}, 1_{CD}]$  with equal probabilities, reflecting the fusion of MZMs into  $I$  and  $\psi$  channels. In the control experiment, the sequence of operations always leads to fusion of MZMs into  $I$  channel so the measured occupation numbers are always  $[0_{AB}, 0_{CD}]$ .

In both sequences, the system is first initialized to a unique ground state of the system  $|\psi_{GS}\rangle$ , which is determined by the relative magnitudes of the turned-on couplings  $U_{AB}$ ,  $U_{BC}$ , and  $U_{CD}$ , but the exact ground state is not important in the following. The fusion and control sequences applied to the ground state  $|\psi_{GS}\rangle$  look very similar but they should lead to very different measurement outcomes of the occupation numbers  $N_{AB}$  and  $N_{CD}$  in the last step of the experiments, allowing us to obtain strong evidence of the Majorana fusion rules.

In the fusion experiment, one first turns off the couplings  $U_{AB}$  and  $U_{CD}$ , so  $|\psi_{GS}\rangle$  evolves to a state  $|\psi_F\rangle = \frac{1}{\sqrt{2}}(|0_{AB}, 0_{CD}\rangle + |1_{AB}, 1_{CD}\rangle)$ . This corresponds to the initialization of the system into a state with well-defined occupation numbers of the fermions  $f_{AD}^\dagger$  and  $f_{BC}^\dagger$  as discussed above [see Eqs. (14)]. After this, one can turn off the coupling  $U_{BC}$  without changing the state of the system and finally measure the occupation numbers  $N_{AB}$  and  $N_{CD}$ . Thus, in the fusion experiment the occupation numbers  $[0_{AB}, 0_{CD}]$  and  $[1_{AB}, 1_{CD}]$  are measured with equal probabilities, reflecting the fusion of MZMs into  $I$  and  $\psi$  channels [see Eq. (13)].

In the control experiment one first turns off the coupling  $U_{BC}$ . This initializes the system into a state with well-defined occupation numbers of the fermions  $f_{AB}^\dagger$  and  $f_{CD}^\dagger$ , e.g., assuming that  $U_{AB}, U_{CD} > 0$  we obtain  $|\psi_C\rangle = |0_{AB}, 0_{CD}\rangle$ . After this, one can turn off the coupling  $U_{AB}$  and  $U_{CD}$  without changing the state of the system and, finally, measure the occupation numbers  $N_{AB}$  and  $N_{CD}$ . Thus, in the control experiment, the occupation numbers  $[0_{AB}, 0_{CD}]$  are always measured, reflecting the fusion of MZMs into  $I$  channel.

The requirements for the fusion-rule detection mentioned above can be satisfied by choosing the charging energy to be  $E_{C1(2)} \sim 0.1$  meV and tuning the Josephson energies in the range  $E_{J1(2)} \in [0, 50E_{C1(2)}]$  so  $U_{\max} \sim 0.5E_c$  to  $U_{\min} \sim 10^{-7}E_c$ . Taking  $A_{\text{eff}}^{S(N)} \sim 0.1E_0d_0$  and  $\Delta_{\text{ex}} \sim \Delta_0 \sim 0.03E_0$ , we find that the Majorana overlap across the superconducting island 1 (2) can be safely neglected if  $L_{AB(CD)} \gtrsim 1 \mu\text{m}$ . According to our calculations the gap  $\Delta_{\text{ex}}$  opened due to TRS symmetry breaking can be tuned with gate voltages to be between  $[0.005E_0, 0.03E_0]$ . Thus, by choosing  $L_{BC} \sim 0.5 \mu\text{m}$ , we find  $U_{\max} \sim 10^{-3}E_0$  and  $U_{\min} \sim 10^{-8}E_0$ . With these values of the parameters, also  $U_{\max} < \Delta_{\text{gap}}$ , so we can neglect the bulk excitations in our low-energy theory. At the same time,  $k_B T \ll \Delta_{\text{gap}}$  and  $k_B T \ll U_{\max}$ , so also the thermal excitations can be neglected. The operation time should satisfy  $T_{\text{op}} \gg \hbar/\Delta_{\text{gap}} \sim 10$  ps and  $100$  ps  $\sim \hbar/U_{\max} \ll T_{\text{op}} \ll \hbar/U_{\min} \sim 10$   $\mu\text{s}$ . These requirements can be satisfied in gate- and flux-controlled tuning of  $E_{J1(2)}$  [47,49], as well as in gate-controlled tuning of  $\Delta_{\text{ex}}$ . The operations should be performed much faster than the quasiparticle poisoning time, but since the external magnetic field is not required this does not pose additional constraints on the operation unless the poisoning time is many orders of magnitude shorter than the observed and predicted  $T_{\text{pois}}$  in state-of-the-art devices [53–55].

## V. CONCLUSIONS AND DISCUSSION

We have shown that the combination of the proximity-induced superconductivity and the spontaneous TRS breaking

allows the possibility to realize MZMs in band-inverted electron-hole bilayers in the absence of magnetic field. We have studied the signatures of MZMs in superconductor/TRS broken insulator/superconductor Josephson junctions numerically using the full lattice model and analytically using the low-energy effective edge theory. We have shown that all the requirements for the observation of the  $4\pi$  Josephson effect can be satisfied in this system. By modifying the setup so the charging energy of the superconducting islands exceeds the temperature, it is possible to detect the Majorana fusion rules by utilizing tunable Josephson junctions and the gate-tunable energy gap opened by the the spontaneous TRS breaking order parameter. Our estimates of the relevant energy scales indicate that all the requirements for robust Majorana fusion-rule detection can be satisfied in this system. We point out that in addition to the  $4\pi$  periodic Josephson effect and the signatures associated with their non-Abelian nature, MZMs also give rise to a zero-bias peak in the conductance due to resonant Andreev reflection [17,18] (see Appendix D for more details).

In the calculations shown above, we have assumed that the superconductivity is induced on both layers and the induced self-energy is independent of energy. In Appendix E, we show that the topological phase diagram also remains similar in a situation where the superconductor is placed on the top of the electron layer, and it induces an energy-dependent self-energy only on the electron layer. In this case, the energy gap between MZMs and other quasiparticle states is reduced because the effective pairing amplitude is weaker, but importantly we find that it is still sufficiently large for the robust observation of the  $4\pi$  Josephson effect. Additionally, our numerical calculations suggest that in this case the quasiparticle states at higher energies may have a weaker dispersion as a function of  $\phi$ , reducing the  $2\pi$  contribution to the Josephson current, and therefore making it easier to observe the  $4\pi$  Josephson effect.

## ACKNOWLEDGMENTS

We thank D. I. Pikulin for useful discussions and comments. The paper is supported by the Foundation for Polish Science through the IRA Programme co-financed by EU within SG OP and the Academy of Finland Project No. 331094. We acknowledge the computational resources provided by the Aalto Science-IT project and access to the computing facilities of the Interdisciplinary Center of Modeling at the University of Warsaw, Grants No. GB82-13, No. G78-13 and No. G75-10.

## APPENDIX A: ANALYTICAL SOLUTIONS OF EFFECTIVE LOW-ENERGY THEORY FOR EDGE EXCITATIONS

In this Appendix, we derive analytical solutions of the effective low-energy edge Hamiltonian  $H_e$ , Eq. (5), where  $A_{\text{eff}}(x)$  is the velocity of the helical edge states and  $\Delta_s(x)$  [ $\Delta_{\text{ex}}(x)$ ] determines the energy gap opened by the proximity induced superconductivity (TRS breaking order parameter) in the superconducting (normal) region of  $x$ .

### 1. Solution of $H_e$ in the normal region

In the normal regions,  $\Delta_{\text{ex}} > 0$  and  $|\Delta_s(x)| = 0$ . The propagating solutions for  $|E| > \Delta_{\text{ex}}$  are

$$\begin{aligned} \psi(x) = & b_1 \begin{pmatrix} 1 \\ i\delta \\ 0 \\ 0 \end{pmatrix} e^{ik_N x} + b_2 \begin{pmatrix} -i\delta \\ 1 \\ 0 \\ 0 \end{pmatrix} e^{-ik_N x} \\ & + b_3 \begin{pmatrix} 0 \\ 0 \\ 1 \\ i\delta \end{pmatrix} e^{-ik_N x} + b_4 \begin{pmatrix} 0 \\ 0 \\ -i\delta \\ 1 \end{pmatrix} e^{ik_N x}, \end{aligned} \quad (\text{A1})$$

where  $\delta = \frac{\Delta_{\text{ex}}}{\sqrt{E^2 - \Delta_{\text{ex}}^2} + E}$  and  $k_N = \frac{\sqrt{E^2 - \Delta_{\text{ex}}^2}}{A_{\text{eff}}^N}$ , and the evanescent solutions for  $|E| < \Delta_{\text{ex}}$  are

$$\begin{aligned} \psi(x) = & p_1 \begin{pmatrix} e^{i\theta_1} \\ 1 \\ 0 \\ 0 \end{pmatrix} e^{-\kappa_N x} + p_2 \begin{pmatrix} -e^{-i\theta_1} \\ 1 \\ 0 \\ 0 \end{pmatrix} e^{\kappa_N x} \\ & + p_3 \begin{pmatrix} 0 \\ 0 \\ e^{i\theta_1} \\ 1 \end{pmatrix} e^{\kappa_N x} + p_4 \begin{pmatrix} 0 \\ 0 \\ -e^{-i\theta_1} \\ 1 \end{pmatrix} e^{-\kappa_N x}, \end{aligned} \quad (\text{A2})$$

where  $e^{i\theta_1} = \frac{\sqrt{\Delta_{\text{ex}}^2 - E^2} - iE}{\Delta_{\text{ex}}}$  and  $\kappa_N = \frac{\sqrt{\Delta_{\text{ex}}^2 - E^2}}{A_{\text{eff}}^N}$ .

### 2. Solution of $H_e$ in the superconducting region

In the superconducting region,  $\Delta_{\text{ex}} = 0$  and  $\Delta_s(x) = \Delta_0 e^{i\varphi}$ . In our analytical calculations, we only need the decaying solutions for  $|E| < \Delta_0$ . The solutions decaying in  $x \rightarrow -\infty$  and  $x \rightarrow \infty$  have the form

$$\psi(x) = a_1 \begin{pmatrix} e^{i\varphi} e^{-i\gamma} \\ 0 \\ 1 \\ 0 \end{pmatrix} e^{\kappa_S x} + a_2 \begin{pmatrix} 0 \\ e^{i\varphi} e^{i\gamma} \\ 0 \\ 1 \end{pmatrix} e^{\kappa_S x}, \quad (\text{A3})$$

$$\psi(x) = c_1 \begin{pmatrix} e^{i\varphi} e^{i\gamma} \\ 0 \\ 1 \\ 0 \end{pmatrix} e^{-\kappa_S x} + c_2 \begin{pmatrix} 0 \\ e^{i\varphi} e^{-i\gamma} \\ 0 \\ 1 \end{pmatrix} e^{-\kappa_S x}, \quad (\text{A4})$$

where  $e^{i\gamma} = \frac{E + i\sqrt{\Delta_0^2 - E^2}}{\Delta_0}$  and  $\kappa_S = \frac{\sqrt{\Delta_0^2 - E^2}}{A_{\text{eff}}^S}$ .

### 3. Majorana zero mode at the interface of TRS broken and superconducting regions

By combining the solutions Eqs. (A2) and (A4) with proper boundary conditions, it is easy to see that if the TRS broken insulator (superconductor) covers the region  $x < 0$  ( $x > 0$ ), there is a MZM localized at  $x = 0$ , namely, there exists a zero-energy solution of the Hamiltonian Eq. (5) of the

form

$$\psi(x) = \begin{cases} \frac{1}{\mathcal{N}} \begin{pmatrix} -e^{-i\pi/4} e^{i\varphi/2} \\ e^{-i\pi/4} e^{i\varphi/2} \\ e^{i\pi/4} e^{-i\varphi/2} \\ e^{i\pi/4} e^{-i\varphi/2} \end{pmatrix} e^{\kappa_N x}, & x < 0 \\ \frac{1}{\mathcal{N}} \begin{pmatrix} -e^{-i\pi/4} e^{i\varphi/2} \\ e^{-i\pi/4} e^{i\varphi/2} \\ e^{i\pi/4} e^{-i\varphi/2} \\ e^{i\pi/4} e^{-i\varphi/2} \end{pmatrix} e^{-\kappa_S x}, & x > 0. \end{cases} \quad (\text{A5})$$

The corresponding field operator  $\gamma$  in the second quantized form obeys  $\gamma = \gamma^\dagger$ , and by choosing the normalization constant  $\mathcal{N}$  properly, we obtain  $\gamma^2 = 1$ . Therefore, this solution satisfies the algebra of the MZMs.

### 4. Energy spectrum of subgap states and hybridization of MZMs across the TRS broken insulator in a Josephson junction

In a Josephson junction, the spatial profiles of  $\Delta_{\text{ex}}(x)$  and  $\Delta_s(x)$  are

$$\Delta_{\text{ex}}(x) = \begin{cases} \Delta_{\text{ex}} & 0 \leq x \leq L \\ 0 & \text{elsewhere} \end{cases} \quad (\text{A6})$$

and

$$\Delta_s(x) = \begin{cases} \Delta_0 e^{-i\phi/2} & x < 0 \\ 0 & 0 \leq x \leq L \\ \Delta_0 e^{i\phi/2} & x > L. \end{cases} \quad (\text{A7})$$

In the case  $|E| > \Delta_{\text{ex}}$ , the solutions are of the form Eq. (A3) for  $x < 0$ , Eq. (A1) for  $0 \leq x \leq L$ , and Eq. (A4) for  $x > L$ . Thus, the continuity of the wave function at  $x = 0$  and  $x = L$  leads to constraints

$$\begin{pmatrix} a_1 e^{-i\phi/2} e^{-i\gamma} \\ a_2 e^{-i\phi/2} e^{i\gamma} \\ a_1 \\ a_2 \end{pmatrix} = \begin{pmatrix} b_1 - i\delta b_2 \\ i\delta b_1 + b_2 \\ b_3 - i\delta b_4 \\ i\delta b_3 + b_4 \end{pmatrix} \quad (\text{A8})$$

and

$$\begin{pmatrix} b_1 e^{i\kappa_N L} - i\delta b_2 e^{-i\kappa_N L} \\ i\delta b_1 e^{i\kappa_N L} + b_2 e^{-i\kappa_N L} \\ b_3 e^{-i\kappa_N L} - i\delta b_4 e^{i\kappa_N L} \\ i\delta b_3 e^{-i\kappa_N L} + b_4 e^{i\kappa_N L} \end{pmatrix} = \begin{pmatrix} c_1 e^{i\phi/2} e^{i\gamma} e^{-\kappa_S L} \\ c_2 e^{i\phi/2} e^{-i\gamma} e^{-\kappa_S L} \\ c_1 e^{-\kappa_S L} \\ c_2 e^{-\kappa_S L} \end{pmatrix}. \quad (\text{A9})$$

These equations can be written in matrix form as  $M(a_1, a_2, b_1, b_2, b_3, b_4, c_1, c_2)^T = 0$ , which has nontrivial solutions only if  $\det(M) = 0$ , so this condition determines the allowed energies as a function of the parameters of the model  $E(A_{\text{eff}}^N, \Delta_{\text{ex}}, \Delta_0, L, \phi)$ .

In the case  $|E| < \Delta_{\text{ex}}$ , the solutions are of the form Eq. (A3) for  $x < 0$ , Eq. (A2) for  $0 \leq x \leq L$ , and Eq. (A4) for  $x > L$ . Thus, the continuity of the wave function at  $x = 0$  and  $x = L$  leads to constraints

$$\begin{pmatrix} a_1 e^{-i\phi/2} e^{-i\gamma} \\ a_2 e^{-i\phi/2} e^{i\gamma} \\ a_1 \\ a_2 \end{pmatrix} = \begin{pmatrix} p_1 e^{i\theta_1} - p_2 e^{-i\theta_1} \\ p_1 + p_2 \\ p_3 e^{i\theta_1} - p_4 e^{-i\theta_1} \\ p_3 + p_4 \end{pmatrix} \quad (\text{A10})$$

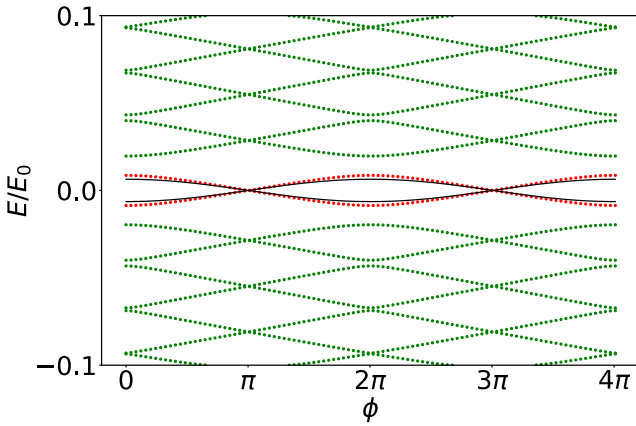


FIG. 10. Energy spectrum for  $E_G^N = 0.86E_0$ ,  $\Delta_0 = 0.1E_0$ , and  $L_N = 10d_0$ , where the Majoranas appear at the interfaces of the system. The green (red) lines are the solutions with energy  $E > \Delta_{\text{ex}}$  ( $E < \Delta_{\text{ex}}$ ). The solid black line shows the analytic expression Eq. (A12).

and

$$\begin{pmatrix} p_1 e^{i\theta_1} e^{-\kappa_N L} - p_2 e^{-i\theta_1} e^{\kappa_N L} \\ p_1 e^{-\kappa_N L} + p_2 e^{\kappa_N L} \\ p_3 e^{i\theta_1} e^{\kappa_N L} - p_4 e^{-i\theta_1} e^{-\kappa_N L} \\ p_3 e^{\kappa_N L} + p_4 e^{-\kappa_N L} \end{pmatrix} = \begin{pmatrix} c_1 e^{i\phi/2} e^{i\gamma} e^{-\kappa_S L} \\ c_2 e^{i\phi/2} e^{-i\gamma} e^{-\kappa_S L} \\ c_1 e^{-\kappa_S L} \\ c_2 e^{-\kappa_S L} \end{pmatrix}, \quad (\text{A11})$$

so the allowed energies can be computed similarly as above. In the asymptotic limit  $\kappa_N L \gg 1$ , we obtain closed form solutions

$$E = \pm 2 \frac{\Delta_0 \Delta_{\text{ex}}}{\Delta_0 + \Delta_{\text{ex}}} e^{-\kappa_N L} \cos(\phi/2), \quad \kappa_N \approx \Delta_{\text{ex}}/A_{\text{eff}}^N. \quad (\text{A12})$$

This equation describes the hybridization of the MZMs across the TRS broken insulator in the superconductor/TRS broken insulator/superconductor Josephson junction in the asymptotic limit where the MZMs are weakly coupled.

The complete subgap energy spectrum can be obtained by sweeping the energies  $E$  from  $-\Delta_0$  to  $+\Delta_0$  and numerically finding the roots of determinants of the constraint matrices (see Fig. 10).

### 5. Hybridization of the MZMs across the superconducting region

In a similar way, we can also compute the hybridization of the MZMs on the opposite sides of a superconducting island. In this case, we assume that the spatial profiles of  $\Delta_{\text{ex}}(x)$  and  $\Delta_s(x)$  are

$$\Delta_{\text{ex}}(x) = \begin{cases} \Delta_{\text{ex}} & x < 0 \\ 0 & 0 \leq x \leq L \\ \Delta_{\text{ex}} & x > L \end{cases} \quad (\text{A13})$$

and

$$\Delta_s(x) = \begin{cases} \Delta_0 & 0 \leq x \leq L \\ 0 & \text{elsewhere.} \end{cases} \quad (\text{A14})$$

In the asymptotic limit, the energies of the hybridized MZMs are

$$E = \pm 2 \frac{\Delta_0 \Delta_{\text{ex}}}{\Delta_0 + \Delta_{\text{ex}}} e^{-\kappa_S L}, \quad \kappa_S \approx \Delta_0/A_{\text{eff}}^S. \quad (\text{A15})$$

## APPENDIX B: DIFFERENT APPROACHES FOR CALCULATING THE JOSEPHSON EFFECT AND THE SYSTEM-SIZE DEPENDENCE

In this Appendix, we briefly summarize the numerical approach for calculating the Josephson current-phase relationship with the hybrid KPM developed in Ref. [52]. Moreover, we compare the hybrid KPM results to the ones obtained using exact diagonalization of small systems and the effective edge theory. Finally, we discuss the effects of system size on the magnitudes of the  $4\pi$ - and  $2\pi$ -periodic Josephson effect.

### 1. Hybrid kernel polynomial method for calculation of the supercurrent in a Josephson junction

Although we are interested in the supercurrent  $I$  at low temperatures, it is convenient to express it as

$$I = \text{Tr}[\hat{I}f(\hat{H}_{\text{BdG}})], \quad \hat{I} = \frac{e}{\hbar} \frac{d\hat{H}_{\text{BdG}}}{d\phi}, \quad (\text{B1})$$

where

$$f(\hat{H}_{\text{BdG}}) = \sum_k f(E_k) |\psi_k\rangle \langle \psi_k|, \quad (\text{B2})$$

$f(E)$  is the Fermi function, and  $|\psi_k\rangle$  are the eigenstates of the  $\hat{H}_{\text{BdG}}$  with eigenenergies  $E_k$ . In the KPM method,  $\hat{H}_{\text{BdG}}$  needs to be scaled so the spectrum  $\{E_k\}$  is bounded to an interval  $(-1, 1)$  by choosing a suitable unit of energy. Then,  $f(E)$  can be expanded as [58]

$$f(E) = \sum_{m=0}^{\infty} \alpha_m T_m(E), \quad (\text{B3})$$

where the Chebyshev's polynomials  $T_m(x) = \cos(m \arccos x)$  form a complete basis in  $(-1, 1)$  and they are orthogonal under the inner product

$$\langle f \cdot g \rangle = \int_{-1}^1 \frac{f(x)g(x)}{\pi \sqrt{1-x^2}} dx, \quad (\text{B4})$$

so the Chebyshev coefficients are given by  $\alpha_m = \langle f(E) \cdot T_m(E) \rangle$ . Thus,  $f(\hat{H}_{\text{BdG}})$  can be written as

$$f(\hat{H}_{\text{BdG}}) = \sum_{m=0}^{\infty} \alpha_m T_m(\hat{H}_{\text{BdG}}). \quad (\text{B5})$$

The series needs to be truncated to some order  $M$  and, to ensure stable convergence, the method of Ref. [52] utilizes Jackson kernel [58]

$$K_m = \frac{M-m+1}{M+1} \cos \frac{\pi m}{M+1} + \frac{1}{M+1} \frac{\sin \frac{\pi m}{M+1}}{\tan \frac{\pi}{M+1}} \quad (\text{B6})$$

to modify the coefficients  $\alpha_m$  to  $\tilde{\alpha}_m = \alpha_m K_m$ , so

$$\tilde{f}(\hat{H}_{\text{BdG}}) = \sum_{m=0}^M \tilde{\alpha}_m T_m(\hat{H}_{\text{BdG}}). \quad (\text{B7})$$

The number of Chebyshev moments  $M$  together with the choice of the kernel sets the energy resolution of the KPM approximation [52,58]. The Fermi function changes rapidly around the Fermi level, and therefore in the hybrid KPM method [52] a small subset of states  $k \in A$  close to the Fermi energy is calculated exactly using sparse diagonalization method, so

$$f(\hat{H}_{\text{BdG}}) \approx \tilde{f}(\hat{H}_{\text{BdG}}) + \sum_{k \in A} [f(E_k) - \tilde{f}(E_k)] |\psi_k\rangle \langle \psi_k|. \quad (\text{B8})$$

Thus, the full expression for the total supercurrent is

$$\begin{aligned} \langle \hat{I} \rangle \approx & \sum_{m=0}^M \tilde{\alpha}_m \left\{ \text{Tr}[\hat{I} T_m(\hat{H})] - \sum_{k \in A} T_m(E_k) \langle \psi_k | \hat{I} | \psi_k \rangle \right\} \\ & + \sum_{k \in A} f(E_k) \langle \psi_k | \hat{I} | \psi_k \rangle. \end{aligned} \quad (\text{B9})$$

In the numerical calculations, the superconducting phase difference is introduced through a Peierls substitution so the expectation value of the current operator can be computed across a cut in the normal region separating the two superconductors [52]. Additionally, we separate the total supercurrent into the components arising from the MZMs  $I_M$  and the other Andreev levels. The first one gives the  $4\pi$  periodic contribution to the Josephson current and the latter one is responsible for the  $2\pi$  periodic Josephson effect.

## 2. Comparison of the hybrid KPM method and exact diagonalization

In the case of small systems, we can compare the hybrid KPM results to the supercurrent obtained using exact diagonalization. For this purpose, we consider the device geometry shown in Fig. 3. We find that for a sufficiently large number of moments,  $M = 700$  and the maximum number of computed subgap states  $K = 200$  the hybrid KPM results are in good agreement with the exact results (see Fig. 11). In all our hybrid KPM calculations, we have used  $M \geq 700$  and  $K \geq 200$ .

## 3. Comparison of the hybrid KPM and the effective edge theory results

We have also compared the hybrid KPM results to the results obtained using the low-energy effective edge theory. As can be seen in Fig. 12, the  $4\pi$ -periodic component  $I_M(\phi)$  originating from the MZMs is well captured by the effective edge theory. In the asymptotic limit  $k_N L \gg 1$ , we obtain from Eqs. (A12):

$$I_M(\phi) = 2 \frac{e}{\hbar} \frac{\Delta_0 \Delta_{\text{ex}}}{\Delta_0 + \Delta_{\text{ex}}} e^{-\Delta_{\text{ex}} L_N / A_{\text{eff}}^N} \frac{\mathcal{P}_{12} + \mathcal{P}_{34}}{2} \sin(\phi/2). \quad (\text{B10})$$

We find that this analytic expression accurately describes the parametric dependencies of the  $4\pi$ -periodic current in the regime of weakly broken TRS. (In all figures, we plot  $I_M(\phi)$  for  $\mathcal{P}_{12} = 1$  and  $\mathcal{P}_{34} = 1$ .) On the other hand, the low-energy effective edge theory strongly underestimates the magnitude of the  $2\pi$ -periodic component, because in the full lattice model there exist more Andreev levels with significant dispersion as a function of  $\phi$  than in the case of the effective edge theory.

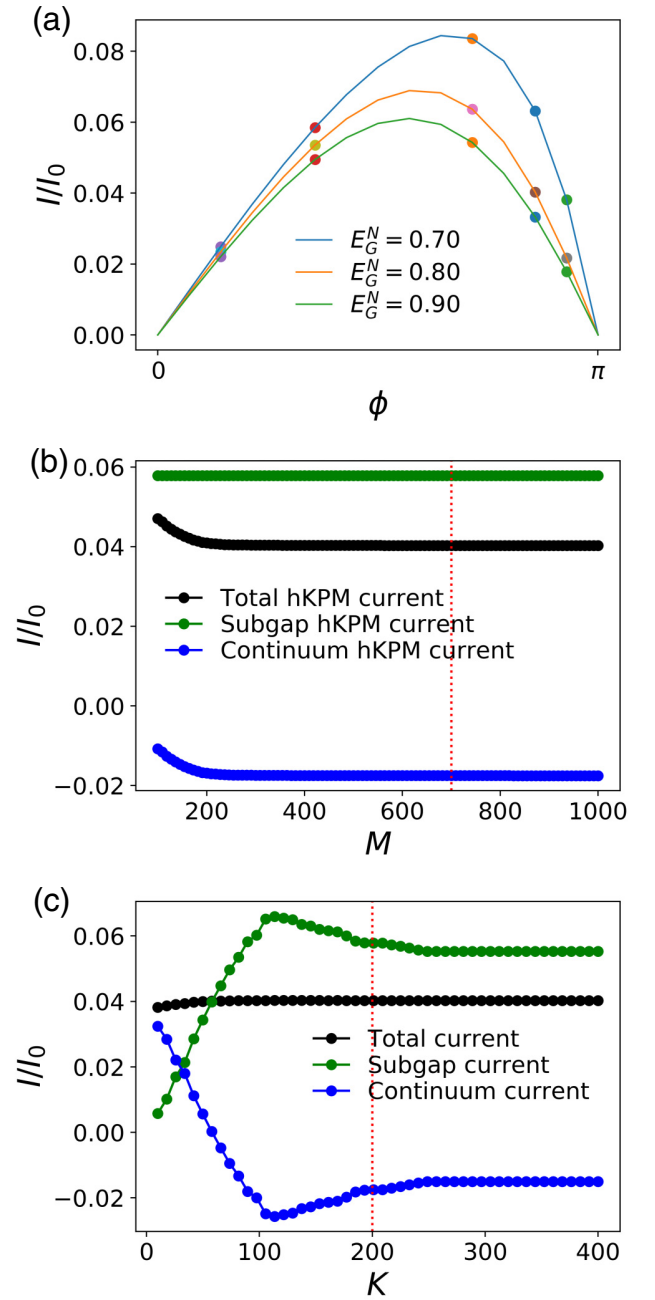


FIG. 11. (a) Current-phase relationship for  $L_N = 10d_0$ ,  $W = 60d_0$ ,  $L_S = 15d_0$ ,  $\Delta_0 = 0.1E_0$ ,  $E_G^N = 0.7E_0, 0.8E_0, 0.9E_0$ , and  $E_G^S = 1.3E_0$ . The solid lines show the current calculated using hybrid kernel polynomial method and the circles show the exact results for particular values of  $\phi$ . Here, the number of moments is  $M = 700$  and the maximum number of computed subgap states is  $K = 200$ . (b) Convergence of the subgap, continuum, and the total current with increasing  $M$  for  $K = 200$  for  $\phi = 2.69$  and  $E_G^N = 0.8E_0$ . (c) Same with increasing  $K$  for  $M = 700$ .

## 4. System size dependence of the Josephson effects

We have also calculated the dependence of the  $2\pi$  and  $4\pi$  periodic Josephson effects on the system size (see Fig. 13). We find that  $L_S$  does not affect the results significantly as long

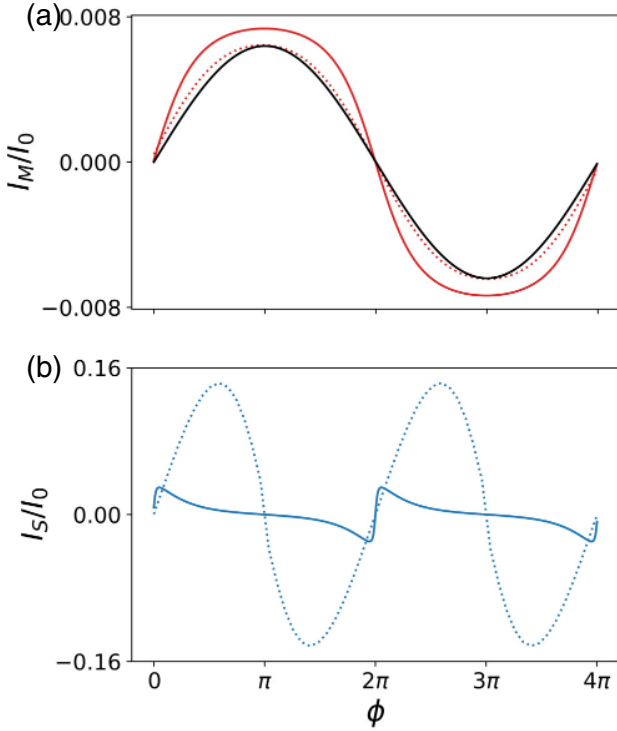


FIG. 12. (a) The  $4\pi$ -periodic supercurrent  $I_M(\phi)$  originating from the MZMs. The low-energy effective theory (solid red line) agrees well with the numerical results obtained from the lattice model (dashed red line). The results are also in good agreement with the analytical expression (black line) given by Eq. (B10). (b) The  $2\pi$ -periodic supercurrent  $I_S(\phi)$  originating from the rest of the states. The  $I_S(\phi)$  of the full lattice model (dashed blue line) deviates significantly from the results of the low-energy effective edge theory (solid blue line) because there exists many high-energy Andreev levels with significant dispersion as a function of  $\phi$ . The corresponding energy spectra for the lattice model and continuum model are shown in Figs. 4(b) and 10, respectively. The model parameters are  $E_G^N = 0.86E_0$ ,  $L_N = 10d_0$ ,  $W = 150d_0$ ,  $E_G^S = 1.3E_0$  and  $L_S = 15d_0$ , and  $\Delta_0 = 0.1E_0$ .

as  $L_S > 10d_0$ . As expected, increasing  $L_N$  decreases both the  $2\pi$  and  $4\pi$  periodic Josephson effects. On the other hand, decreasing  $W$  reduces the magnitude of the  $2\pi$  Josephson effect but it does not influence significantly the  $4\pi$  periodic Josephson effect.

### APPENDIX C: FUSION OF MAJORANA ZERO MODES

In the fusion setup shown in Fig. 8, the four MZMs, described by the operators  $\gamma_i = \gamma_i^\dagger$  ( $i = A, B, C, D$ ) satisfying  $\{\gamma_i, \gamma_j\} = 2\delta_{ij}$ , are related to fermionic operators:

$$f_{AB}^\dagger = \frac{1}{2}(\gamma_A + i\gamma_B), \quad f_{CD}^\dagger = \frac{1}{2}(\gamma_C + i\gamma_D). \quad (C1)$$

The occupation operators of these fermions are given by

$$\begin{aligned} \hat{N}_{AB} &= f_{AB}^\dagger f_{AB} = \frac{1 - i\gamma_A\gamma_B}{2}, \\ \hat{N}_{CD} &= f_{CD}^\dagger f_{CD} = \frac{1 - i\gamma_C\gamma_D}{2}. \end{aligned} \quad (C2)$$

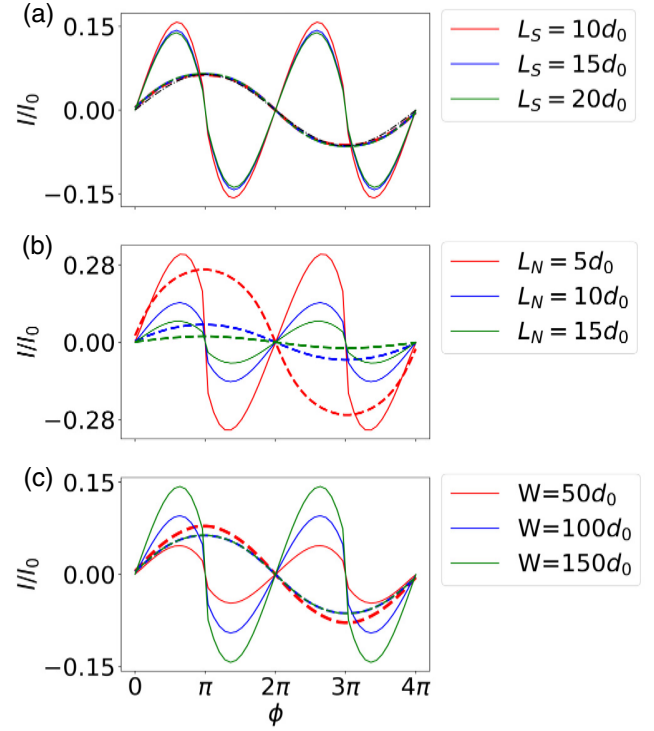


FIG. 13. (a) The  $4\pi$ -periodic supercurrent  $I_M(\phi)$  originating from the MZMs (dashed, magnified ten times) and the  $2\pi$ -periodic current  $I_S(\phi)$  (solid) originating from the rest of the states for  $L_N = 10d_0$ ,  $W = 150d_0$ , and  $L_S = 10, 15, 20d_0$ . The analytic approximation Eq. (B10) is shown with dash-dot black line. (b) Same for  $W = 150d_0$ ,  $L_S = 15d_0$ , and  $L_N = 5, 10, 15d_0$ . (c) Same for  $L_S = 15d_0$ ,  $L_N = 10d_0$ , and  $W = 50, 100, 150d_0$ . The other parameters are  $\Delta_0 = 0.1E_0$ ,  $E_G^N = 0.86E_0$ , and  $E_G^S = 1.3E_0$ .

In the case of even total parity, the two possible states of the system are

$$|0_{AB}, 0_{CD}\rangle, \quad |1_{AB}, 1_{CD}\rangle = f_{AB}^\dagger f_{CD}^\dagger |0_{AB}, 0_{CD}\rangle, \quad (C3)$$

satisfying

$$\begin{aligned} \hat{N}_{AB}|N_{AB}N_{CD}\rangle &= N_{AB}|N_{AB}N_{CD}\rangle, \\ \hat{N}_{CD}|N_{AB}N_{CD}\rangle &= N_{CD}|N_{AB}N_{CD}\rangle. \end{aligned} \quad (C4)$$

Alternatively, we can form the fermion operators, number operators, and states as

$$f_{AD}^\dagger = \frac{1}{2}(\gamma_A + i\gamma_D), \quad f_{BC}^\dagger = \frac{1}{2}(\gamma_B + i\gamma_C), \quad (C5)$$

$$\begin{aligned} \hat{N}_{AD} &= f_{AD}^\dagger f_{AD} = \frac{1 - i\gamma_A\gamma_D}{2}, \\ \hat{N}_{BC} &= f_{BC}^\dagger f_{BC} = \frac{1 - i\gamma_B\gamma_C}{2}, \end{aligned} \quad (C6)$$

and

$$|0_{AD}, 0_{BC}\rangle, \quad |1_{AD}, 1_{BC}\rangle = f_{AD}^\dagger f_{BC}^\dagger |0_{AD}, 0_{BC}\rangle. \quad (C7)$$

The two sets of fermionic operators are related as

$$\begin{aligned} f_{AD}^\dagger &= \frac{1}{2}(f_{AB} + f_{AB}^\dagger - f_{CD} + f_{CD}^\dagger), \\ f_{BC}^\dagger &= \frac{i}{2}(f_{AB} - f_{AB}^\dagger + f_{CD} + f_{CD}^\dagger). \end{aligned} \quad (\text{C8})$$

Thus, by straightforward algebra we find that the basis states are related as

$$\begin{aligned} |0_{AD}0_{BC}\rangle &= \frac{1}{\sqrt{2}}(|0_{AB}0_{CD}\rangle + |1_{AB}1_{CD}\rangle), \\ |1_{AD}1_{BC}\rangle &= \frac{i}{\sqrt{2}}(|1_{AB}1_{CD}\rangle - |0_{AB}0_{CD}\rangle). \end{aligned} \quad (\text{C9})$$

The important consequence of this simple algebra is that if one initializes the system into a state with well-defined fermion numbers  $N_{AD}$  and  $N_{BC}$ , and then measures the fermion number  $N_{AB}$  (or  $N_{CD}$ ), the outcome will be 0 and 1 with equal probabilities. This is a manifestation of the fusion rule of the MZMs,

$$\sigma \times \sigma = I + \psi, \quad (\text{C10})$$

which states that the MZMs can coalesce into identity  $I$  or a fermion  $\psi$ .

#### APPENDIX D: ZERO-BIAS CONDUCTANCE PEAK DUE TO RESONANT ANDREEV REFLECTION

In addition to the  $4\pi$  periodic Josephson effect and the signatures associated with their non-Abelian nature, MZMs also give rise to a zero-bias peak in the conductance due to resonant Andreev reflection [17,18]. To illustrate this, we consider the setup shown in Fig. 14(a), where the TRS broken insulating region is coupled to a QSH insulator lead on the left and a superconducting lead on the right. If the system is in the topologically nontrivial phase with  $\nu = -1$ , two MZMs  $\gamma_1$  and  $\gamma_2$  are localized at the edge of the system at the interface of the TRS broken insulator and the superconductor as illustrated in Fig. 14(a). In this kind of situation, each MZM contributes  $2e^2/h$  to the zero-bias peak, so the total value of the conductance peak is  $G = 4e^2/h$ . The coupling of the MZMs to the normal lead is stronger at larger values of  $E_G^N$ , where the spontaneous TRS breaking introduces only a small gap in the edge-state spectrum, leading to a wide plateau in the quantized conductance. When  $E_G^N$  is decreased, the edge gap increases and the conductance peak appears only at small range of voltages  $V_{dc}$ . Close to the phase transition between the trivial and nontrivial phases, the low-energy states are delocalized along the whole width of the system at the interface of TRS broken insulator and superconductor so they couple very weakly to the QSH insulator lead, and therefore they are not clearly visible in the conductance.

#### APPENDIX E: EFFECTS OF THE LAYER AND ENERGY DEPENDENCE OF THE INDUCED SUPERCONDUCTIVITY

So far, we have assumed that the amplitude of the self-energy  $\Sigma$  induced by the superconductor is constant  $\Delta_0$ , which is independent of position  $\mathbf{r}$ , momentum  $\mathbf{k}$ , the layer index, and energy. This is a standard approximation used in

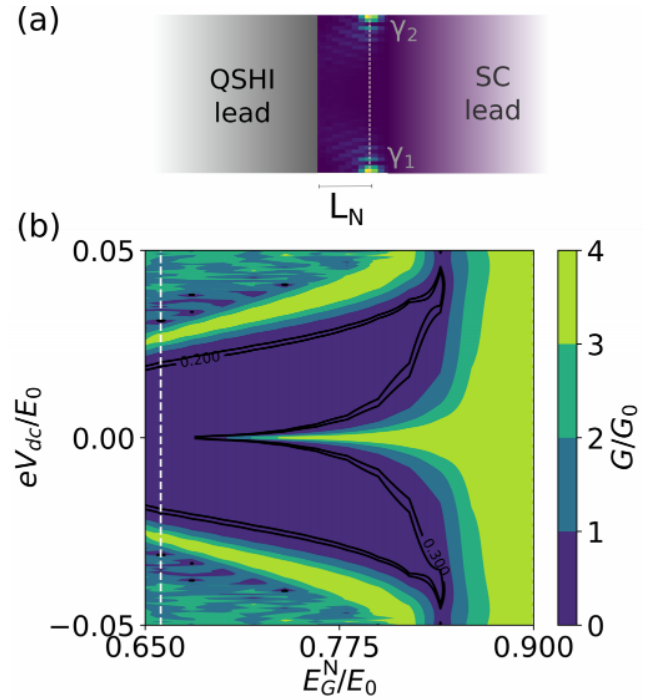


FIG. 14. (a) Schematic illustration of the setup for detection of MZMs through zero-bias peak in the conductance. The insulating region with spontaneously broken TRS is connected to a quantum spin Hall insulator lead on the left and a superconducting lead on the right. The MZMs  $\gamma_1$  and  $\gamma_2$  are localized at the interface of the TRS broken insulator and the superconductor if the system is in the topologically nontrivial phase with  $\nu = -1$ . (b) Conductance  $G/G_0$  ( $G_0 = e^2/h$ ) plotted as a function of  $E_G^N/E_0$  and  $eV_{dc}/E_0$ . The white dashed line marks the phase boundary between trivial  $\nu = 1$  and nontrivial  $\nu = -1$  phases. The value of the zero-bias peak in the conductance in the topologically nontrivial phase is  $G = 4e^2/h$ . The model parameters are  $L_N = 5d_0$ ,  $W = 100d_0$ ,  $E_G^S = 1.3E_0$ .

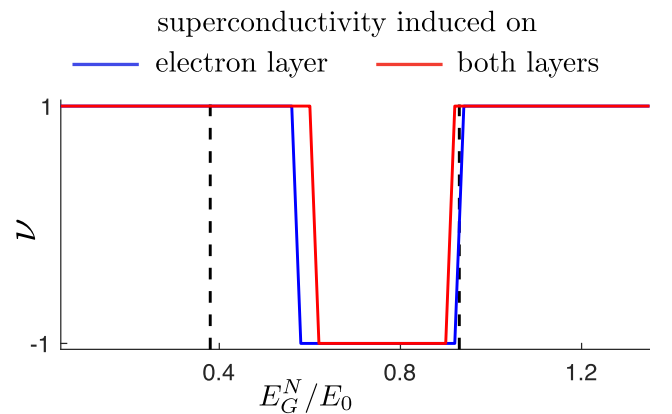


FIG. 15.  $\mathbb{Z}_2$  topological invariant  $\nu$  when the superconductivity is induced on the electron layer (blue) [both layers (red)] as a function of  $E_G^N/E_0$  for the setup shown in Fig. 2. The TRS is spontaneously broken in the region between the black dashed lines. The other model parameters are  $E_G^S = 1.0E_0$ ,  $W = 150d_0$ , and  $\Delta_0 = 0.1E_0$ .

the literature, but in reality  $\Sigma$  depends on the microscopic details of the superconductor and the placement of the superconductor in proximity to the bilayer system. In this section, we go beyond the simplest approximation by considering a conventional  $s$ -wave superconducting metal placed on the top of the electron layer in the bilayer system.

The Hamiltonian of the whole system  $\hat{H}_{\text{tot}}$  consists of

$$\hat{H}_{\text{tot}} = \hat{H}_{\text{SC}} + \hat{H} + \hat{H}_T, \quad (\text{E1})$$

where  $\hat{H}_{\text{SC}}$  is the Hamiltonian of  $s$ -wave superconductor having an arbitrary number of layers (the layer index is included in the lattice site index  $i$ ):

$$\hat{H}_{\text{SC}} = \sum_{i,j,\sigma} t_{i,j} a_{i\sigma}^\dagger a_{j\sigma} - \sum_i (\Delta_{\text{SC}} a_{i\uparrow}^\dagger a_{i\downarrow}^\dagger + \text{H.c.}). \quad (\text{E2})$$

$$H_{\text{BdG}}^{\text{eff}}(E, \mathbf{k}) = \begin{pmatrix} H(\mathbf{k}) + \Sigma_0(E, \mathbf{k}) + \Sigma_Z(E, \mathbf{k}) & \Sigma_X(E, \mathbf{k}) \\ \Sigma_X^*(E, \mathbf{k}) & -\sigma_y H^T(-\mathbf{k}) \sigma_y + \Sigma_0(E, \mathbf{k}) - \Sigma_Z(E, \mathbf{k}) \end{pmatrix}, \quad (\text{E4})$$

where the self-energy terms are

$$\begin{aligned} \Sigma_0(E, \mathbf{k}) &= -\tilde{t}^2 \int d\epsilon \frac{E \nu(\epsilon, \mathbf{k})}{\epsilon^2 + |\Delta_{\text{SC}}|^2 - E^2} \frac{\tau_z + \tau_0}{2} \sigma_0, \\ \Sigma_Z(E, \mathbf{k}) &= -\tilde{t}^2 \int d\epsilon \frac{\epsilon \nu(\epsilon, \mathbf{k})}{\epsilon^2 + |\Delta_{\text{SC}}|^2 - E^2} \frac{\tau_z + \tau_0}{2} \sigma_0, \\ \Sigma_X(E, \mathbf{k}) &= \tilde{t}^2 \int d\epsilon \frac{\Delta_{\text{SC}} \nu(\epsilon, \mathbf{k})}{\epsilon^2 + |\Delta_{\text{SC}}|^2 - E^2} \frac{\tau_z + \tau_0}{2} \sigma_0, \end{aligned} \quad (\text{E5})$$

and  $\nu(E, \mathbf{k})$  is the energy and in-plane momentum dependent local density of states at the interface superconducting layer  $z = z_I$  located directly on the top of electron layer in the bilayer system:

$$\nu(\epsilon, \mathbf{k}) = \sum_m \delta(\epsilon - \epsilon_{m\mathbf{k}}) |\chi_{m\mathbf{k}}(z_I)|^2. \quad (\text{E6})$$

Here,  $\epsilon_{m\mathbf{k}}$  and  $\chi_{m\mathbf{k}}$  are the eigenenergies and eigenstates in the metallic phase of the superconductor obtained by setting  $\Delta_{\text{SC}} = 0$ . The matrix structure  $(\tau_z + \tau_0)/2$  takes care that the self-energies are induced only to the electron layer in the bilayer system.

So far, the expressions for the self-energies are completely general but approximations are necessary to proceed further. The superconductor reduces the magnitudes of the exciton mean field in  $H_{\text{EC}}$  by inducing a superconducting gap due to the self-energy  $\Sigma_X(E, \mathbf{k})$  [this effect would be accounted in the calculation of mean fields from Eqs. (3)]. Second, the distance of the superconductor to the electron layer will typically be much smaller than the exciton radius  $d_0$  strongly screening the Coulomb interactions responsible for the formation of the bound electron-hole pairs (this effect should be accounted in the calculation of the effective interaction strengths  $g_s$  and  $g_p$  discussed in Ref. [41]). We expect that these effects strongly suppress the exciton mean fields below the superconductor and it would be difficult to find a parameter regime where large exciton mean fields and  $\Sigma_X(E, \mathbf{k})$

$\hat{H}$  is the normal state Hamiltonian for the bilayer system consisting of the noninteracting part  $H_0$  [Eq. (1)] and the exciton mean field  $H_{\text{EC}}$  [Eq. (2)] discussed in the main text, and  $\hat{H}_T$  describes the tunneling between the electron layer in the bilayer system and the superconducting layer directly on the top of it:

$$\hat{H}_T = \sum_{\langle i,j \rangle, \sigma} (\tilde{t} a_{i\sigma}^\dagger c_{j\sigma 1} + \text{H.c.}). \quad (\text{E3})$$

Here,  $t_{i,j}$  are the hopping amplitudes between lattice sites  $i$  and  $j$  in the superconductor,  $\Delta_{\text{SC}}$  is the superconducting order parameter, and  $a_{i\sigma}^\dagger$  and  $a_{i\sigma}$  ( $c_{i\sigma 1}^\dagger$  and  $c_{i\sigma 1}$ ) are the creation and annihilation operators in the superconductor (electron layer in the bilayer system). By integrating out the superconductor following the approach developed in Ref. [59], the effective Hamiltonian for the bilayer system at energies  $E < \Delta_{\text{SC}}$  can be written as

are simultaneously present in the same region of the bilayer system. Thus, we believe that it is a good approximation to assume that  $H_{\text{EC}}(\mathbf{k}, \mathbf{x}) = 0$  in the regions of  $\mathbf{x}$  covered by the superconductor. This assumption is used in the following, but nevertheless we stress that our results would remain qualitatively similar as long as the magnitude of the induced superconducting gap is larger than the exciton mean fields in the regions of  $\mathbf{x}$  covered by the superconductor. Second, assuming that we have a conventional  $s$ -wave superconducting metal, we can neglect the energy and momentum dependence in the density of states and assume  $\nu(\epsilon, k) \approx \nu_0$ . This way, the self-energies are simplified to a form [59]

$$\begin{aligned} \Sigma_0(E) &= -\Delta_0 \frac{E}{\sqrt{|\Delta_{\text{SC}}|^2 - E^2}} \frac{\tau_z + \tau_0}{2} \sigma_0, \quad \Sigma_Z = 0, \\ \Sigma_X(E) &= \Delta_0 \frac{\Delta_{\text{SC}}}{\sqrt{|\Delta_{\text{SC}}|^2 - E^2}} \frac{\tau_z + \tau_0}{2} \sigma_0, \end{aligned} \quad (\text{E7})$$

where we have denoted  $\Delta_0 = \pi \tilde{t}^2 \nu_0$ .

### 1. Effects of layer-dependent self-energy on the topological phase diagram and Majorana zero modes

The topological phase transitions and the MZMs occur at  $E = 0$ . Therefore, in the calculation of the topological properties, we can set  $E = 0$  in Eq. (E4). Using expressions Eqs. (E7), we notice that the only difference to our earlier analysis is that the induced superconductivity is now introduced only in the electron layer, whereas in the main text it was introduced in both layers. In Fig. 15, we compare the topological phase diagram obtained using Eqs. (E4) and (E7) to the corresponding phase diagram when superconductivity is induced on both layers [a linecut from Fig. 2(c) in the main text]. The topologically nontrivial region is slightly wider

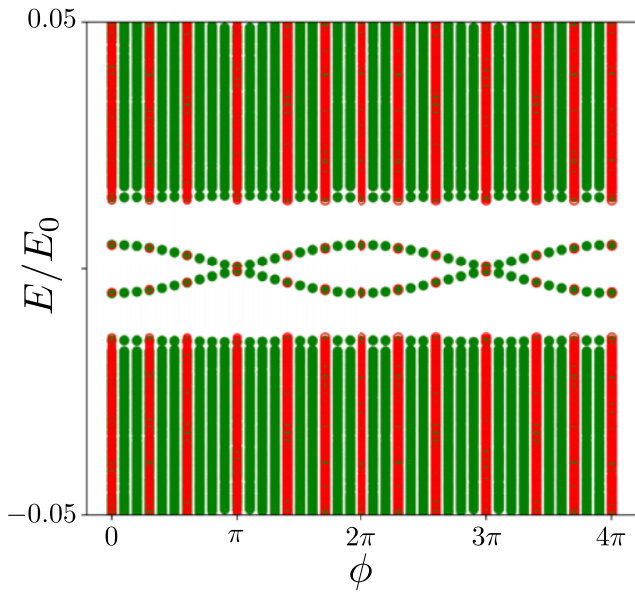


FIG. 16. Spectrum of the Josephson junction (Fig. 3) as a function of  $\phi$  when the superconductivity is induced only on the electron layer. The red circles show the spectrum of the nonlinear eigenvalue problem defined by Eqs. (E4) and (E7) for specific values of  $\phi$  and the green dots show the spectrum when we have approximated the self-energies as  $\Sigma_0(E) \approx \Sigma_0(0) = 0$  and  $\Sigma_X(E) \approx \Sigma_X(0)$  in Eqs. (E7). The model parameters are  $E_G^N = 0.86E_0$ ,  $E_G^S = 1.0E_0$ ,  $L_N = 10d_0$ ,  $L_S = 15d_0$ ,  $W = 150d_0$ ,  $\Delta_{SC} = 0.15E_0$ , and  $\Delta_0 = 0.1E_0$ .

when the superconductivity is induced only to the electron layer.

## 2. Effects of energy- and layer-dependent self-energy on the Josephson junction spectrum

Although the energy and layer dependencies of the  $\Sigma_0$  and  $\Sigma_X$  are not important for the topological properties, they can influence the quasiparticle spectrum at the nonzero energies. In Fig. 16, we show the spectrum obtained from Eqs. (E4) and (E7) for a similar Josephson junction as considered in Fig. 4(b) in the main text. The dispersions of the MZMs as a function of  $\phi$ , determining the magnitude of the  $4\pi$  Josephson effect, are very similar in Figs. 16 and 4(b). The energy gap between MZMs and other quasiparticle states is slightly reduced in Fig. 16 in comparison to Fig. 4(b) because the effective pairing amplitude is weaker but, importantly, we find that it is still sufficiently large for the robust observation of the  $4\pi$  Josephson effect according to the criteria considered in the main text. Additionally, the quasiparticle states at higher energies have a weaker dispersion as a function of  $\phi$  in Fig. 16 in comparison to Fig. 4(b), reducing the  $2\pi$  contribution to the Josephson current, and therefore suggesting that it might be easier to observe the  $4\pi$  Josephson effect when the superconductivity is induced only on the electron layer. We point out that these quantitative changes are caused mainly by the layer dependence of the self-energy  $\Sigma_X$ . The energy dependencies of  $\Sigma_0$  and  $\Sigma_X$  seem to be less important (see Fig. 16).

- [1] M. Z. Hasan and C. L. Kane, *Colloquium: Topological insulators*, *Rev. Mod. Phys.* **82**, 3045 (2010).
- [2] X.-L. Qi and S.-C. Zhang, *Topological insulators and superconductors*, *Rev. Mod. Phys.* **83**, 1057 (2011).
- [3] C. L. Kane and E. J. Mele, *Quantum Spin Hall Effect in Graphene*, *Phys. Rev. Lett.* **95**, 226801 (2005).
- [4] B. A. Bernevig, T. L. Hughes, and S.-C. Zhang, *Quantum spin Hall effect and topological phase transition in HgTe quantum wells*, *Science* **314**, 1757 (2006).
- [5] C. Liu, T. L. Hughes, X.-L. Qi, K. Wang, and S.-C. Zhang, *Quantum Spin Hall Effect in Inverted Type-II Semiconductors*, *Phys. Rev. Lett.* **100**, 236601 (2008).
- [6] M. König, S. Wiedmann, C. Brüne, A. Roth, H. Buhmann, L. W. Molenkamp, X.-L. Qi, and S.-C. Zhang, *Quantum spin Hall insulator state in HgTe quantum wells*, *Science* **318**, 766 (2007).
- [7] L. Du, I. Knez, G. Sullivan, and R.-R. Du, *Robust Helical Edge Transport in Gated InAs/GaSb Bilayers*, *Phys. Rev. Lett.* **114**, 096802 (2015).
- [8] S. Wu, V. Fatemi, Q. D. Gibson, K. Watanabe, T. Taniguchi, R. J. Cava, and P. Jarillo-Herrero, *Observation of the quantum spin Hall effect up to 100 kelvin in a monolayer crystal*, *Science* **359**, 76 (2018).
- [9] L. Fu and C. L. Kane, *Superconducting Proximity Effect and Majorana Fermions at the Surface of a Topological Insulator*, *Phys. Rev. Lett.* **100**, 096407 (2008).
- [10] L. Fu and C. L. Kane, *Josephson current and noise at a superconductor/quantum-spin-Hall-insulator/superconductor junction*, *Phys. Rev. B* **79**, 161408(R) (2009).
- [11] J. Nilsson, A. R. Akhmerov, and C. W. J. Beenakker, *Splitting of a Cooper Pair by a Pair of Majorana Bound States*, *Phys. Rev. Lett.* **101**, 120403 (2008).
- [12] C. Beenakker, *Search for Majorana fermions in superconductors*, *Annu. Rev. Condens. Matter Phys.* **4**, 113 (2013).
- [13] J. Alicea, *New directions in the pursuit of Majorana fermions in solid state systems*, *Rep. Prog. Phys.* **75**, 076501 (2012).
- [14] K. Flensberg, F. von Oppen, and A. Stern, *Engineered platforms for topological superconductivity and Majorana zero modes*, *Nat. Rev. Mater.* **6**, 944 (2021).
- [15] C. Nayak, S. H. Simon, A. Stern, M. Freedman, and S. Das Sarma, *Non-Abelian anyons and topological quantum computation*, *Rev. Mod. Phys.* **80**, 1083 (2008).
- [16] C. W. J. Beenakker, *Search for non-Abelian Majorana braiding statistics in superconductors*, *SciPost Phys. Lect. Notes* **15** (2020).
- [17] K. T. Law, P. A. Lee, and T. K. Ng, *Majorana Fermion Induced Resonant Andreev Reflection*, *Phys. Rev. Lett.* **103**, 237001 (2009).
- [18] S. Mi, D. I. Pikulin, M. Wimmer, and C. W. J. Beenakker, *Proposal for the detection and braiding of Majorana fermions in a quantum spin Hall insulator*, *Phys. Rev. B* **87**, 241405(R) (2013).

- [19] A. Y. Kitaev, Unpaired Majorana fermions in quantum wires, *Phys. Usp.* **44**, 131 (2001).
- [20] C. W. J. Beenakker, D. I. Pikulin, T. Hyart, H. Schomerus, and J. P. Dahlhaus, Fermion-Parity Anomaly of the Critical Supercurrent in the Quantum Spin-Hall Effect, *Phys. Rev. Lett.* **110**, 017003 (2013).
- [21] S. Hart, H. Ren, T. Wagner, P. Leubner, M. Mühlbauer, C. Brüne, H. Buhmann, L. W. Molenkamp, and A. Yacoby, Induced superconductivity in the quantum spin Hall edge, *Nat. Phys.* **10**, 638 (2014).
- [22] V. S. Pribrig, A. J. A. Beukman, F. Qu, M. C. Cassidy, C. Charpentier, W. Wegscheider, and L. P. Kouwenhoven, Edge-mode superconductivity in a two-dimensional topological insulator, *Nat. Nanotechnol.* **10**, 593 (2015).
- [23] I. Knez, R.-R. Du, and G. Sullivan, Andreev Reflection of Helical Edge Modes in InAs/GaSb Quantum Spin Hall Insulator, *Phys. Rev. Lett.* **109**, 186603 (2012).
- [24] R. S. Deacon, J. Wiedenmann, E. Bocquillon, F. Domínguez, T. M. Klapwijk, P. Leubner, C. Brüne, E. M. Hankiewicz, S. Tarucha, K. Ishibashi, H. Buhmann, and L. W. Molenkamp, Josephson Radiation from Gapless Andreev Bound States in HgTe-Based Topological Junctions, *Phys. Rev. X* **7**, 021011 (2017).
- [25] S. Vaitiekėnas, Y. Liu, P. Krogstrup, and C. M. Marcus, Zero-bias peaks at zero magnetic field in ferromagnetic hybrid nanowires, *Nat. Phys.* **17**, 43 (2021).
- [26] D. I. Pikulin and T. Hyart, Interplay of Exciton Condensation and the Quantum Spin Hall Effect in InAs/GaSb Bilayers, *Phys. Rev. Lett.* **112**, 176403 (2014).
- [27] Y. Naveh and B. Laikhtman, Excitonic Instability and Electric-Field-Induced Phase Transition Towards a Two-Dimensional Exciton Condensate, *Phys. Rev. Lett.* **77**, 900 (1996).
- [28] J. C. Budich, B. Trauzettel, and P. Michetti, Time Reversal Symmetric Topological Exciton Condensate in Bilayer HgTe Quantum Wells, *Phys. Rev. Lett.* **112**, 146405 (2014).
- [29] L.-H. Hu, C.-C. Chen, C.-X. Liu, F.-C. Zhang, and Y. Zhou, Topological charge-density and spin-density waves in InAs/GaSb quantum wells under an in-plane magnetic field, *Phys. Rev. B* **96**, 075130 (2017).
- [30] F. Xue and A. H. MacDonald, Time-Reversal Symmetry-Breaking Nematic Insulators Near Quantum Spin Hall Phase Transitions, *Phys. Rev. Lett.* **120**, 186802 (2018).
- [31] Q. Zhu, M. W.-Y. Tu, Q. Tong, and W. Yao, Gate tuning from exciton superfluid to quantum anomalous Hall in van der Waals heterobilayer, *Sci. Adv.* **5**, eaau6120 (2019).
- [32] D. Varsano, M. Palummo, E. Molinari, and M. Rontani, A monolayer transition-metal dichalcogenide as a topological excitonic insulator, *Nat. Nanotechnol.* **15**, 367 (2020).
- [33] Y. Zeng, F. Xue, and A. H. MacDonald, In-plane magnetic field induced density wave states near quantum spin Hall phase transitions, *Phys. Rev. B* **105**, 125102 (2022).
- [34] L. Du, X. Li, W. Lou, G. Sullivan, K. Chang, J. Kono, and R.-R. Du, Evidence for a topological excitonic insulator in InAs/GaSb bilayers, *Nat. Commun.* **8**, 1971 (2017).
- [35] X. Wu, W. Lou, K. Chang, G. Sullivan, and R.-R. Du, Resistive signature of excitonic coupling in an electron-hole double layer with a middle barrier, *Phys. Rev. B* **99**, 085307 (2019).
- [36] X.-J. Wu, W. Lou, K. Chang, G. Sullivan, A. Ikhlassi, and R.-R. Du, Electrically tuning many-body states in a Coulomb-coupled InAs/InGaSb double layer, *Phys. Rev. B* **100**, 165309 (2019).
- [37] D. Xiao, C.-X. Liu, N. Samarth, and L.-H. Hu, Anomalous Quantum Oscillations of Interacting Electron-Hole Gases in Inverted Type-II InAs/GaSb Quantum Wells, *Phys. Rev. Lett.* **122**, 186802 (2019).
- [38] H. Irie, T. Akiho, F. Couëdo, K. Suzuki, K. Onomitsu, and K. Muraki, Energy gap tuning and gate-controlled topological phase transition in InAs/In<sub>x</sub>Ga<sub>1-x</sub>Sb composite quantum wells, *Phys. Rev. Mater.* **4**, 104201 (2020).
- [39] Y. Jia, P. Wang, C.-L. Chiu, Z. Song, G. Yu, B. Jäck, S. Lei, S. Klemenž, F. A. Cevallos, M. Onyszczyk, N. Fishchenko, X. Liu, G. Farahi, F. Xie, Y. Xu, K. Watanabe, T. Taniguchi, B. A. Bernevig, R. J. Cava, L. M. Schoop *et al.*, Evidence for a monolayer excitonic insulator, *Nat. Phys.* **18**, 87 (2022).
- [40] B. Sun, W. Zhao, T. Palomaki, Z. Fei, E. Runburg, P. Malinowski, X. Huang, J. Cenker, Y.-T. Cui, J.-H. Chu, X. Xu, S. S. Ataei, D. Varsano, M. Palummo, E. Molinari, M. Rontani, and D. H. Cobden, Evidence for equilibrium exciton condensation in monolayer WTe<sub>2</sub>, *Nat. Phys.* **18**, 94 (2022).
- [41] T. Paul, V. Fernández Becerra, and T. Hyart, Interplay of quantum spin Hall effect and spontaneous time-reversal symmetry breaking in electron-hole bilayers. I. Transport properties, *Phys. Rev. B* **106**, 235421 (2022).
- [42] I. Knez, C. T. Rettner, S.-H. Yang, S. S. P. Parkin, L. Du, R.-R. Du, and G. Sullivan, Observation of Edge Transport in the Disordered Regime of Topologically Insulating InAs/GaSb Quantum Wells, *Phys. Rev. Lett.* **112**, 026602 (2014).
- [43] E. M. Spanton, K. C. Nowack, L. Du, G. Sullivan, R.-R. Du, and K. A. Moler, Images of Edge Current in InAs/GaSb Quantum Wells, *Phys. Rev. Lett.* **113**, 026804 (2014).
- [44] T. Li, P. Wang, H. Fu, L. Du, K. A. Schreiber, X. Mu, X. Liu, G. Sullivan, G. A. Csáthy, X. Lin, and R.-R. Du, Observation of a Helical Luttinger Liquid in InAs/GaSb Quantum Spin Hall Edges, *Phys. Rev. Lett.* **115**, 136804 (2015).
- [45] D. Laroche, D. Bouman, D. J. van Woerikom, A. Proutski, C. Murthy, D. I. Pikulin, C. Nayak, R. J. J. van Gulik, J. Nygård, P. Krogstrup, L. P. Kouwenhoven, and A. Geresdi, Observation of the  $4\pi$ -periodic Josephson effect in indium arsenide nanowires, *Nat. Commun.* **10**, 245 (2019).
- [46] B. van Heck, A. R. Akhmerov, F. Hassler, M. Burrello, and C. W. J. Beenakker, Coulomb-assisted braiding of Majorana fermions in a Josephson junction array, *New J. Phys.* **14**, 035019 (2012).
- [47] T. Hyart, B. van Heck, I. C. Fulga, M. Burrello, A. R. Akhmerov, and C. W. J. Beenakker, Flux-controlled quantum computation with Majorana fermions, *Phys. Rev. B* **88**, 035121 (2013).
- [48] B. van Heck, T. Hyart, and C. W. J. Beenakker, Minimal circuit for a flux-controlled Majorana qubit in a quantum spin-Hall insulator, *Phys. Scr.* **T164**, 014007 (2015).
- [49] D. Aasen, M. Hell, R. V. Mishmash, A. Higginbotham, J. Danon, M. Leijnse, T. S. Jespersen, J. A. Folk, C. M. Marcus, K. Flensberg, and J. Alicea, Milestones Toward Majorana-Based Quantum Computing, *Phys. Rev. X* **6**, 031016 (2016).
- [50] C. Liu and S. Zhang, Models and Materials for topological insulators, in *Topological Insulators*, edited by M. Franz and L. Molenkamp (Elsevier, 2013).
- [51] M. Wimmer, Algorithm 923: Efficient numerical computation of the Pfaffian for dense and banded skew-symmetric matrices, *ACM Trans. Math. Softw.* **38**, 1 (2012).

- [52] M. Irfan, S. R. Kuppaswamy, D. Varjas, P. M. Perez-Piskunow, R. Skolasinski, M. Wimmer, and A. R. Akhmerov, Hybrid kernel polynomial method, [arXiv:1909.09649](https://arxiv.org/abs/1909.09649).
- [53] J. van Veen, A. Proutski, T. Karzig, D. I. Pikulin, R. M. Lutchyn, J. Nygård, P. Krogstrup, A. Geresdi, L. P. Kouwenhoven, and J. D. Watson, Magnetic-field-dependent quasiparticle dynamics of nanowire single-Cooper-pair transistors, *Phys. Rev. B* **98**, 174502 (2018).
- [54] E. T. Mannila, P. Samuelsson, S. Simbierowicz, J. T. Peltonen, V. Vesterinen, L. Grönberg, J. Hassel, V. F. Maisi, and J. P. Pekola, A superconductor free of quasiparticles for seconds, *Nat. Phys.* **18**, 145 (2022).
- [55] T. Karzig, W. S. Cole, and D. I. Pikulin, Quasiparticle Poisoning of Majorana Qubits, *Phys. Rev. Lett.* **126**, 057702 (2021).
- [56] D. Sticlet, J. D. Sau, and A. Akhmerov, Dissipation-enabled fractional Josephson effect, *Phys. Rev. B* **98**, 125124 (2018).
- [57] C. W. Groth, M. Wimmer, A. R. Akhmerov, and X. Waintal, Kwant: A software package for quantum transport, *New J. Phys.* **16**, 063065 (2014).
- [58] A. Weiße, G. Wellein, A. Alvermann, and H. Fehske, The kernel polynomial method, *Rev. Mod. Phys.* **78**, 275 (2006).
- [59] T. D. Stanescu, J. D. Sau, R. M. Lutchyn, and S. Das Sarma, Proximity effect at the superconductor–topological insulator interface, *Phys. Rev. B* **81**, 241310(R) (2010).

# Chapter 6

## Conclusion and Outlook

In this thesis, we have looked into the foundational principles of quantum spin Hall effect, which can be understood via analogies to quantum Hall and quantum anomalous Hall effects. We have studied the model by A. Bernevig, T. Hughes and S.C. Zhang which describes the quantum spin Hall effect observed in the band-inverted regime of type-I and type-II quantum wells. We have discussed the significant role of Coulomb interactions because of the spatially separated electron and hole subbands in type-II quantum wells. The Coulomb interactions in these quantum wells lead to the formation of an exciton condensate phase. By varying the tunneling term between the electron and hole layers, it is possible to turn the exciton condensate phase into a crossover. In this regime, it has been shown theoretically, that the correlated excitons lead to spontaneous time-reversal symmetry breaking for intermediate strengths of tunneling and the electron-hole density, which is controlled by the Dirac mass term  $E_G$  in the Hamiltonian. This time-reversal symmetry broken phase appears in between the trivial and quantum spin Hall phase. This results in an unconventional topological phase transition where the bulk-gap does not close. In the work comprising the first paper, we found that:

- The proposed experimental setup of a Corbino disc can be used to confirm the presence of an unconventional topological phase transition. We also test the topological phase transition in the presence of varied disorder strengths and mass asymmetry, and find that the transport characteristics confirm the

---

existence of the unconventional topological phase transition in all realistic situations.

We further discussed the possibility of utilizing the time-reversal broken phase that appears in type-II quantum wells due to excitons to realize Majorana zero modes. This avoids the problems that arise in the state of the art setups which use magnetic field or ferromagnetic insulators to break time-reversal symmetry. Our calculations presented in the second paper show that:

- It is possible to realize Majorana zero modes at the interface of a type-II quantum well in its spontaneously broken time-reversal symmetry phase and an s-wave superconductor.
- A superconductor/time-reversal symmetry broken insulator/superconductor Josephson junction provided an experimental signature of the Majorana zero modes that are present.
- Our theoretical prediction could be confirmed in state-of-the-art experimental devices.

In conclusion, we have answered the main three questions that formed the research problem for the doctoral dissertation.

Quantum spin Hall insulators offer quantized conductance only for short samples. Therefore, it is important to consider the role of interactions for a better insight into the physics of such materials. The emergence of correlated phases of excitons in bilayer systems as a result of Coulomb interactions have been studied extensively in theoretical frameworks and are also becoming increasingly evident in the experiments. Therefore, it is important to explore the interaction effects in topological materials, both experimentally and theoretically. Moreover, as has been shown, one could use interactions to realize Majorana zero modes. An experimental observation of these quasiparticles would solve one of the major problems in condensed matter physics.

# Bibliography

- [1] E. H. Hall. “On a New Action of the Magnet on Electric Currents”. In: *American Journal of Mathematics* 2.3 (1879), pp. 287–292. ISSN: 00029327, 10806377.
- [2] S. Datta. *Electronic Transport in Mesoscopic Systems*. Cambridge Studies in Semiconductor Physics and Microelectronic Engineering. Cambridge University Press, 1995. DOI: 10.1017/CB09780511805776.
- [3] K. von Klitzing, G. Dorda, and M. Pepper. “New Method for High-Accuracy Determination of the Fine-Structure Constant Based on Quantized Hall Resistance”. In: *Phys. Rev. Lett.* 45 (1980), pp. 494–497. DOI: 10.1103/PhysRevLett.45.494.
- [4] R. B. Laughlin. “Quantized Hall conductivity in two dimensions”. In: *Phys. Rev. B* 23 (1981), pp. 5632–5633. DOI: 10.1103/PhysRevB.23.5632.
- [5] B. I. Halperin. “Quantized Hall conductance, current-carrying edge states, and the existence of extended states in a two-dimensional disordered potential”. In: *Phys. Rev. B* 25 (1982), pp. 2185–2190. DOI: 10.1103/PhysRevB.25.2185.
- [6] J. Weis and K. von Klitzing. “Metrology and microscopic picture of the integer quantum Hall effect”. In: *Philosophical Transactions of the Royal Society A: Mathematical, Physical and Engineering Sciences* 369.1953 (2011), pp. 3954–3974. DOI: 10.1098/rsta.2011.0198.
- [7] Z. Jiang et al. “Quantum Hall effect in graphene”. In: *Solid State Communications* 143.1 (2007). Exploring graphene, pp. 14–19. ISSN: 0038-1098. DOI: 10.1016/j.ssc.2007.02.046.

- 
- [8] NobelPrize.org. *The Nobel Prize in Physics 1985*. URL: <https://www.nobelprize.org/prizes/physics/1985/summary/>.
- [9] R. B. Laughlin. “Anomalous Quantum Hall Effect: An Incompressible Quantum Fluid with Fractionally Charged Excitations”. In: *Phys. Rev. Lett.* 50 (1983), pp. 1395–1398. DOI: 10.1103/PhysRevLett.50.1395.
- [10] H. L. Stormer, D. C. Tsui, and A. C. Gossard. “The fractional quantum Hall effect”. In: *Rev. Mod. Phys.* 71 (1999), S298–S305. DOI: 10.1103/RevModPhys.71.S298.
- [11] D. C. Tsui, H. L. Stormer, and A. C. Gossard. “Two-Dimensional Magnetotransport in the Extreme Quantum Limit”. In: *Phys. Rev. Lett.* 48 (1982), pp. 1559–1562. DOI: 10.1103/PhysRevLett.48.1559.
- [12] J.P. Eisenstein. “Exciton Condensation in Bilayer Quantum Hall Systems”. In: *Annual Review of Condensed Matter Physics* 5.1 (2014), pp. 159–181. DOI: 10.1146/annurev-conmatphys-031113-133832.
- [13] B. Andrei Bernevig, Taylor L. Hughes, and Shou-Cheng Zhang. “Quantum Spin Hall Effect and Topological Phase Transition in HgTe Quantum Wells”. In: *Science* 314.5806 (2006), pp. 1757–1761. DOI: 10.1126/science.1133734.
- [14] M. König et al. “Quantum Spin Hall Insulator State in HgTe Quantum Wells”. In: *Science* 318.5851 (2007), pp. 766–770. DOI: 10.1126/science.1148047.
- [15] F. D. M. Haldane. “Model for a Quantum Hall Effect without Landau Levels: Condensed-Matter Realization of the “Parity Anomaly” ”. In: *Phys. Rev. Lett.* 61 (1988), pp. 2015–2018. DOI: 10.1103/PhysRevLett.61.2015.
- [16] X. L. Qi, Y. S. Wu, and S. C. Zhang. “Topological quantization of the spin Hall effect in two-dimensional paramagnetic semiconductors”. In: *Phys. Rev. B* 74 (2006), p. 085308. DOI: 10.1103/PhysRevB.74.085308.
- [17] C. Z. Chang et al. “Experimental Observation of the Quantum Anomalous Hall Effect in a Magnetic Topological Insulator”. In: *Science* 340.6129 (2013), pp. 167–170. DOI: 10.1126/science.1234414.

- 
- [18] C. Nayak et al. “Non-Abelian anyons and topological quantum computation”. In: *Rev. Mod. Phys.* 80 (2008), pp. 1083–1159. DOI: 10.1103/RevModPhys.80.1083.
- [19] S. S. Hegde et al. “Quasinormal Modes and the Hawking-Unruh Effect in Quantum Hall Systems: Lessons from Black Hole Phenomena”. In: *Phys. Rev. Lett.* 123 (2019), p. 156802. DOI: 10.1103/PhysRevLett.123.156802.
- [20] S. C. Zhang and J. Hu. “A Four-Dimensional Generalization of the Quantum Hall Effect”. In: *Science* 294.5543 (2001), pp. 823–828. DOI: 10.1126/science.294.5543.823.
- [21] L. D. Landau and L. M. Lifshitz. *Quantum Mechanics Non-Relativistic Theory, Third Edition: Volume 3*. Butterworth-Heinemann, 1981.
- [22] David Tong. *Lectures on the Quantum Hall Effect*. 2016. DOI: 10.48550/arXiv.1606.06687.
- [23] F. Delahaye and B. Jeckelmann. “Revised technical guidelines for reliable dc measurements of the quantized Hall resistance”. In: *Metrologia* 40.5 (2003), p. 217. DOI: 10.1088/0026-1394/40/5/302.
- [24] A. Fabre et al. “Laughlin’s Topological Charge Pump in an Atomic Hall Cylinder”. In: *Phys. Rev. Lett.* 128 (2022), p. 173202. DOI: 10.1103/PhysRevLett.128.173202.
- [25] K. von Klitzing et al. “40 years of the quantum Hall effect”. In: *Nature Reviews Physics* 2.8 (2020), pp. 397–401. DOI: 10.1038/s42254-020-0209-1.
- [26] D. J. Thouless et al. “Quantized Hall Conductance in a Two-Dimensional Periodic Potential”. In: *Phys. Rev. Lett.* 49 (1982), pp. 405–408. DOI: 10.1103/PhysRevLett.49.405.
- [27] Charles Kittel. *Introduction to Solid State Physics*. 8th ed. Wiley, 2004. ISBN: 9780471415268.
- [28] N. W. Ashcroft and N. D. Mermin. *Solid State Physics*. Holt-Saunders, 1976.

- 
- [29] M. Kohmoto. “Topological invariant and the quantization of the Hall conductance”. In: *Annals of Physics* 160.2 (1985), pp. 343–354. DOI: 10.1016/0003-4916(85)90148-4.
- [30] B. Simon. “Holonomy, the Quantum Adiabatic Theorem, and Berry’s Phase”. In: *Phys. Rev. Lett.* 51 (1983), pp. 2167–2170. DOI: 10.1103/PhysRevLett.51.2167.
- [31] M. Berry. “Quantal phase factors accompanying adiabatic changes”. In: *Proceedings of the Royal Society of London. A. Mathematical and Physical Sciences* 392.1802 (1984), pp. 45–57. DOI: 10.1098/rspa.1984.0023.
- [32] M. Berry. “Anticipations of the Geometric Phase”. In: *Physics Today* 43.12 (1990), pp. 34–40. DOI: 10.1063/1.881219.
- [33] D. B. Chklovskii, B. I. Shklovskii, and L. I. Glazman. “Electrostatics of edge channels”. In: *Phys. Rev. B* 46 (1992), pp. 4026–4034. DOI: 10.1103/PhysRevB.46.4026.
- [34] M. Büttiker. “Absence of backscattering in the quantum Hall effect in multiprobe conductors”. In: *Phys. Rev. B* 38 (1988), pp. 9375–9389. DOI: 10.1103/PhysRevB.38.9375.
- [35] M. Z. Hasan and C. L. Kane. “Colloquium: Topological insulators”. In: *Rev. Mod. Phys.* 82 (2010), pp. 3045–3067. DOI: 10.1103/RevModPhys.82.3045.
- [36] B.A. Bernevig. *Topological Insulators and Topological Superconductors*. Princeton: Princeton University Press, 2013. ISBN: 9781400846733. DOI: 10.1515/9781400846733.
- [37] J. K. Asbóth, L. Oroszlány, and A. Pályi. *A Short Course on Topological Insulators*. Springer International Publishing, 2016. DOI: 10.1007/978-3-319-25607-8.
- [38] H. Yasuhiro. “Chern number and edge states in the integer quantum Hall effect”. In: *Phys. Rev. Lett.* 71 (1993), pp. 3697–3700. DOI: 10.1103/PhysRevLett.71.3697.

- 
- [39] NobelPrize.org. *The Nobel Prize in Physics 1998*. URL: <https://www.nobelprize.org/prizes/physics/1998/summary/>.
- [40] M. B. Hastings and X. G. Wen. “Quasiadiabatic continuation of quantum states: The stability of topological ground-state degeneracy and emergent gauge invariance”. In: *Phys. Rev. B* 72 (2005), p. 045141. DOI: 10.1103/PhysRevB.72.045141.
- [41] M. B. Hastings and S. Michalakis. “Quantization of Hall Conductance for Interacting Electrons on a Torus”. In: *Communications in Mathematical Physics* 334.1 (2015), pp. 433–471. DOI: 10.1007/s00220-014-2167-x.
- [42] B. I. Halperin. “Possible States for a Three-Dimensional Electron Gas in a Strong Magnetic Field”. In: *Japanese Journal of Applied Physics* 26.S3-3 (1987), p. 1913. DOI: 10.7567/JJAPS.26S3.1913.
- [43] M. Kohmoto, B. I. Halperin, and Y. S. Wu. “Diophantine equation for the three-dimensional quantum Hall effect”. In: *Phys. Rev. B* 45 (1992), pp. 13488–13493. DOI: 10.1103/PhysRevB.45.13488.
- [44] J. Gooth, S. Galeski, and T. Meng. “Quantum-Hall physics and three dimensions”. In: *Reports on Progress in Physics* 86.4 (2023), p. 044501. DOI: 10.1088/1361-6633/acb8c9.
- [45] K. S. Novoselov et al. “Room-Temperature Quantum Hall Effect in Graphene”. In: *Science* 315.5817 (2007), pp. 1379–1379. DOI: 10.1126/science.1137201.
- [46] C. X. Liu, S. C. Zhang, and X. L. Qi. “The Quantum Anomalous Hall Effect: Theory and Experiment”. In: *Annual Review of Condensed Matter Physics* 7.1 (2016), pp. 301–321. DOI: 10.1146/annurev-conmatphys-031115-011417.
- [47] H. Chi and J. S. Moodera. “Progress and prospects in the quantum anomalous Hall effect”. In: *APL Materials* 10.9 (2022), p. 090903. DOI: 10.1063/5.0100989.
- [48] C. Z. Chang, C. X. Liu, and A. H. MacDonald. “Colloquium: Quantum anomalous Hall effect”. In: *Rev. Mod. Phys.* 95 (2023), p. 011002. DOI: 10.1103/RevModPhys.95.011002.
-

- 
- [49] J. Gregor et al. “Experimental realization of the topological Haldane model with ultracold fermions”. In: *Nature* 515.7526 (2014), pp. 237–240. DOI: 10.1038/nature13915.
- [50] A. L. Sharpe et al. “Emergent ferromagnetism near three-quarters filling in twisted bilayer graphene”. In: *Science* 365.6453 (2019), pp. 605–608. DOI: 10.1126/science.aaw3780.
- [51] M. Serlin et al. “Intrinsic quantized anomalous Hall effect in a moiré heterostructure”. In: *Science* 367.6480 (2020), pp. 900–903. DOI: 10.1126/science.aay5533.
- [52] T. Li et al. “Quantum anomalous Hall effect from intertwined moiré bands”. In: *Nature* 600.7890 (2021), pp. 641–646. DOI: 10.1038/s41586-021-04171-1.
- [53] Y. Deng et al. “Quantum anomalous Hall effect in intrinsic magnetic topological insulator  $\text{MnBi}_2\text{Te}_4$ ”. In: *Science* 367.6480 (2020), pp. 895–900. DOI: 10.1126/science.aax8156.
- [54] E. J. Fox et al. “Part-per-million quantization and current-induced breakdown of the quantum anomalous Hall effect”. In: *Phys. Rev. B* 98 (2018), p. 075145. DOI: 10.1103/PhysRevB.98.075145.
- [55] M. Götz et al. “Precision measurement of the quantized anomalous Hall resistance at zero magnetic field”. In: *Applied Physics Letters* 112.7 (2018). 072102. DOI: 10.1063/1.5009718.
- [56] Yi-Fan Zhao et al. “Tuning the Chern number in quantum anomalous Hall insulators”. In: *Nature* 588.7838 (2020), pp. 419–423. DOI: 10.1038/s41586-020-3020-3.
- [57] B. A. Bernevig and S. C. Zhang. “Quantum Spin Hall Effect”. In: *Phys. Rev. Lett.* 96 (2006), p. 106802. DOI: 10.1103/PhysRevLett.96.106802.
- [58] M. Z. Hasan and C. L. Kane. “Colloquium: Topological insulators”. In: *Rev. Mod. Phys.* 82 (2010), pp. 3045–3067. DOI: 10.1103/RevModPhys.82.3045.

- 
- [59] X. L. Qi and S. C. Zhang. “Topological insulators and superconductors”. In: *Rev. Mod. Phys.* 83 (2011), pp. 1057–1110. DOI: 10.1103/RevModPhys.83.1057.
- [60] C. X. Liu et al. “Quantum Spin Hall Effect in Inverted Type-II Semiconductors”. In: *Phys. Rev. Lett.* 100 (2008), p. 236601. DOI: 10.1103/PhysRevLett.100.236601.
- [61] M. König et al. “The Quantum Spin Hall Effect: Theory and Experiment”. In: *Journal of the Physical Society of Japan* 77.3 (2008), p. 031007. DOI: 10.1143/JPSJ.77.031007.
- [62] J. Maciejko, X. L. Qi, and S. C. Zhang. “Magnetoelectronic transport of the quantum spin Hall state”. In: *Phys. Rev. B* 82 (2010), p. 155310. DOI: 10.1103/PhysRevB.82.155310.
- [63] C. L. Kane and E. J. Mele. “Quantum Spin Hall Effect in Graphene”. In: *Phys. Rev. Lett.* 95 (2005), p. 226801. DOI: 10.1103/PhysRevLett.95.226801.
- [64] C. L. Kane and E. J. Mele. “ $\mathbb{Z}_2$  Topological Order and the Quantum Spin Hall Effect”. In: *Phys. Rev. Lett.* 95 (2005), p. 146802. DOI: 10.1103/PhysRevLett.95.146802.
- [65] Y. Yao et al. “Spin-orbit gap of graphene: First-principles calculations”. In: *Phys. Rev. B* 75 (2007), p. 041401. DOI: 10.1103/PhysRevB.75.041401.
- [66] H. Min et al. “Intrinsic and Rashba spin-orbit interactions in graphene sheets”. In: *Phys. Rev. B* 74 (2006), p. 165310. DOI: 10.1103/PhysRevB.74.165310.
- [67] C. Wu, B. A. Bernevig, and S. C. Zhang. “Helical Liquid and the Edge of Quantum Spin Hall Systems”. In: *Phys. Rev. Lett.* 96 (2006), p. 106401. DOI: 10.1103/PhysRevLett.96.106401.
- [68] C. Xu and J. E. Moore. “Stability of the quantum spin Hall effect: Effects of interactions, disorder, and  $\mathbb{Z}_2$  topology”. In: *Phys. Rev. B* 73 (2006), p. 045322. DOI: 10.1103/PhysRevB.73.045322.

- 
- [69] A. Altland and M. R. Zirnbauer. “Nonstandard symmetry classes in mesoscopic normal-superconducting hybrid structures”. In: *Phys. Rev. B* 55 (1997), pp. 1142–1161. DOI: 10.1103/PhysRevB.55.1142.
- [70] L. Du et al. “Robust Helical Edge Transport in Gated InAs/GaSb Bilayers”. In: *Phys. Rev. Lett.* 114 (2015), p. 096802. DOI: 10.1103/PhysRevLett.114.096802.
- [71] I. Knez et al. “Observation of Edge Transport in the Disordered Regime of Topologically Insulating InAs/GaSb Quantum Wells”. In: *Phys. Rev. Lett.* 112 (2014), p. 026602. DOI: 10.1103/PhysRevLett.112.026602.
- [72] E. M. Spanton et al. “Images of Edge Current in InAs/GaSb Quantum Wells”. In: *Phys. Rev. Lett.* 113 (2014), p. 026804. DOI: 10.1103/PhysRevLett.113.026804.
- [73] A. Roth et al. “Nonlocal Transport in the Quantum Spin Hall State”. In: *Science* 325.5938 (2009), pp. 294–297. DOI: 10.1126/science.1174736.
- [74] K. C. Nowack et al. “Imaging currents in HgTe quantum wells in the quantum spin Hall regime”. In: *Nature Materials* 12.9 (2013), pp. 787–791. DOI: 10.1038/nmat3682.
- [75] K. Suzuki et al. “Edge channel transport in the InAs/GaSb topological insulating phase”. In: *Phys. Rev. B* 87 (2013), p. 235311. DOI: 10.1103/PhysRevB.87.235311.
- [76] G. Grabecki et al. “Nonlocal resistance and its fluctuations in microstructures of band-inverted HgTe/(Hg,Cd)Te quantum wells”. In: *Phys. Rev. B* 88 (2013), p. 165309. DOI: 10.1103/PhysRevB.88.165309.
- [77] I. Knez, R. R. Du, and G. Sullivan. “Evidence for Helical Edge Modes in Inverted InAs/GaSb Quantum Wells”. In: *Phys. Rev. Lett.* 107 (2011), p. 136603. DOI: 10.1103/PhysRevLett.107.136603.

- 
- [78] B. L. Altshuler, I. L. Aleiner, and V. I. Yudson. “Localization at the Edge of a 2D Topological Insulator by Kondo Impurities with Random Anisotropies”. In: *Phys. Rev. Lett.* 111 (2013), p. 086401. DOI: 10.1103/PhysRevLett.111.086401.
- [79] V. Cheianov and L. I. Glazman. “Mesoscopic Fluctuations of Conductance of a Helical Edge Contaminated by Magnetic Impurities”. In: *Phys. Rev. Lett.* 110 (2013), p. 206803. DOI: 10.1103/PhysRevLett.110.206803.
- [80] F. Crépin et al. “Renormalization group approach for the scattering off a single Rashba impurity in a helical liquid”. In: *Phys. Rev. B* 86 (2012), p. 121106. DOI: 10.1103/PhysRevB.86.121106.
- [81] T. L. Schmidt et al. “Inelastic Electron Backscattering in a Generic Helical Edge Channel”. In: *Phys. Rev. Lett.* 108 (2012), p. 156402. DOI: 10.1103/PhysRevLett.108.156402.
- [82] N. Lezmy, Y. Oreg, and M. Berkooz. “Single and multiparticle scattering in helical liquid with an impurity”. In: *Phys. Rev. B* 85 (2012), p. 235304. DOI: 10.1103/PhysRevB.85.235304.
- [83] J. I. Väyrynen, Moshe Goldstein, and Leonid I. Glazman. “Helical Edge Resistance Introduced by Charge Puddles”. In: *Phys. Rev. Lett.* 110 (2013), p. 216402. DOI: 10.1103/PhysRevLett.110.216402.
- [84] J. I. Väyrynen et al. “Resistance of helical edges formed in a semiconductor heterostructure”. In: *Phys. Rev. B* 90 (2014), p. 115309. DOI: 10.1103/PhysRevB.90.115309.
- [85] D. I. Pikulin and T. Hyart. “Interplay of Exciton Condensation and the Quantum Spin Hall Effect in InAs/GaSb Bilayers”. In: *Phys. Rev. Lett.* 112 (2014), p. 176403. DOI: 10.1103/PhysRevLett.112.176403.
- [86] R. Skolasinski et al. “Robust helical edge transport in quantum spin Hall quantum wells”. In: *Phys. Rev. B* 98 (2018), p. 201404. DOI: 10.1103/PhysRevB.98.201404.

- 
- [87] Y. Naveh and B. Laikhtman. “Excitonic Instability and Electric-Field-Induced Phase Transition Towards a Two-Dimensional Exciton Condensate”. In: *Phys. Rev. Lett.* 77 (1996), pp. 900–903. DOI: 10.1103/PhysRevLett.77.900.
- [88] L. Du et al. “Evidence for a topological excitonic insulator in InAs/GaSb bilayers”. In: *Nature Communications* 8.1 (2017), p. 1971. DOI: 10.1038/s41467-017-01988-1.
- [89] X. Wu et al. “Resistive signature of excitonic coupling in an electron-hole double layer with a middle barrier”. In: *Phys. Rev. B* 99 (2019), p. 085307. DOI: 10.1103/PhysRevB.99.085307.
- [90] X. J. Wu et al. “Electrically tuning many-body states in a Coulomb-coupled InAs/InGaSb double layer”. In: *Phys. Rev. B* 100 (2019), p. 165309. DOI: 10.1103/PhysRevB.100.165309.
- [91] D. Xiao et al. “Anomalous Quantum Oscillations of Interacting Electron-Hole Gases in Inverted Type-II InAs/GaSb Quantum Wells”. In: *Phys. Rev. Lett.* 122 (2019), p. 186802. DOI: 10.1103/PhysRevLett.122.186802.
- [92] R. Wang et al. “Excitonic topological order in imbalanced electron–hole bilayers”. In: *Nature* 619.7968 (2023), pp. 57–62. DOI: 10.1038/s41586-023-06065-w.
- [93] Y. Jia et al. “Evidence for a monolayer excitonic insulator”. In: *Nature Physics* 18.1 (2022), pp. 87–93. DOI: 10.1038/s41567-021-01422-w.
- [94] B. Sun et al. “Evidence for equilibrium exciton condensation in monolayer WTe<sub>2</sub>”. In: *Nature Physics* 18.1 (2022), pp. 94–99. DOI: 10.1038/s41567-021-01427-5.
- [95] Y. Q. Wang, M. Papaj, and J. E. Moore. “Breakdown of helical edge state topologically protected conductance in time-reversal-breaking excitonic insulators”. In: (2023). DOI: 10.48550/arXiv.2305.09202.
- [96] J. C. Budich, B. Trauzettel, and P. Michetti. “Time Reversal Symmetric Topological Exciton Condensate in Bilayer HgTe Quantum Wells”. In: *Phys. Rev. Lett.* 112 (2014), p. 146405. DOI: 10.1103/PhysRevLett.112.146405.
-

- 
- [97] S. D. Sarma, M. Freedman, and C. Nayak. “Majorana zero modes and topological quantum computation”. In: *npj Quantum Information* 1.1 (2015), p. 15001. DOI: 10.1038/npjqi.2015.1.
- [98] J. Alicea. “New directions in the pursuit of Majorana fermions in solid state systems”. In: *Reports on Progress in Physics* 75.7 (2012), p. 076501. DOI: 10.1088/0034-4885/75/7/076501.
- [99] M. Leijnse and K. Flensberg. “Introduction to topological superconductivity and Majorana fermions”. In: *Semiconductor Science and Technology* 27.12 (2012), p. 124003. DOI: 10.1088/0268-1242/27/12/124003.
- [100] K. Flensberg, F. von Oppen, and A. Stern. “Engineered platforms for topological superconductivity and Majorana zero modes”. In: *Nature Reviews Materials* 6.10 (2021), pp. 944–958. DOI: 10.1038/s41578-021-00336-6.
- [101] C.W.J. Beenakker. “Search for Majorana Fermions in Superconductors”. In: *Annual Review of Condensed Matter Physics* 4.1 (2013), pp. 113–136. DOI: 10.1146/annurev-conmatphys-030212-184337.
- [102] C. Nayak et al. “Non-Abelian anyons and topological quantum computation”. In: *Rev. Mod. Phys.* 80 (2008), pp. 1083–1159. DOI: 10.1103/RevModPhys.80.1083.
- [103] C. W. J. Beenakker. “Search for non-Abelian Majorana braiding statistics in superconductors”. In: *SciPost Phys. Lect. Notes* (2020), p. 15. DOI: 10.21468/SciPostPhysLectNotes.15.
- [104] E. Majorana. “Teoria simmetrica dell’elettrone e del positrone”. In: *Il Nuovo Cimento (1924-1942)* 14.4 (1937), pp. 171–184. DOI: 10.1007/BF02961314.
- [105] M. M. Salomaa and G. E. Volovik. “Half-Quantum Vortices in Superfluid  $^3\text{He-A}$ ”. In: *Phys. Rev. Lett.* 55 (1985), pp. 1184–1187. DOI: 10.1103/PhysRevLett.55.1184.
- [106] A. P. Mackenzie and Y. Maeno. “The superconductivity of  $\text{Sr}_2\text{RuO}_4$  and the physics of spin-triplet pairing”. In: *Rev. Mod. Phys.* 75 (2003), pp. 657–712. DOI: 10.1103/RevModPhys.75.657.

- 
- [107] A Yu Kitaev. “Unpaired Majorana fermions in quantum wires”. In: *Physics-Usp ekhi* 44.10S (2001), p. 131. DOI: 10.1070/1063-7869/44/10S/S29.
- [108] L. Fu and C. L. Kane. “Superconducting Proximity Effect and Majorana Fermions at the Surface of a Topological Insulator”. In: *Phys. Rev. Lett.* 100 (2008), p. 096407. DOI: 10.1103/PhysRevLett.100.096407.
- [109] J. D. Sau et al. “Generic New Platform for Topological Quantum Computation Using Semiconductor Heterostructures”. In: *Phys. Rev. Lett.* 104 (2010), p. 040502. DOI: 10.1103/PhysRevLett.104.040502.
- [110] J. Alicea. “Majorana fermions in a tunable semiconductor device”. In: *Phys. Rev. B* 81 (2010), p. 125318. DOI: 10.1103/PhysRevB.81.125318.
- [111] K. T. Law, P. A. Lee, and T. K. Ng. “Majorana Fermion Induced Resonant Andreev Reflection”. In: *Phys. Rev. Lett.* 103 (2009), p. 237001. DOI: 10.1103/PhysRevLett.103.237001.
- [112] S. Mi et al. “Proposal for the detection and braiding of Majorana fermions in a quantum spin Hall insulator”. In: *Phys. Rev. B* 87 (2013), p. 241405. DOI: 10.1103/PhysRevB.87.241405.
- [113] L. Fu and C. L. Kane. “Josephson current and noise at a superconductor/quantum-spin-Hall-insulator/superconductor junction”. In: *Phys. Rev. B* 79 (2009), p. 161408. DOI: 10.1103/PhysRevB.79.161408.
- [114] C. W. J. Beenakker et al. “Fermion-Parity Anomaly of the Critical Supercurrent in the Quantum Spin-Hall Effect”. In: *Phys. Rev. Lett.* 110 (2013), p. 017003. DOI: 10.1103/PhysRevLett.110.017003.
- [115] V. S. Pribiag et al. “Edge-mode superconductivity in a two-dimensional topological insulator”. In: *Nature Nanotechnology* 10.7 (2015), pp. 593–597. DOI: 10.1038/nnano.2015.86.
- [116] J. B. Fu et al. “Experimental review on Majorana zero-modes in hybrid nanowires”. In: *Science China Physics, Mechanics & Astronomy* 64.10 (2021), p. 107001. DOI: 10.1007/s11433-021-1737-4.

- 
- [117] H. Zhang et al. “RETRACTED ARTICLE: Quantized Majorana conductance”. In: *Nature* 556.7699 (2018), pp. 74–79. DOI: 10.1038/nature26142.
- [118] Qing L. H. et al. “RETRACTED: Chiral Majorana fermion modes in a quantum anomalous Hall insulator-superconductor structure”. In: *Science* 357.6348 (2017), pp. 294–299. DOI: 10.1126/science.aag2792.
- [119] S. Hart et al. “Induced superconductivity in the quantum spin Hall edge”. In: *Nature Physics* 10.9 (2014), pp. 638–643. DOI: 10.1038/nphys3036.
- [120] I. Knez, R. R. Du, and G. Sullivan. “Andreev Reflection of Helical Edge Modes in InAs/GaSb Quantum Spin Hall Insulator”. In: *Phys. Rev. Lett.* 109 (2012), p. 186603. DOI: 10.1103/PhysRevLett.109.186603.
- [121] R. S. Deacon et al. “Josephson Radiation from Gapless Andreev Bound States in HgTe-Based Topological Junctions”. In: *Phys. Rev. X* 7 (2017), p. 021011. DOI: 10.1103/PhysRevX.7.021011.
- [122] S. Vaitiekėnas et al. “Zero-bias peaks at zero magnetic field in ferromagnetic hybrid nanowires”. In: *Nature Physics* 17.1 (2021), pp. 43–47. DOI: 10.1038/s41567-020-1017-3.
- [123] B. Jäck, Yonglong Xie, and Ali Yazdani. “Detecting and distinguishing Majorana zero modes with the scanning tunnelling microscope”. In: *Nature Reviews Physics* 3.8 (2021), pp. 541–554. DOI: 10.1038/s42254-021-00328-z.
- [124] C.W. Groth et al. “Kwant: a software package for quantum transport”. In: *New Journal of Physics* 16.6 (2014), p. 063065. DOI: 10.1088/1367-2630/16/6/063065.
- [125] T. Paul, V. F. Becerra, and T. Hyart. “Interplay of quantum spin Hall effect and spontaneous time-reversal symmetry breaking in electron-hole bilayers. I. Transport properties”. In: *Phys. Rev. B* 106 (2022), p. 235420. DOI: 10.1103/PhysRevB.106.235420.
- [126] Yuli V. Nazarov and Yaroslav M. Blanter. *Quantum Transport: Introduction to Nanoscience*. Cambridge University Press, 2009.

- 
- [127] G. E. Blonder, M. Tinkham, and T. M. Klapwijk. “Transition from metallic to tunneling regimes in superconducting microconstrictions: Excess current, charge imbalance, and supercurrent conversion”. In: *Phys. Rev. B* 25 (1982), pp. 4515–4532. DOI: 10.1103/PhysRevB.25.4515.
- [128] J. P. Eisenstein and A. H. MacDonald. “Bose–Einstein condensation of excitons in bilayer electron systems”. In: *Nature* 432.7018 (2004), pp. 691–694. DOI: 10.1038/nature03081.
- [129] I. B. Spielman et al. “Resonantly Enhanced Tunneling in a Double Layer Quantum Hall Ferromagnet”. In: *Phys. Rev. Lett.* 84 (2000), pp. 5808–5811. DOI: 10.1103/PhysRevLett.84.5808.
- [130] A. D. K. Finck et al. “Exciton Transport and Andreev Reflection in a Bilayer Quantum Hall System”. In: *Phys. Rev. Lett.* 106 (2011), p. 236807. DOI: 10.1103/PhysRevLett.106.236807.
- [131] G. W. Burg et al. “Strongly Enhanced Tunneling at Total Charge Neutrality in Double-Bilayer Graphene-WSe<sub>2</sub> Heterostructures”. In: *Phys. Rev. Lett.* 120 (2018), p. 177702. DOI: 10.1103/PhysRevLett.120.177702.
- [132] M. König et al. “Spatially Resolved Study of Backscattering in the Quantum Spin Hall State”. In: *Phys. Rev. X* 3 (2013), p. 021003. DOI: 10.1103/PhysRevX.3.021003.
- [133] C. Liu and S. C. Zhang. *Models and Materials for Topological Insulators*, edited by M. Franz and L. Molenkamp, *Topological Insulators*. Springer, 2013.
- [134] L. J. Cooper et al. “Resistance resonance induced by electron-hole hybridization in a strongly coupled InAs/GaSb/AlSb heterostructure”. In: *Phys. Rev. B* 57 (1998), pp. 11915–11918. DOI: 10.1103/PhysRevB.57.11915.
- [135] Y. Naveh and B. Laikhtman. “Band-structure tailoring by electric field in a weakly coupled electron-hole system”. In: *Applied Physics Letters* 66.15 (1995), pp. 1980–1982. DOI: 10.1063/1.113297.

- 
- [136] V. Lechner. “Bulk and structure inversion asymmetry in semiconductor quantum well structures”. PhD thesis. University of Regensburg, 2012. DOI: 10.5283/epub.25885.
- [137] T. Paul, V. F. Becerra, and T. Hyart. “Interplay of quantum spin Hall effect and spontaneous time-reversal symmetry breaking in electron-hole bilayers. II. Zero-field topological superconductivity”. In: *Phys. Rev. B* 106 (2022), p. 235421. DOI: 10.1103/PhysRevB.106.235421.
- [138] J. Maciejko, T. L. Hughes, and S. C. Zhang. “The Quantum Spin Hall Effect”. In: *Annual Review of Condensed Matter Physics* 2.1 (2011), pp. 31–53. DOI: 10.1146/annurev-conmatphys-062910-140538.
- [139] R. B. Laughlin. “Quantized Hall conductivity in two dimensions”. In: *Phys. Rev. B* 23 (1981), pp. 5632–5633. DOI: 10.1103/PhysRevB.23.5632.
- [140] G. Tkachov and E.M. Hankiewicz. “Two-dimensional topological insulators in quantizing magnetic fields”. In: *Physica E: Low-dimensional Systems and Nanostructures* 44.5 (2012), pp. 900–905. DOI: 10.1016/j.physe.2011.11.012.
- [141] G. Tkachov and E. M. Hankiewicz. “Ballistic Quantum Spin Hall State and Enhanced Edge Backscattering in Strong Magnetic Fields”. In: *Phys. Rev. Lett.* 104 (2010), p. 166803. DOI: 10.1103/PhysRevLett.104.166803.
- [142] J. C. Chen, J. Wang, and Q. F. Sun. “Effect of magnetic field on electron transport in HgTe/CdTe quantum wells: Numerical analysis”. In: *Phys. Rev. B* 85 (2012), p. 125401. DOI: 10.1103/PhysRevB.85.125401.
- [143] B. Scharf, A. Matos-Abiague, and J. Fabian. “Magnetic properties of HgTe quantum wells”. In: *Phys. Rev. B* 86 (2012), p. 075418. DOI: 10.1103/PhysRevB.86.075418.
- [144] J. R. Meyer et al. “Magneto-optical properties of HgTe-CdTe superlattices”. In: *Phys. Rev. B* 42 (1990), pp. 9050–9062. DOI: 10.1103/PhysRevB.42.9050.

- 
- [145] M. Schultz et al. “Crossing of conduction- and valence-subband Landau levels in an inverted HgTe/CdTe quantum well”. In: *Phys. Rev. B* 57 (1998), pp. 14772–14775. DOI: 10.1103/PhysRevB.57.14772.
- [146] D. I. Pikulin et al. “Disorder and magnetic-field-induced breakdown of helical edge conduction in an inverted electron-hole bilayer”. In: *Phys. Rev. B* 89 (2014), p. 161403. DOI: 10.1103/PhysRevB.89.161403.
- [147] C. W. Groth et al. “Theory of the Topological Anderson Insulator”. In: *Phys. Rev. Lett.* 103 (2009), p. 196805. DOI: 10.1103/PhysRevLett.103.196805.
- [148] D. I. Pikulin, P. G. Silvestrov, and T. Hyart. “Confinement-deconfinement transition due to spontaneous symmetry breaking in quantum Hall bilayers, journal=Nature Communications”. In: 7.1 (2016), p. 10462. DOI: 10.1038/ncomms10462.
- [149] L. H. Hu et al. “Effect of in-plane magnetic field and applied strain in quantum spin Hall systems: Application to InAs/GaSb quantum wells”. In: *Phys. Rev. B* 94 (2016), p. 085306. DOI: 10.1103/PhysRevB.94.085306.
- [150] L. V. Keldysh and A. N. Kozlov. “Collective properties of excitons in semiconductors”. In: *Journal of Experimental and Theoretical Physics* 27.3 (1968), p. 521.
- [151] P. B. Littlewood and X. Zhu. “Possibilities for exciton condensation in semiconductor quantum-well structures”. In: *Physica Scripta* 1996.T68 (1996), p. 56. DOI: 10.1088/0031-8949/1996/T68/008.
- [152] Y. E. Lozovik and V.I. Yudson. “Feasibility of superfluidity of paired spatially separated electrons and holes; a new superconductivity mechanism”. In: *Soviet Journal of Experimental and Theoretical Physics Letters* 22 (1975), p. 274.
- [153] Y. E. Lozovik and V. I. Yudson. “New mechanism for superconductivity: pairing between spatially separated electrons and holes”. In: *Sov. Phys. JETP* 44.2 (1976), p. 389.

- 
- [154] Y. P. Shim and A. H. MacDonald. “Spin-orbit interactions in bilayer exciton-condensate ferromagnets”. In: *Phys. Rev. B* 79 (2009), p. 235329. DOI: 10.1103/PhysRevB.79.235329.
- [155] X. Zhu et al. “Exciton Condensate in Semiconductor Quantum Well Structures”. In: *Phys. Rev. Lett.* 74 (1995), pp. 1633–1636. DOI: 10.1103/PhysRevLett.74.1633.